METAL OXIDE, GROUP V-VI CHALCOGENIDES AND GAN/ALGAN PHOTODETECTORS

by

Md Rezaul Hasan

A Dissertation
Submitted to the
Graduate Faculty
of
George Mason University
In Partial Fulfillment of
The Requirements for the Degree
of
Doctor of Philosophy
Electrical and Computer Engineering

Committee:

_____ Dr. Rao Mulpuri, Dissertation Director

_____ Dr. Dimitris Ioannou, Committee Member

_____ Dr. Abhishek Motayed, Committee Member

_____ Dr. Qiliang Li, Committee Member

_____ Dr. Alok Berry, Committee Member

_____ Dr. Albert Davydov, Committee Member

_____ Dr. Monson H. Hayes, Department Chair

_____ Dr. Kenneth S. Ball, Dean, Volgenau School of Engineering

Date: _____ Fall Semester 2016
George Mason University
Fairfax, VA

Metal Oxide, Group V-VI Chalcogenides and GaN/AlGaN Photodetectors

A Dissertation submitted in partial fulfillment of the requirements for the degree of Doctor of Philosophy at George Mason University

by

Md Rezaul Hasan
Master of Science
Islamic University of Technology, Dhaka, Bangladesh 2012
Bachelor of Science
Islamic University of Technology, Dhaka, Bangladesh 2009

Dissertation Chair: Rao Mulpuri, Professor
Department of Electrical and Computer Engineering

Fall Semester 2016
George Mason University
Fairfax, VA

DEDICATION

This work is dedicated to my beloved parents, my wife Mayeesha Tabassum,my elder brother Nazmul Hasan and my sister Taslima Jahan.

ACKNOWLEDGEMENTS

I would like to thank many friends, relatives, and supporters who have made this happen. My special gratitude goes to Ratan Debnath, Dmitry Veksler and Sergey L. Rumyantsev who assisted me greatly in my research. All the committee members rendered me with their invaluable guidance and help throughout my research work as well.

TABLE OF CONTENTS

LIST OF TABLES

LIST OF FIGURES

LIST OF EQUATIONS

LIST OF ABBREVIATIONS AND SYMBOLS

Photodetector.....PD
Transparent Metal Oxide.....TMO
Ultraviolet.....UV
Polyethylene Tetraphthalate.....PET
Scanning Electron Microscopy.....SEM
Atomic Force Microscopy.....AFM
X-Ray Diffraction.....XRD
Field Effect Transistor.....FET
High Electron Mobility Transistor.....HEMT
Metal Oxide Semiconductor High Electron Mobility Transistor.....MOS-HEMT
Carrier Number Fluctuation.....CNF
Hooge's Mobility Fluctuation.....HMF
Metal-Semiconductor-Metal.....MSM
Transparent Oxide Semiconductors.....TOS
External Quantum Efficiency.....EQE
Noise Equivalent Power.....NEP
Terahertz.....THz
Galium Nitride.....GaN
Aluminium Galium Nitride.....AlGaN
Low Frequency Noise.....LFN
Genration-Recombination.....G-R
Near-Infrared.....NIR
Radio Frequency.....RF
Zinc Oxide.....ZnO
Nickel Oxide.....NiO
Light Emitting DIode.....LED
Indium Doped Tin Oxide.....ITO
Tin Oxide.....SnO_2
Copper Oxide.....CuO
Nano-particle.....NP
Ethylenediamine.....EDA
Nanowire.....NW
Nano-rod.....NR
Transmission Electron Microscopy.....TEM
Noise Spectral Density.....NSD

ABSTRACT

METAL OXIDE, GROUP V-VI CHALCOGENIDES AND GAN/ALGAN PHOTODETECTORS

Md Rezaul Hasan, Ph.D.

George Mason University, 2016

Dissertation Director: Dr. Rao Mulpuri

Structural, electrical and optical properties of metal oxide and Group V-VI chalcogenide based semiconductor materials and their optoelectronic response were studied when used as UV-Visible-NIR photodetectors. Optimization of processing steps was done to achieve better quality films in terms of crystallinity and stoichiometry.The films were thoroughly characterized for their structural, electrical and optical behavior. For visible blind- UV detection, transparent metal oxide (TMO) based photodiodes were fabricated and for UV-NIR broadband detection of wavelength, Group V-VI chalcogenide nanostructure photodiodes were fabricated.

A self-powered ultraviolet (UV) photodetector (PD) based on p-NiO/ n-ZnO was sputtered on flexible substrates. The fabricated devices showed good photovoltaic properties with a fill factor of ~ 41% under the illumination wavelength of 370 nm. Excellent photoresponse factor of ~2600 and external quantum efficiency of 63% was obtained. The engineered ultrathin Ti/Au top metal contacts and UV transparent

Polyethylene tetraphthalate (PET)substrates allowed the PDs to be illuminated through either top or bottom side. Significant performance enhancement of metal oxide based UV detectors was exhibited by fabricating Tin oxide (SnO_2) thin film ultraviolet (UV) photodetectors through incorporation of sputtered Cu clusters that oxidize in ambience to form CuO. The performance improvements were attributed to: (i) enhanced UV absorption as demonstrated both experimentally and by optical simulations. And (ii) electron transfer facilitated by the nanoheterojunctions between CuO and SnO_2. The peak responsivity of the PDs at a bias of 0.2 V improved from 1.9 A/W in a SnO_2-only device to 10.3 A/W after CuO deposition.

As representative of Group V-VI chalcogenide materials, Sb_2Se_3 and Sb_2S_3 based UV to visible broadband photodetectors were fabricated. A flexible, low-cost and scalable, catalyst-free one-step solution-processed novel approach, to grow Sb_2Se_3nanostructures was demonstrated. Structural characterization and compositional analyses revealed: (i)high-quality single-crystalline material with orthorhombic crystal structure, (ii) a near-stoichiometric Sb/Se atomic ratio and (ii) direct band gap of 1.12 eV. The fabricated metal-semiconductor-metal (MSM) photodetectors exhibited fast response (on the order of milliseconds) and high performance (responsivity ~ 0.27 A/W) as well as excellent mechanical flexibility and durability. Antimony sulphide nanostructures were grown directly on flexible polyamide substrates using similar method and this also showed good material quality and photoconductive behavior.

In this work, a simple, low-cost and catalyst free one-step solution processing of one-dimensional Sb_2S_3 nanostructures on polyimide substrates was done. This structure

demonstrated its potential application as a photoconductor in the UV and visible regime. Using-field emission scanning electron microscopy (SEM), grazing incidence X-Ray diffraction, Raman spectra and transmission electron microscopy measurements, it was shown that the Sb_2S_3 films have high crystallinity, uniform morphology and near-stoichiometric composition. Further, using tauc plot, it was found that the films have a direct bandgap of ~1.67 eV. MSM photodetectors, fabricated using these films showed a clear photo response in both UV as well as visible wavelength. These devices showed UV on/off ratio as high as 160 under the light intensity of 30 mW/cm^2 and a small rise time and fall time of 44 ms 28 ms respectively.

The effect of geometry of metal pad and bonding wire orientation of a multi-channel FET on the coupling of THz radiation was studied. The spatial variation images were taken by raster scan with the resolution of 0.07 mm steps in both x and y directions. An effective gate bias, where the effect of noise is minimum and photoresponse is maximum, was used for imaging. By applying V_{GS} =-2.8V and V_{DS} =380mV, the images were taken for all different combinations of activated bonding wires and metal pads. It was observed that, effect of bonding wire orientation is negligible for the large source pad as the radiation is coupled basically between drain and gate pad. Effect of drain bonding wire on coupling depends on the maximum width or diameter of metal pad and the incoming wavelength. In this work, Position of activated Drain pad and orientation of respective bonding wire defined the image tilting angle. Voltage drop across the shorting metal between drain pads, also played a role in increasing the asymmetry by selectively exciting a certain portion of FET Channels more than the other portion. Position of gate

pad defined the center point of the image without tilting the image as the geometry of the gate pads were parallel to each other. And there was no effect of gate pad bonding wire orientation because of the larger width of gate pads.

For the GaN/AlGaNHEMT, the effect of Al mole fraction in AlGaN layer and the effect of gate oxide on the DC and low frequency noise characterization was studied. MOS-HEMT with SiO_2 improved the $I_{d(on)}/I_{d(off)}$ ratio up to more than 8 orders, while it is only ~10 times in conventional HEMT. It was shown that the gate leakage and isolation leakage suppression efficiency improved dramatically with the oxide. Subthreshold swing (SS) of MOS-HEMTs with different Al mole fraction (from 20% to 35%) vary slightly from 72 mV/decade to 79 mV/decade, but the conventional GaN/AlGaN HEMT showed SS of 2.4V/decade. Low frequency noise study revealed the difference in transport mechanism between HEMT and MOS-HEMTs. By using Carrier Number Fluctuation (CNF) model on the measured data, it was found that the noise is predominantly coming from the surface states. While generation-recombination is very prominent in conventional HEMT, it is very weak and insignificant in both MOS-HEMTs at much higher frequencies. This study reveals that very high number of surface states assisting the tunneling in schottky/AlGaN barrier is responsible for unusually high leakage and higher noise level in conventional HEMT. Leakage level is improved from mA/mm range for HEMT to pA/mm range for MOS-HEMTs. Leakage suppression improvement and minimization of noise level can be mainly attributed to high quality SiO_2. Hooge's constant was in the order of $5\text{-}6\times10^{-3}$ in MOS-HEMTs, which is 5×10^{-2} for conventional HEMT indicating much lower noise level in the MOS-HEMTs.

CHAPTER ONE: INTRODUCTION

1.1 Overview of Metal Oxide based UV Photodetector

In recent years, Ultraviolet (UV) photodetection has attracted the attention of research community due to wide range of civil and military applications such as secure space-to-space communications, pollution monitoring, water sterilization, flame sensing and early missile plume detection.[1] Ultraviolet ray detection systems so far employed several process technologies such as Metal-organic Chemical Vapor Deposition (MOCVD), Molecular Beam Epitaxy (MBE), Pulse laser deposition (PLD), Radio Frequency Sputtering, electron-beam evaporation and solution processing method[2].The device structures used so far are normal photoconductors, p-n junction photodiode and Metal-semiconductor-metal (MSM) photodiodes for the detection of UV light. Several techniques were also explored to improve the responsivity. Techniques such as surface HCl treatment[2,19] and SiO_2 capping layer[2,20] on the surface of the devices can increase the photoresponsivity, but they also can increase the dark current due to the damage on semiconductor films. Among different optoelectronic nanodevices, the visible-blind UV-light photodetectors showed wide range of applications in imaging, light-wave communications, memory storage and optoelectronic circuits.[3,2]Although many UV-detectors have recently been developed using pn-junction, MSM and schottky junction diodes of wide-gap semiconductors such as GaN [1-4], ZnSe [3,5,6], ZnS [3,7] and diamond

[3,8]systems, transparent oxide semiconductors (TOSs) are much more preferable for the fabrication of UV-detectors. Because TOSs are optically transparent in visible and near UV-light region, environmental friendly and thermally and chemically stable.[4-8]Transparent oxide semiconductors (TOSs) have also attracted considerable attention in recent years, due to their versatile applications in transparent thin-film transistors,[1,2,3] transparent electrodes,[3] and optoelectronics,[4–6]. Visible-blind ultraviolet (UV) photodetectors (PDs) are of particular interest, owing to their broad application in digital imaging, missile plume detection, optical communications, and biomedical sensing.[7–9]TMOs were also used for some other various device applications[9-11] as alternatives to silicon and other wide-bandgap inorganic semiconductors such as SiC, GaN etc. Among various TMOs, ZnO and NiO thin films are of particular interest. ZnO is widely studied for applications such as light emitting diodes (LEDs),[12]solar cells,[13] chemical sensors,[14] nanogenerator,[15] photodetectors,[16]thin-film transistor,[17]and memory devices.[18]NiOhas been usedin LEDs,[19]resistive memory switching,[20,21] and photovoltaics.[22]NiO and ZnO, intrinsically p- and n-type semiconductors, respectively, are greatly used due to their distinguished electrical and optical properties[23-27],among the other demonstrated TMOs materials. Their band alignments make them promising candidates for heterojunction thin film devices for optoelectronic applications such as LEDs[28] and photodetectors (PDs).[24,29-32,33]

$SnO_2$is also a wide bandgap material and transparent in the visible spectral region. SnO_2 has been demonstrated as a useful material for visible-blind UV PD.[10–12]Reported SnO_2 based PD showed lower level of responsivity, especially at longer UV

wavelengths.[13]Achieving better crystal quality and fabricating one-dimensional SnO_2 nanostructures are the two areas, where the researchers have focused in order to get improved responsivity of the PDs.[9,14–16] Although PDs based on one-dimensional materials have been reported to have ultrahigh responsivity[14], their fabrication processes are complicated and difficult to scale. In this work, a thin-film SnO_2 PDs were fabricated using a flexible and scalable approach to fabricate nanoscale *p-n* heterojunctions with enhanced light absorption in the active material to improve the performance of UV PDs.

1.2 FIGURES OF MERIT

There are many important figures of merit which are used to compare the performance of different PDs. They are discussed briefly in this section.

(a) External Quantum Efficiency (EQE): EQE is the ratio of the number of free carriers generated per incident photon. EQE can be defined as

$$\eta = I/(e\times\Phi) \quad (1)$$

where I is the output current, e is the electron charge and Φ is the incoming flux of the radiation.

(b) Noise Equivalent power (NEP): It quantifies the sensitivity of a PD. A more sensitive PD has a smaller NEP. It is defined as the input power that produces a unity signal to noise ratio in a 1 Hz output bandwidth

(c) Photoresponsivity: R measures the gain of a detector system. The unit of it is A/W and it means output current generated per input optical power at any photon energy or wavelength.

$$R = I_{op}/ P_{in} \quad (2)$$

(d) Detectivity: It is inversely proportional to the term NEP and it evaluates the noise performance of PDs. Equation for detectivity is

$$D^* = R/\sqrt{(2eIdark)} \quad (3)$$

Where e is electron charge and I_{dark} is dark current.

(e) Transient response: Rise time and fall time represents the speed of the device, which is one of the most important figures of merit of PD. Rise time represents the time interval for the PD response to increase from 10% to 90% of the peak output. Fall time is the time interval for the response to fall from 90% to 10% of the maximum value.

1.3 Flexible Electronics technology and Self Powered property

Flexible electronics are of great interest now due to their light weight and shock resistance for use in portable and wearable device applications such as flexible displays, sensor arrays, curved circuits, curved detector arrays, sensor skins, and other large-area electronics. Their properties of flexibility, thinness and lightweight make them keep increasing attention by researchers.[34-36]The combination of flexibility and self-sufficiency of a UV PD enables the operation of portable or wearable sensing or monitoring devices without external power supplies, as well as possible application in energy harvesting systems.[15]

To the industrial community today, flexible electronics means flexible displays and X-ray sensor arrays. To researchers, flexible means conformally shaped displays and sensors, electronic textiles and electronic skin. Flexible electronics covers a wide spectrum of applications including flexible display, flexible solar cell, printed RFID, flexible lighting and others. Currently, it has been estimated that there are about 1500

worldwide research units working on various aspects of flexible electronics. Market analysis estimates the revenue of flexible electronics can reach 30 billion USD in 2017 and over 300 billion USD in 2028. Additionally, flexible interconnects enable the development of highly compact electronic packages (e.g. portable video cameras, automotive electronic systems, and medical equipment) with little "empty" volume, by

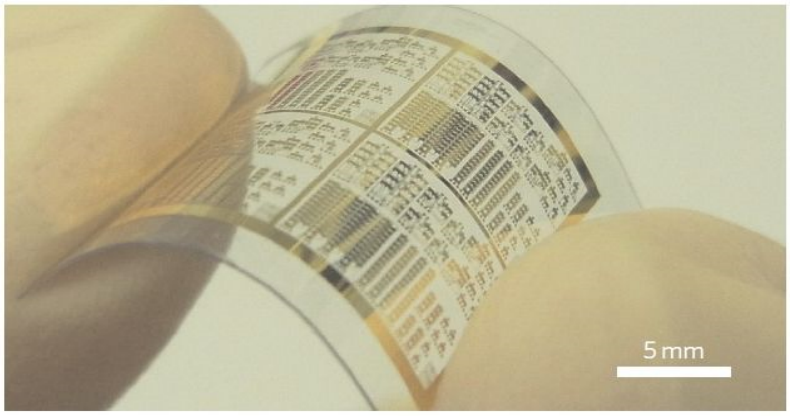

Figure.1: Illustration of a flexible substrate. Carbon nanotube thin-film transistors and integrated circuits on a flexible and transparent substrate. Image copyright: Dong-ming Sun, et al. ©2011 Macmillan Publishers Limited.

allowing for the use of discrete electronic modules connected by flexible strips that can be conformed to the irregular contours of the unit. Further, in applications where speed is critical, such as for chip carriers, the relatively low dielectric constant of organic substrates offers better performance, compared with ceramic chip carriers.

Nowadays, self-powered nanosystem is another attractive theme that can greatly enhance the adaptability and sustainability of such devices.A Self-powered Dynamic System [1,2]is defined as a system powered by its own excessive kinetic energy,renewable

energy or a combination of both. The particular area of interest is the concept of fully or partially self-powered dynamic systems, requiring zero or reduced external energy inputs. The exploited technologies are particularly associated with self-powered sensors, regenerative actuators, human powered devices, and dynamic systems powered by renewable resources (e.g. solar-powered airships) as self-sustained systems.

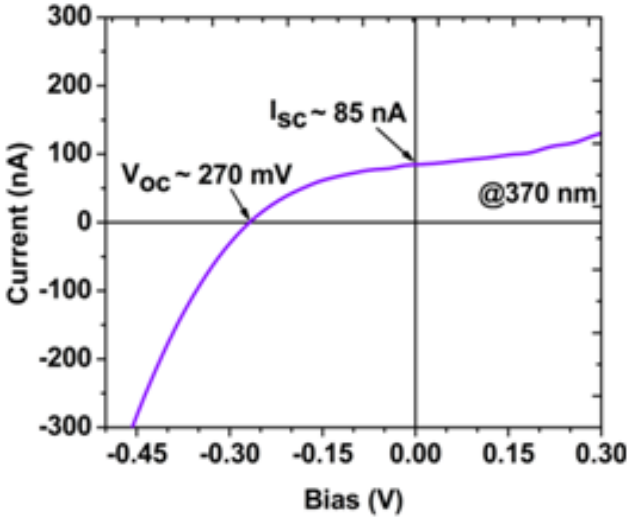

Figure 2: Example of demonstration of a self-powered device

A self-sustained system does not require maintenance (e.g. replacing the battery of the sensor at the end of the battery life). This is particularly beneficial in remote sensing and applications in hostile or inaccessible environments.

1.4 Group V-VI Chalcogenide materials based broadband photodetector

A chalcogenide is a chemical compound consisting of at least one chalcogen anion and at least one more electropositive element. Although all group 16 elements of the periodic

table are defined as chalcogens, the term chalcogenide is more commonly reserved for sulfides, selenides, and tellurides, rather than oxides. Group V-VI binary semiconductor compounds have been widely studied due to their specific properties and different structures have presented potential application in thermoelectric devices and optoelectronic devices[37,38].

Among them, antimony selenide (Sb_2Se_3), commonly crystallizing into one dimensional nanostructure, has the promising prospect of applying in various optical devices with its direct band gap (approximately 1.1eV), high optical absorption coefficient (>$10^5 cm^{-1}$)and high Seebeck Coefficient (1800 $\mu V K^{-1}$).[39-41] Due to the excellent optical and electrical properties, metal selenides drew attention of the research community over the last decade [42-46]. Due to these remarkable advantages, various solution-based synthesis techniques of Sb_2Se_3based one dimensional nanostructures have been reported during last decade.

Among the metal sulfides, antimony trisulfide (Sb_2S_3) has attracted attention for its application as a target material for television cameras [1,2], as well as in microwave[3], switching [4], and optoelectronic devices. Amorphous and crystalline thin films of antimony sulfide have been prepared using a wide variety of thin film deposition techniques, including: chemical bath deposition, electrodeposition, spray pyrolysis and vacuum thermal evaporation.

1.5 PRINCIPLE OF THz DETECTION BY FETs

THz detection by FET is possible due to nonlinear properties of the transistor, which rectifies the ac current, induced by the radiation. A dc voltage appears between source

and drain as a photoresponse from this induction.[47]. Both the carrier concentration and elelctron drift velocity are modulated by the radiation of plasma frequency. Some asymmetry between the source and drain is needed to induce photo voltage, otherwise the induced plasma wave at source and drain side will cancel each other and no photoresponse will appear. This necessary asymmetry can be achieved by: (i) designing the source and drain pad asymmetrically, (ii) feeding the incoming radiation in an

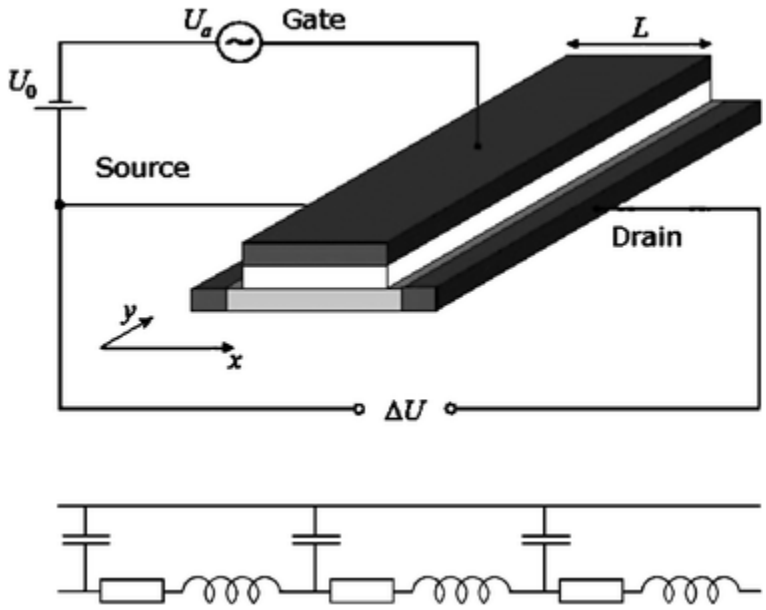

Figure 3. Schematics of a FET as a THz detector (above) and the equivalent circuit [Knap et. al][47]

asymmetric way,[47] (iii) by using special grating gate structure [48,49] or (iv) by applying drain bias and thus changing the boundary conditions[50,51]. In low frequency radiation, generally the THz radiation is coupled with contact pads and bonding wires.[52,53]Knap et. al has described the theory of terahertz detection by FET.[47]In presence of extreme

asymmetry between source and drain, let us assume that the incoming radiation is coupled between source and gate (This can be between gate and drain as well depending on the asymmetry).

(Fig. 3). There is no applied voltage between drain and source as well. Figure 3 shows the ac equivalent circuit of an FET. Channel resistance depends on the gate voltage through the electron concentration with a relation:

$$qn=CU \tag{4}$$

where q is the elementary charge, n is the electron concentration in the channel, C is the gate-to-channel capacitance per unit area, and U is the gate to channel voltage. In the absence of the drain current, $U = U_0 = V_g - V_{th}$, where U_0 is the voltage swing, V_g is the gate voltage, and V_{th} is the threshold voltage at which the channel is completely depleted. The kinetic inductances are due to the electron inertia and are proportional to electron effective mass. Incoming Radiation frequency ω defines two regimes of operation, and depending on the gate length L, these two regimes can be further sub-divided in another two regimes.

1. *High frequency regime:* when $\omega\tau > 1$, where τ is the electron momentum relaxation time, then high frequency regime occurs. In this regime, the kinetic inductances are very important, and the plasma waves will be excited like the RLC transmission line waves. The plasma waves, having velocity $s = \sqrt{(eU/m)}$ and a damping time τ will propagate the distance $s\tau$.

a. *Short gate ($L < s\tau$):*The channel serves as a resonator for plasma oscillations because the waves can reach to the drain side and forms a standing wave after getting reflected.In this regime, resonant detection is possible with the fundamental mode of frequency ~ s/L.

b. *Long gate ($L >> s\tau$):* The plasma waves decay before reaching the drain and apparently no photoresponse appears.

2.*Low frequency regime:*When $\omega\tau << 1$ the plasma waves are overdamped and the inductances in Fig. 3 become short-circuited, which makes the equivalent circuit as RC line. Instead of electron momentum relaxation time τ, it's properties depend on τ_{RC}, which is the RC time constant of the whole transistor. It was proved that,$s\tau_{RC} = L^2\rho C$, where ρ is the resistivity of the channel.[47]

a. *Short gate ($L < (\rho C\omega)^{-1/2}$):* This regime is the so-called "resistive mixer", where the ac current goes though gate to channel capacitance uniformly throughout the whole length of the channel. This regime can apply only for transistors with extremely short gates. This regime is exploited for non-resonant broadband detection and imaging.

b.*Long gate ($L >> (\rho C\omega)^{-1/2}$)*:In this regime, the induced ac current will leak to the gate at a small distance l from the source, and neither ac voltage, nor ac current will exist in the channel at distances beyond $l$from the source.

1.6 THz Imaging

The idea of using terahertz radiation for imaging and sensing, has been discussed for at least several decades[54]. many researchers speculated earlier that, the sub-millimetre waves can be used for seeing through fog or haze, locating objects hidden in camouflage, and detecting defects in optically opaque materials. More recently, this list of promising applications has grown to include package inspection, quality control, non-destructive testing, and spectroscopic characterization of materials[186]. Many of these ideas exploit the unique properties of terahertz radiation which include the transparency of common packaging materials such as cardboard and plastics, the sub-millimetre wavelength which permits imaging with a diffraction-limited resolution similar to that of the human eye, and the fact that many interesting materials exhibit unique spectral fingerprints in the terahertz range which can be used for identification and chemical analysis[54].Apart from all these applications, understanding the mechanism of coupling of radiation is another important application of THz imaging.

1.7 GaN based HEMT as THz detector

GaN is a wide bandgap semiconductor and does not suffer from undesirable background optical and thermal excitation unlike Si and GaAs. The GaN/AlGaN heterostructure FETs (HFETs) have extremely high electron concentration in the channel (exceeding 10^{13} cm^{-2}) due to the piezoelectric and the spontaneous polarization effects. The devices made of nitride materials are also capable of operating at high temperatures and harsh environments. These transistor devices with short gate lengths have a higher

plasma wave frequencyand better performance of gate modulation, which makes them good candidates for resonant THz detectors[45].

For conventional GaN/AlGaN HEMT, high gate and drain leakage currents due to surface states and trap state assisted tunneling are very common in HEMT and thus leakage suppression and high on/off ratio is desired to make a good HEMT[55,56]. Many techniques were followed so far to effectively suppress the leakage and minimize noise level[56-60]. Metal-Oxide-Semiconductor is an effective structure to suppress the gate leakage by creating a blocking insulating layer. But to reduce the leakage effectively and prevent the negative shift of threshold voltage, generally high-k dielectric materials such as hfO_2[61,62], Al_2O_3[63-66]and ZrO_2[67] were used. Not much work has been done on the use of SiO_2 for improving the HEMT performance reported[68].

Fabrication of the nano-dimensional structures is always challenging. Techniques such as wet chemical etching are not feasible for etching nanoscale, high aspect- ratio GaN nanostructures due to undercutting of the mask and sloped sidewalls. One of the most critical aspects of making high quality GaN nanostructure arrays using top-down approach (by plasma etch) is to design an etching protocol for producing high-aspect ratio structures while inducing minimal damage to the sidewalls and preventing the etch-mask erosion. These problems were surmounted by carefully designing the metallization mask, etch parameters, surface treatments and annealing treatments in this work.

1.8 Low Frequency Noise (LFN) Theory

Knowing the source mechanism of noise and characterizing and predicting noise are very important for circuit design[69]. Fundamental physical processes and external sources can

be responsible for introducing noise in the device or circuit. External sources can often be eliminated by shielding, filtering, and change of layout. Fundamental physical sources cannot be eliminated, but it is however possible to reduce them by proper design and fabrication of devices and also design of circuits. Noise coming from fundamental physical sources are shown in figure 4.

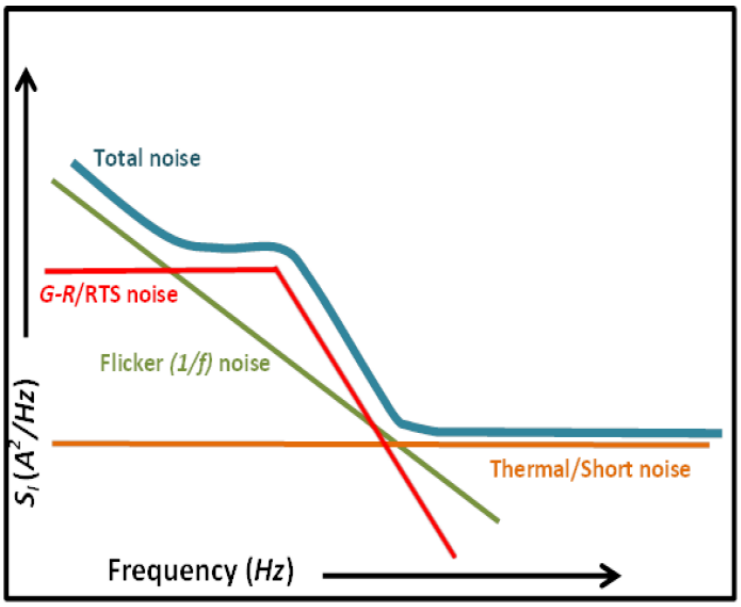

Figure 4. Schematic representation of a general noise spectrum in semiconductor devices. The total noise is a superposition of all the different noise sources. The typical cutoff frequencies are (i) over the THz region for thermal/short noise, (ii) below the GHz region for *G-R* noise, and (iii) below the MHz region for *1/f* noise.

Among all those different noise sources, 1/f (flicker noise) and Generation-recombination noise is more prominent in GaN based devices.

Generation-recombination noise is due to fluctuations in the number of free carriers in a semiconductor between different energy states within the forbidden bandgap. The traps generally exist due to the presence of defects or impurities in the crystal. It represents a typical noise source in semiconductor materials where carrier concentration can vary over many orders of magnitude. Typical examples of transitions are between

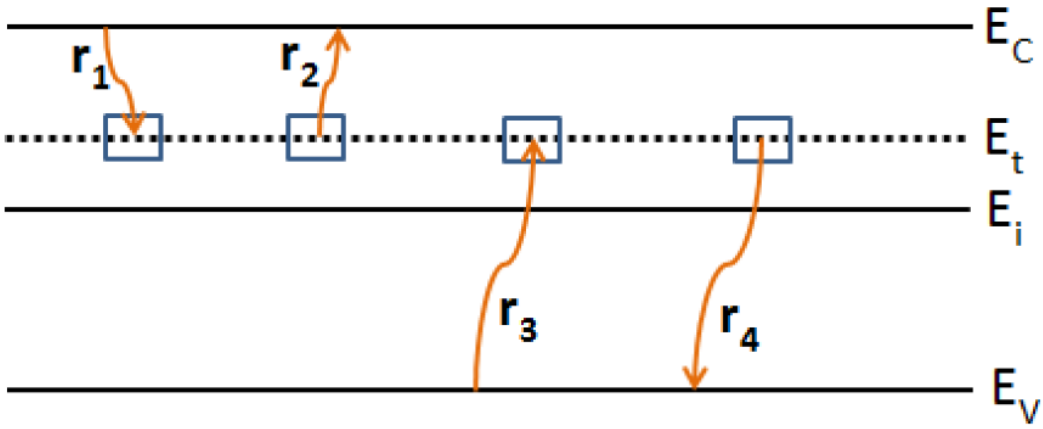

Figure 5. Free carriers can interact with traps by four processes: r1 electron capture, r2 electron emission, r3 hole capture, r4 hole emission. EC, EV, Ei and Et represents conduction band edge, valance band edge, intrinsic Fermi level and localized trap state (acceptor type) energy level respectively. [Ref: Deepak et. al[70]]

conduction band and localized levels in the energy gap, conduction and valence bands, etc.[70]If the Fermi-level is far above or below the trap level, then a few transitions take place that produce noise. When there are several *G-R* centers with different carrier life times, the resultant noise spectrum will be a superposition of several distributions.[70]

***1/f* noise** (flicker noise) is the most common noise type in the low frequency range. This noise is present in all semiconductor devices under biasing and cannot be eliminated completely. This noise is usually attributed to material failures or imperfections in

fabrication process. *1/f* noise power spectral density (PSD) is proportional to $1/f^{\gamma}$ with γ close to 1, usually in the range 0.7-1.3. The PSD for *1/f* noise is given by

$$S_I = \frac{KI^{\beta}}{f^{\gamma}} \quad (5)$$

where *K* is a constant and β is a current exponent. *1/f* fluctuations in conductance have been observed in the low-frequency part of the spectrum in most of the conducting materials and in a wide variety of semiconductor devices

1.9 Characterization Methods

- Morphological Characterization:SEM (Scanning Electronic Microscopy) and High resolution Bruker Dimension fastscan AFM (Atomic Force Microscopy) have been used to observe the surface image, grain size and shape and surface roughness of the nanostructured film.
- Structural and Compositional characterization:Rigaku smartlab XRD has been used to see the crystallinity of the deposited film. Transmission electron micrsocopy (TEM) image reveals more detailed description of the phase of the films. EDS (Electron dispersive X-ray spectroscopy) has been used to see the composition of the grown film. Raman and XPS spectroscopy have been used further to confirm the structural details of the semiconductor films
- Optical characterization: UV-Vis-NIR absorption spectroscopy and ellipsometry have been used to confirm the bandgap and thickness of the photoconductive film.Devices have been characterized for current-voltage (I-V) and external quantum efficiency (EQE) using a spectrally filtered light source. EQE system

was calibrated using a NIST-calibrated silicon photodiode and a total uncertainty of ± 5 % (fractional) is associated with measured EQE.

- Electrical characterization: Semiconductor parameter analyzer Agilent B1550A has been used to see all the electrical and temporal characteristics of the devices.
- Low Frequency noise measurement: LFN characterization for GaN based HEMTs has been done using SR 770 FFT spectrum analyzer.
- THz measurement:300 GHz focused beam was irradiated on the device and computer controlled nanopositioning stage (NanoMax 341) was used to observe the spatial variation dependence responsivity of the device. The induced photovoltage between source to drain was identified by standard lock-in technique. To apply the gate and drain bias voltage to the FET, tunable battery was used to minimize the low frequency noise and external disturbance.

This chapter gave an introduction on Ultraviolet photodetection, different methods and materials used and also the figures of merit for the PDs. It also discussed about the significance of group V-VI chalcogenides nanostructures. It gives an idea about the Terahertz detection principle and basic theory, THz imaging overview and overview on Low frequency noise theory for GaN/AlGaN HEMTs.

In the second and third chapters, UV photodetectors based on NiO/ZnO p-n junction photodiode and SnO_2 based MSM photodiode are discussed respectively. Chapter 4 and 5 presents the broadband photodetector by 2 different Group V-VI chalcogenides, namelyAntimony Selenide and Antimony Sulphide. Chapter 6 presents effect of radiation

coupling thorough contact pad and bonding wire on THz imaging by GaN/AlGaN multi-channel FET. And chapter 7 describes the comparative study of electrical and Low frequency noise characterization of GaN/AlGaN HEMT and MOS-HEMT.

CHAPTER TWO: SELF-POWERED p-NiO/n-ZnO HETEROJUNCTION ULTRAVIOLET PHOTODETECTORS FABRICATED ON PLASTIC SUBSTRATES

Flexible electronics are of great interest now due to their light weight and shock resistance for use in portable and wearable device applications such as flexible displays, sensor arrays, curved circuits, curved detector arrays, sensor skins, and other large-area electronics.[71-75] Self-powered UV PDs have also attracted considerable attention in recent years for their ability to operate sustainably without external power for the optical communication, environmental monitoring, missile plume detection, and digital imaging applications.[15,75-80]The self-powered PDs that have been demonstrated rely on the photovoltaic effect produced by the built-in electric field of a junction.[75-80] Based on interface features, self-powered PDs can be categorized into two types: Schottky junctions and p-n junctions. In both structures, the photo-generated electrons and holes are separated by the build-in electric field and collected at cathode and anode, respectively.

As a representative II-VI group semiconductor, ZnO is intrinsically n-type with 3.3 eV direct band-gap, 60 mV exciton binding energy, and additionally high radiation and chemical resistance.[81,82] For the UV PD applications, junctions that are composed of ZnO have been investigated extensively due to the excellent electrical and optical properties of ZnO.[78-81,83]Despite the advantage of simple fabrication process of ZnO based Schottky

junction PDs, p-n junction structure appears to be more promising due to its stability, lower applied filed and faster response.[78,83,84]Among the variety of p-type materials that have been employed to form p-n junction with ZnO, p-NiO stands out due to its band alignment with ZnO in UV PD applications.[24,85,86]

The combination of flexibility and self-sufficiency of a UV PD enables the operation of portable or wearable sensing or monitoring devices without external power supplies, as well as possible application in energy harvesting systems.[15] In this paper, we demonstrate radio frequency (rf)-sputtered p-NiO/n-ZnO heterojunctions as self-powered UV PDs. The devices are fabricated on transparent, conducting, and flexible indium-doped tin oxide (ITO) coated PET (polyethylene tetraphthalate) substrates and deposited at low temperature. Top metal contacts of the p-n heterojunctions are engineered to be UV transparent, allowing illumination of devices through both the PET/ITO and top metal contacts. Chemical, structural and optical properties of NiO and ZnO thin films were characterized. The measured performance of the PDs shows self-powered properties driven by photovoltaic effect, as well as excellent external quantum efficiency (EQE), responsivity, detectivity and UV to visible rejection ratio.

In this work, radio frequency (rf)-sputtered p-NiO/n-ZnO heterojunctions as self-powered UV PDs were demonstrated. The devices are fabricated on transparent, conducting, and indium-doped tin oxide (ITO) coated PET (polyethylene tetraphthalate) substrates and deposited at low temperature. Top metal contacts of the p-n heterojunctions are engineered to be UV transparent, allowing illumination of devices through both the PET/ITO and top metal contacts. Chemical, structural, and optical properties of NiO and

ZnO thin films were characterized. The measured performance of the PD shows self-powered properties driven by photovoltaic effect with very fast temporal response, as well as excellent external quantum efficiency (EQE), detectivity, and UV to visible rejection ratio. The PDs have been fabricated on PET substrates using rf sputtering and the deposited thin films devices have been characterized.

2.1 Experimental Details

The NiO thin films were deposited on commercially available PET (polyethylene terephthalate)/ ITO (indium doped tin oxide) substrate (from Sigma Aldrich) by rf-sputtering from a NiO target at or below a base pressure of 5×10-6 Torr. A gas flow of Ar and O^2at 40 standard cubic centimeters per minute (sccm) and 4 sccm, respectively, and 200 W rf-sputtering power were maintained during the process and the substrate temperature was kept at 70°C. The target was cleaned for 10 minutes followed by 2 hours of deposition to reach the film thickness of ≈105 nm.

Similarly, 125 nm thick ZnO film was were deposited with 50 sccm Ar and 100 W rf-power atroom temperature for 50 minutes. The film thickness for both NiO and ZnO films were confirmed by ellipsometry and profilometry measurements. The metal oxide deposition recipe was optimized to minimize the bending of the substrate during the deposition. Corners of the PET/ITO substrates were intentionally left blank during NiO and ZnO depositions to accommodate the connections of anode for future optoelectronic measurements. Ultra-thin metal contacts, 10 nm Ti/ 3 nm Au, were deposited through a shadow mask having an array of circular openings of 4 mm on top of the p-NiO/n-ZnO

heterojunctions using e-beam evaporation. In order to obtain a smooth thin metal contact, Ti and Au layers were deposited using a very low deposition rate of 0.5 A/s and 0.2 A/s, respectively.

Sputtering conditions for NiO and top metal contact were kept unchanged to optimize the Sputtering power of ZnO so that the substrate has less bending. RF sputtering power for ZnO from 300 W to 100 W and the bending effect decreased gradually as shown in Figure 6.

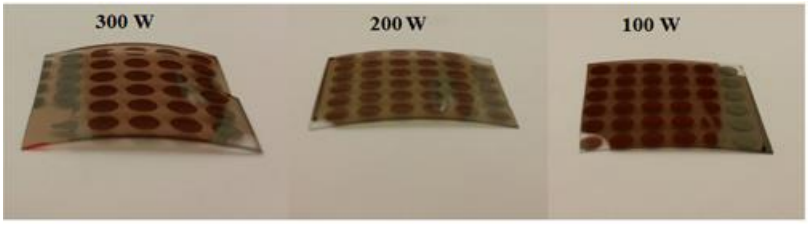

Figure. 6: Reduction of substrate bending with the decrease in applied RF bias while ZnO sputtering

Figure 7(a) shows the schematic of the device structure whereas Fig. 7(b) shows the optical image of the same, demonstrating its transparency and flexibility.

2.2 Film and Device Characterization Method

The surface morphology and roughness of the deposited NiO and ZnO films were studied with high-resolution atomic force microcopy (AFM) using a Bruker Dimension FastScan system. Crystallinity of the deposited films was characterized using Rigaku ray

diffraction (XRD) system. UV-VIS-NIR absorption spectroscopy (Lambda 950 Perkin Elmer) was used to determine optical properties of the sputtered films. From the measured absorption spectra, bandgaps of the sputtered NiO and ZnO films were

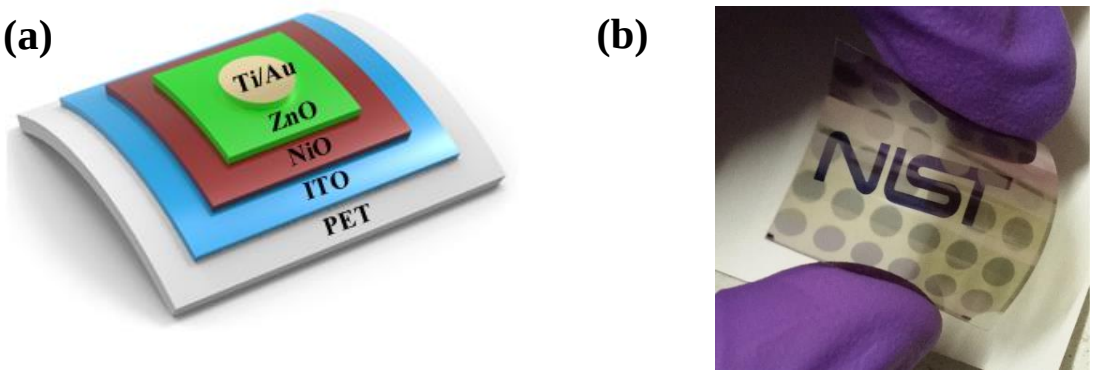

Figure 7. (a) Schematic of the p-NiO/n-ZnO PD on PET/ITO substrate. (b) Actual optical image of the device exhibiting flexibility of the substrate.

extracted using Tauc plots. Vacuum ultraviolet variable angle ellipsometry (VUV-VASE) measurements were also performed to confirm the bandgaps obtained from absorption spectroscopy. X-ray photoelectron spectroscopy(XPS) was used to validate the chemical composition of the deposited NiO and ZnO films and the spectra were collected in a Kratos Axis Ultra DLD spectrometer with an Al Ka monochromatic x-ray source and an analyzer with 0.1 eV energy steps and 20 eV pass energy for high resolution scans. The XPS spectra were energy calibrated to the adventitious C 1s binding energy at (284.5±0.3) eV. Figures of merit of the p-NiO/n-ZnO heterojunction PD devices were measured under a spectrally filtered light source at different biases. The system was

calibrated using a NIST calibrated silicon photodiode and a total uncertainty of ±5 % (fractional) is associated with measured EQE.

For transient response, PD devices were illuminated using Panasonic Aicure UJ30 system equipped with 365 nm UV light emitting diode (LED) and currents were monitored with/without UV light using an Agilent B1500A semiconductor device parameter analyzer.

2.3 Results and Discussion

The stress induced during the film deposition has resulted in bending of PET/ITO substrates and the bending effects could be minimized by reducing rf power during sputtering (See Fig.6). Other parameters such as working pressure, substrate temperature etc. can also affect the film quality and no optimization has been done in order to

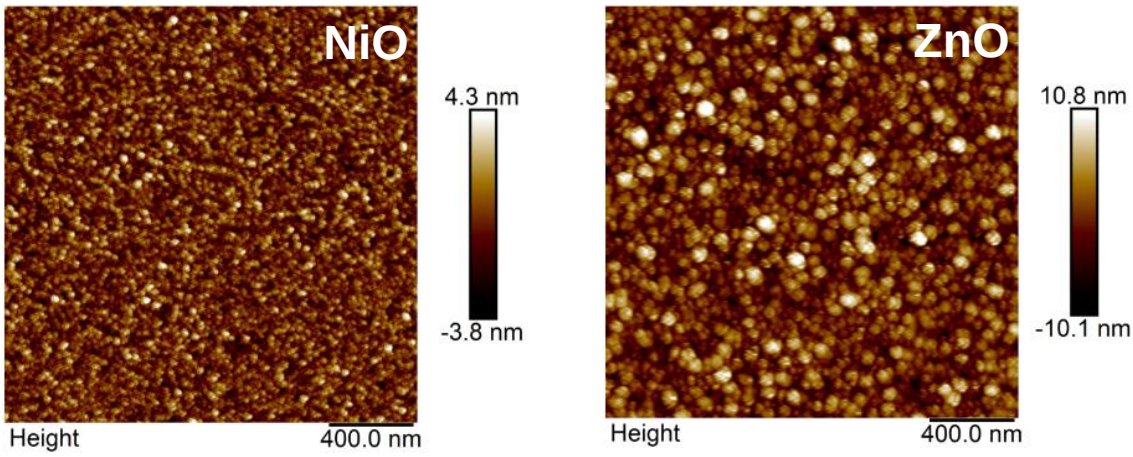

Figure 8. AFM images of sputtered NiO and ZnO thin films. Nano-grains are clearly evident from AFM images.

correlate the material properties with the device performance. Figure 8 shows high-resolution AFM images of sputtered NiO and ZnO thin films which exhibit nanoscale-sized grains and smooth surface. The estimated granularities of the deposited NiO and ZnO films are 20±6 nm and 50±14 nm, respectively. The measured root mean square (rms) roughness of the films is 1.13 nm for NiO and 3.24 nm for ZnO. The small grain size and smooth surface of prepared NiO and ZnO films allow them to form abrupt p-n heterojunctions. Figure 9(a) shows the results of a grazing incidence XRD measurement of the fabricated device. All the diffraction peaks, except those from the PET/ITO substrate, can be assigned as cubic NiO (JCPDS-78-0643) or hexagonal wurtzite ZnO structure (JCPDS 36-1451), accordingly. The results indicate that the prepared NiO and ZnO films are polycrystalline in nature. The small grain sizes of the films can be deduced from the broad detected peaks, which agree well with the AFM results. X-ray diffraction scans were also done on sputtered NiO and ZnO films separately on silicon substrate in the same deposition condition of that of fabricated device to confirm the crystallinity of both the films. Following figure shows the clear sharp peaks confirming the presence of crystalline NiO and ZnO films.

Figure 9(b) shows the bandgaps of the NiO and ZnO thin films with Tauc plots measured by UV-vis spectroscopy. The bandgaps are estimated by extrapolating the linear region of the Tauc plots of $(\alpha h\nu)^{1/2}$ versus $h\nu$ to $h\nu = 0$, where α is the absorption coefficient and $h\nu$ is the photon energy. The estimated bandgaps are 3.74 eV and 3.25 eV for NiO and ZnO, respectively. Bandgap was also calculated from Ellipsometry to confirm the measurement

from absorption spectroscopy. Table 1 shows the bandgap obtained from absorption spectroscopy and ellipsometry. The values are also consistent with the ellipsometry data.

Table1: Bandgap of NiO and ZnOfrom absorption spectroscopy and ellipsometry

Calculated Bandgap	Absorption spectroscopy	Ellipsometry
ZnO	3.74±0.04 ev	3.69±0.03 ev
NiO	3.25± 0.01 ev	3.29±0.03 ev

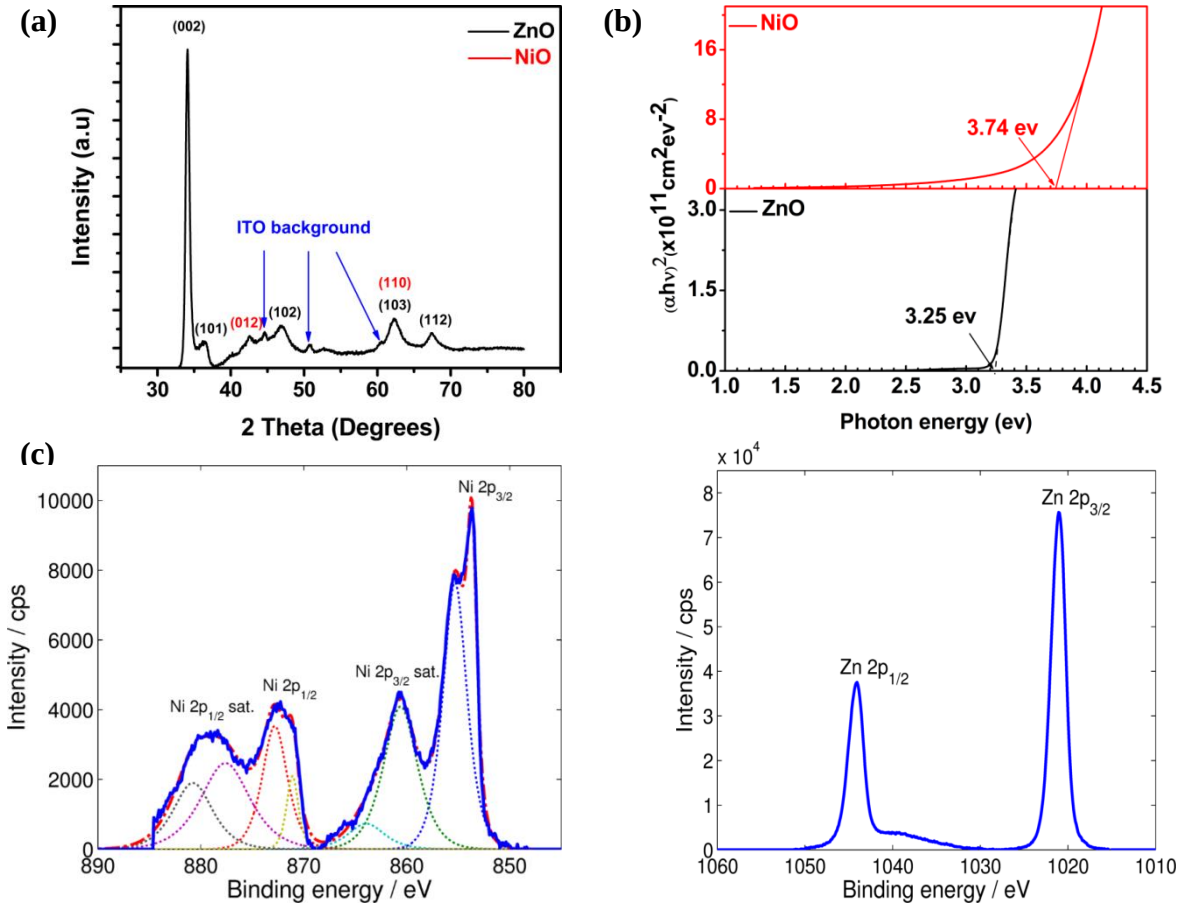

Figure. 9. (a) XRD scans taken from the fabricated device show diffraction peaks coming from different planes of NiO and ZnO. (b) Direct energy bandgap from absorption spectroscopy (Tauc plot). Both materials have direct energy bandgap. (c) XPSdata for both NiO and ZnO films.

The wide bandgaps lead to the transparency of the prepared films in the visible spectrum and will determine the risingand falling edges of the EQE patterns under various reverse bias voltages. Figure 9(c)shows the high-resolution XPS spectra of sputtered NiO and

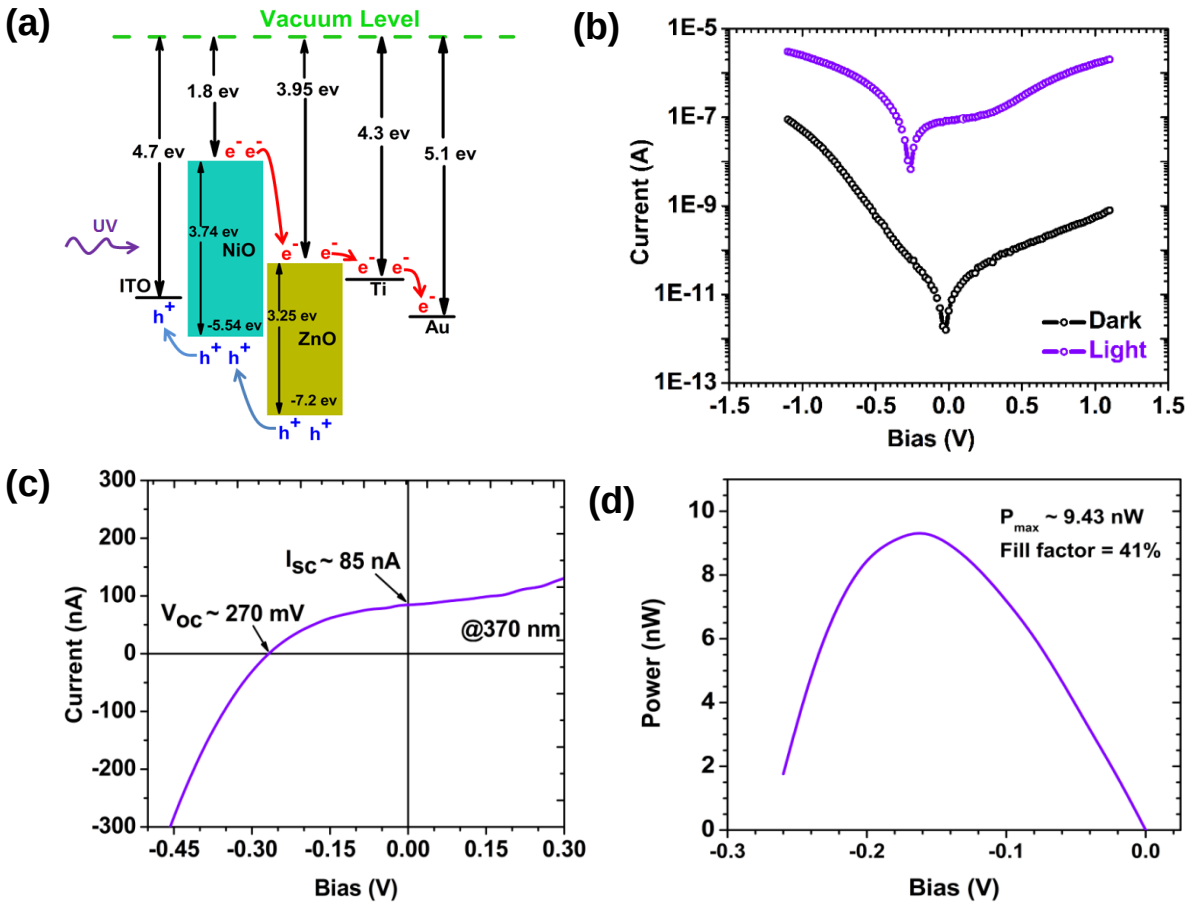

Figure 10. (a) Energy levels of different components of PDs. Work function of all the components and bandgap of NiO and ZnO films are shown. Under UV illumination, photogenerated holes and electrons in the depletion region of junction are collected by ITO side and metal contact respectively.(b) Diode characteristic of the device: current-voltage curve both in dark and UV illumination at 370 nm (through PET/ITO layer). The rectifying nature of the diode as well as the photoresponse is evident from the I-V data. The Photoresponse factor, S was found to be approximately ~2663. Dark current on-off ratio (IF/IR) is found to be ~111 and Ideality factor of the diode is ~8.14. Inset shows the device schematic along with the reverse bias connection. (c) self powered behavior of the device. Voc = 270 mV and Isc = 85 nA and (d) Change of power in the voltage range o to Voc.

ZnO films at the Ni 2pand Zn 2p regions, respectively. Wide range low resolution scans (1 eV steps with 160 eV pass energy) were used to check for contamination. In both NiO and ZnO films, the only elements identified were the desired metal oxide and carbon, attributed to surface contamination; no Ni was found in the ZnO film, nor Zn in NiO film. As seen in spectrum of NiO, the Ni 2p 3/2 peak appears at a binding energy of 853.7± 0.1 eV, with the binding energy and multiplet splitting characteristics of Ni^{2+}, as in NiO.[87]In the spectrum of ZnO, the Zn 2p 3/2 peak at 1021.1 ±0.1 eV, with 23.1 eV splitting from its 2p 1/2 component, is consistent with reported XPS data of other ZnO films.[88]To illustrate the mechanism of the self-powered PDs, Figure 10(a) shows the band diagrams of the fabricated device. Under UV illumination, electron-hole pairs are generated in the depletion region of the device. At the interface of NiO and ZnO films, the built-in electric field across the depletion region separates the photo-generated electron-hole pairs and drives them out of the depletion region. The drifted electrons then diffuse through the ZnO layer to be collected at the Ti/Au cathode. Similarly, the photo-generated holes reach to the ITO anode through the NiO layer.

Figure 10(b) shows the typical current-voltage (I-V) characteristics of p-NiO/n-ZnO heterojunction device in the dark and under UV illumination UV from the back side (PET/ITO) at room temperature. The applied voltage ranges from -1.2 V to 1.2 V, where the positive voltage means reversed bias. The diode shows an obvious rectifying behavior and a rectification ratio of ≈111 at ±1.2 V is calculated from the dark current. To evaluate the ideality factor of the diode, the dark I-V response in the low bias regime can be modeled using the following approximated equation:

$$I=I_0 e^{(\frac{qV_d}{\eta KT})} \quad (6)$$

Where I is the current through the diode, I_0 is the dark saturation current, V is the applied voltage across the diode, n is the ideality factor, k is the Boltzmann's constant and T is the temperature in kelvin. The ideality factor and the reverse saturation current have been extracted from the slope and intercept of the straight line region of ln(I)–V plot, respectively. The obtained ideality factor n = 3.96 is greater than its normal range (1 < n< 2).

It implies that the transport mechanism is not dominated by the thermionic emission and it can be inferred that defects exist in the quasi-neutral region as well as in the junction which can be responsible for the carrier recombination at the junction. An enhancement of current at both forward and reverse biases is observed under UV illumination. The increased current results from the photo generated carriers within the depletion region which are being extracted in their respective contacts. To quantify the performance of thePD, the photoresponse factor (S) which can be defined as

$$S = \frac{I_{light} - I_{dark}}{I_{dark}} \quad (7)$$

where I_{light} is the current under UV illumination and I_{dark} is the dark current at the same biasvoltage, has been measured. The fabricated PDs exhibit an excellent S ≈2700 at 1.2 V at 370 nmwavelength, much higher than that of other PDs based on oxide films, much higher than that of other PDs based on oxide films.[89-91]

Figure 10(c) shows the photovoltaic (PV) properties of the device under UV excitation. The open circuit voltage (V_{oc}) which is the maximum voltage available from a PV cell at zero current and short-circuit current (I_{sc}) which is the current when the voltage across the

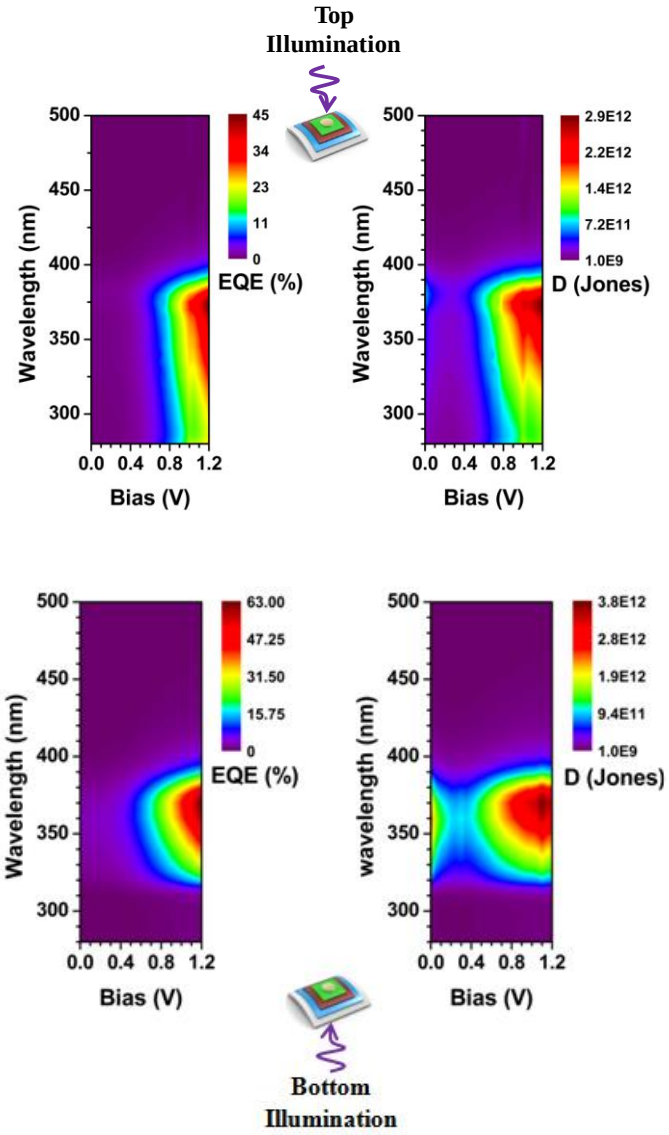

Figure 11: Device performance: (a) measured EQE and detectivity of the PD as a function of applied reverse bias with (a) light illumination through the Ti/Au contact. The maximum EQE reaches to 45% at 370 nm with a reverse bias of 1.2 V. (b) light illumination through PET/ITO side. The EQE reaches to a maximum value of 63% at 370 nm

cell is zero, are measured to be 270 mV and 85 nA, respectively. The PV effects make the fabricated devices suitable for self-powered PD application. Figure 10(d) shows the calculated self-generated power with the forward bias in the range of 0 to V_{oc} (270 mV). The maximum power point of curve is found at a voltage of V_m=0.16 V and current I_m=50.8 nA, yielding a maximum output power of 9.43 nW. The fill factor which is ratio of $V_mI_m/V_{oc}I_{sc}$ has been calculated to be ~ 41% for the device.

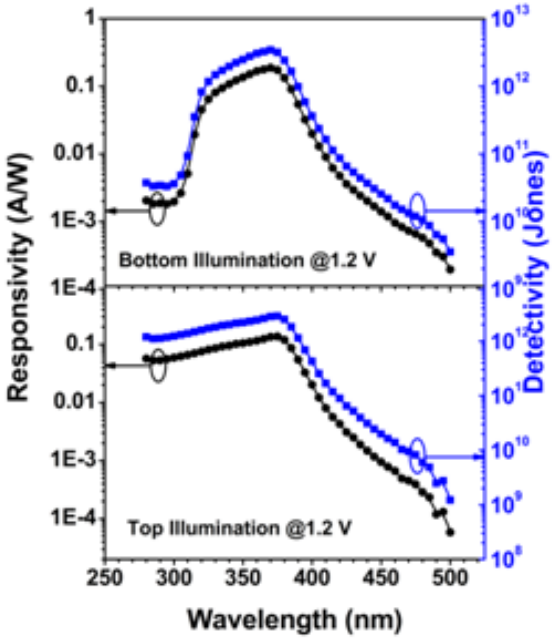

Figure 12: Calculated responsivity (left-axis) and detectivity (right-axis) of the device at 1.2 V for bottom illumination (on top) and top illumination (bottom figure). Maximum responsivity reaches to 0.19 A/W at bottom illumination (through PET/ITO layer)

EQE of NiO/ZnO devices have been measured at an applied reverse bias from 0 V to 1.2 V under top illumination (i.e., through Ti/Au metal contacts) as shown in Fig. 11(a).

The light spectrum spans from 280 nm to 500 nm. The obtained device spectral response is normalized tothe measured photocurrent of a NIST-calibrated Si photodetector under the identical illumination condition. At an applied reverse bias of 1.2 V, the maximum EQE reaches to ≈45% at 370 nm wavelength (Fig. 11a). Detectivity (D^*)is another important specification that characterizes the capability of PDs to detect the weakest light signal. By regarding the dark current as the major component of the noise, the specific detectivity is defined by the expression:

$$D^* = \frac{R_\lambda}{\sqrt{2eI_{dark}}} \quad (8)$$

Where e is the electron charge, $R_\lambda$is the responsivity at wavelength λ and I_{dark} is the measured dark current at the same reverse bias of the used responsivity.[24]The responsivity (R_λ), the ratio of detected photocurrent to incident light intensity, shows the maximum value of ≈0.14 A/W at370 nm at a reverse bias of 1.2 V (Fig. 12). The calculated detectivity of the fabricated device at370 nm reaches to a maximum of 2.9 × 10^{12}cm.$\sqrt{\ }$Hz/W or Jones.

Performances of the PDs are also measured while illuminating through the PET/ITO side (i.e., bottom illumination). At the reverse bias of 1.2 V, the EQE reaches ≈63% at 370 nm (Fig. 11b). The calculated maximum D^* and R_λ are found to be 3.8 × 10^{12}cm. $\sqrt{\ }$Hz/W and ≈ 0.19 A/W, respectively (Figure 12). The distinct but higher performance of the PD under bottom illumination as compared to the top illumination is likely due to the higher transparency of the PET/ITO as compared to ultrathin Ti/Au electrode around the UV regime of 370 nm (Fig. 13). Additionally, the device shows a sharp cut-off wavelength at

320 nm under bottom illumination condition, which is due to the precipitous drop in the UV transparency profile of the PET/ITO around 320 nm. Absorption spectroscopy of PET/ITO substrate shows that there is no transmission of light below 315 nm wavelength i.e., all the light gets absorbed below that wavelength (Fig. 13). Thus the EQE of bottom

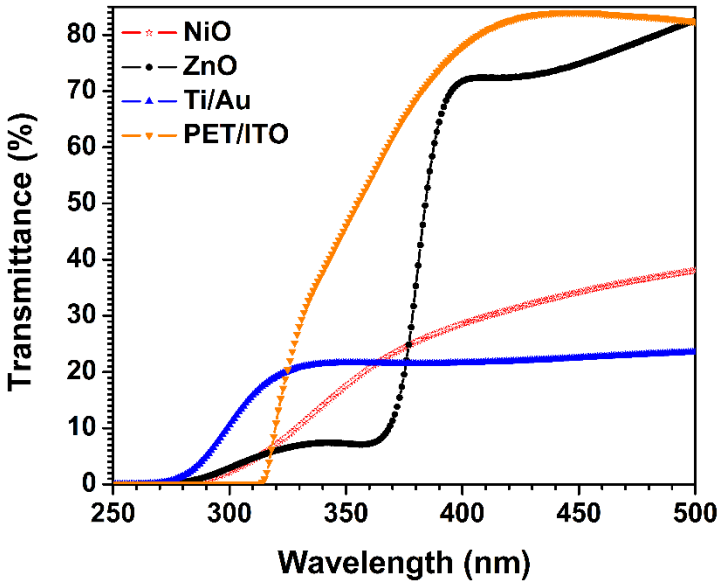

Figure 13. Transmittance spectra of NiO, ZnO, Ti/Au and PET/ITO

illuminated device (through PET/ITO) in figure 11(b) shows a sharp cut-off at this wavelength. In case of ultrathin Ti/Au metal contacts, there is still some transmission of light below 280 nm as opposed to PET/ITO. That is why the device shows some photoresponse below 315 nm wavelength. Above 325 nm, PET/ITO shows more transmittance than Ti/Au and thus the device shows higher quantum efficiency for the former than the latter at higher wavelength. Transmittance data of NiO and ZnO are also shown in figure 13.Fig.14 shows the temporal response of the fabricated photodetectors

under 365 nm UV illumination at room temperature. The photocurrent increases very rapidly upon exposure to UV radiation, stays essentially constant during the UV exposure, and decays much faster when UV is turned off. The rise time (t_r) for the photocurrent to reach from 10% to

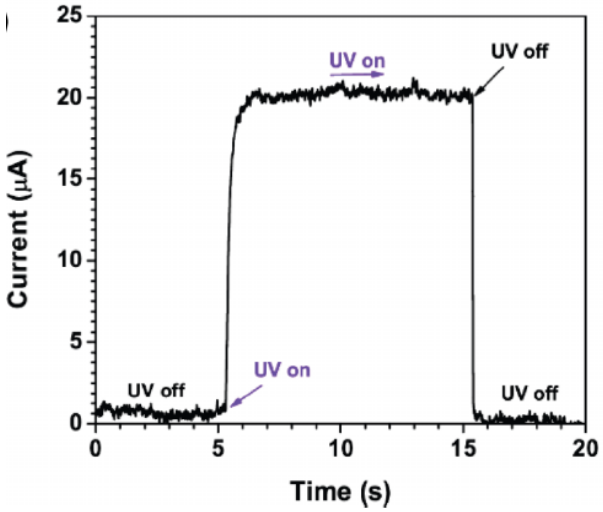

Figure 14. Time-resolved photocurrent response to a 10 s light pulse from 365 nm UV light source at 1.2 V reverse bias. Dark currents have been subtracted. The device has been illuminated through PET/ITO side.

90% of its maximum value is ≈323 ms and the decay time (t_d) for the photocurrent to decrease from 90% to 10% of the peak value is ≈12 ms. The slow response of the PD is related to strong carrier trapping and these photoconductors exhibit comparable or better temporal response than other oxide based PDs[16,18] indicating high quality engineered metal oxide heterojunction with excellent sensitivity. The solar blindness is usually quantified in terms of rejection ratio which is defined the ratio of the photoresponse of a PD in the UV light to the visible light. A high UV-to visible is always desirable for the

detector which shows very weak response to the solar visible spectrum and no filter is needed for UV detection. The devices demonstrate an excellent UV-selective sensitivity with maximum UV-to-visible rejection ratio ($R_{\lambda=370\ nm}/R_{\lambda=450\ nm}$) of ≈183 (Fig. 15).

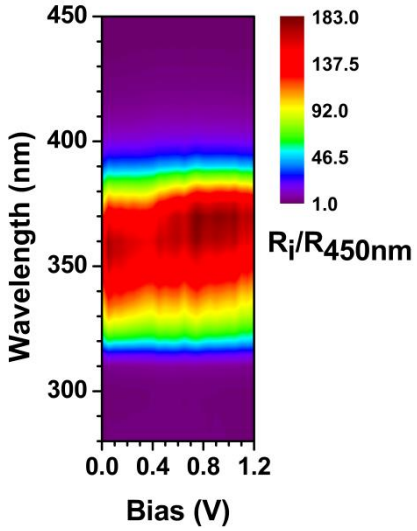

Figure 15. UV to visible rejection ratio($R_i/R_{\lambda=450nm}, i = 280 - 450\ nm$) for the bottom illumination (through PET/ITO side)

Finally, the performance of PDs in this work[92] and some previously reported data are summarized in Table 2 for comparison.

2.4 Conclusion

In this work, self-powered photodiodes based on low-temperature rf-sputtered NiO and ZnO on PET/ITO substrates were demonstrated. The architecture of the device and the UV transparency of the substrate allow the illumination through both the top Ti/Au metal

and bottom PET/ITO contacts side without significantly affecting the device performance. The fabricated *p*-NiO/*n*-ZnO heterojunction exhibits excellent UV

Table 2: Performance matrix of various metal oxide based PDs reported in the literature

System	**Structure**	**Growth method**	**Bias(V)**	**Max. R_λ(A/W)**	**Max. UV-Vis. rej.(R_λ/R_{400})**	**Self-powered**	**Flexible**
NiO-ZnO[79]	Nanorod	Sol-gel	0	0.44m	-	Yes	No
ZnO-MgO-GaN[78]	Nanorod	Sol-gel	0	0.23	34.5	Yes	No
NiO-ZnO[26]	Thin film	Sol-gel	5	21.8	1600	No	No
NiO-ZnO[93]	Coaxial nanowire	Sol-gel	3.5	7.37	154	No	No
ZnS-ZnO[94]	Nanofilm	Hydrothermal	10	0.165μ·cm^2	48	No	Yes
NiO-ZnO (current work)	**Thin film**	**Sputtering**	**1.2**	**0.19**	**183**	**Yes**	**Yes**

sensitivity with a reasonable on/off ratio as well as self-powered behavior with V_{oc} of 270 mV, I_{sc} of 85 nA, and fill factor of ~41%. The maximum EQE of 63%, detectivity of 3.8×10^{12}cm.√Hz/Wand responsivity of 0.19 A/W are achieved at 370 nm under a reverse bias of 1.2 V. Considering the advantages of low-temperature processable fabrication with large visible-blind UV selectivity detection as well as very fast temporal response, these heterojunction PDs have potential for use in large-area UV PD applications.

CHAPTER THREE: HIGH-PERFORMING VISIBLE-BLIND PHOTODETECTORS BASED ON SnO_2/CuO NANO-HETEROJUNCTIONS

Transparent oxide semiconductors (TOS) have attracted considerable attention in recent years, due to their versatile applications in transparent thin-film transistors,[1,2] transparent electrodes,[3] and optoelectronics,[4–6]. Visible-blind ultraviolet (UV) photodetectors (PDs) are of particular interest, owing to their broad application in digital imaging, missile plume detection, optical communications, and biomedical sensing.[7–9] Due to its wide bandgap and consequent transparency in the visible spectral region, SnO_2 has been demonstrated as a useful material for visible-blind UV photon detection.[10–12]

Typical *n*-SnO_2PDs work as photoconductors with electrons as the majority carriers. In a photoconductor, absorption of photons with energy larger than the bandgap energy generates free carriers, leading to an increase in conductivity for a period known as the persistence time. The device conducts a single carrier type, and the persistence time can be lengthened by trapping of the non-conducting carrier type, leading to photoconductive gain and quantum efficiency of greater than 100%. At a specific operation bias, the photocurrent is measured as the response of the PD, which can be used to calculate the EQE (external quantum efficiency) and responsivity of the device.

Current SnO_2 thin-film PD technology is limited by low responsivity, especially at longer UV wavelengths.[13] Efforts to improve device performance have focused on achieving better crystal quality and building one-dimensional SnO_2 nanostructures.[9,14–16] The

reported ultrahigh responsivity[14] of SnO_2 based PDs indicates that SnO_2 is a promising material for high-performing PDs. Here thin-film SnO_2 PDs were fabricated using a novel, facile, and scalable approach to fabricate nanoscale *p*-*n* heterojunctions with enhanced light absorption in the active material to improve the performance of UV PDs. Nanorod-based heterojunctions consisting of *p*-CuO and *n*-SnO_2 have been previously developed for applications such as gas sensors.[17,18].

In this work[95] ,the significant performance enhancement of SnO_2 thin film ultraviolet (UV) photodetectors (PDs) through incorporation of CuO/SnO_2*p*-*n* nanoscale heterojunctions was shown. The nanoheterojunctions are self-assembled by sputtering Cu clusters that oxidize in ambient to form CuO. The performance improvements were attributed to enhanced UV absorption, demonstrated both experimentally and using optical simulations, and electron transfer facilitated by the nanoheterojunctions. The peak responsivity of the PDs at a bias of 0.2 V improved from 1.9 A/W in a SnO_2-only device to 10.3 A/W after CuO deposition. The wavelength-dependent photocurrent-to-dark current ratio was estimated to be ~ 592 for the CuO/SnO_2 PD at 290 nm. The morphology, distribution of nanoparticles, and optical properties of the CuO/SnO_2 heterostructured thin films are also investigated.

3.1 DEVICE FABRICATION AND RESULT DISCUSSION

The SnO_2 thin films were rf-sputtered using a SnO_2 target on sapphire substrates in a Denton[1] Vacuum Discovery 550 sputtering system. The base pressure was kept at or

below 6.7 x 10^{-4} Pa (5 x 10^{-6} Torr), and the substrate temperature was maintained at 325˚C to yield uniform films. The thickness of the deposited SnO_2 was measured using a J. A. Woollam M2000 ellipsometer and estimated to be (95 ± 2) nm.

The Cu NP clusters were deposited on the SnO_2 films by rf-sputtering at room temperature. The deposition time was 185 seconds, and a shadow mask was used to form square-shaped clusters composed of self-assembled nanoparticles with a nominal height of 40-50 nm rather than continuous cluster films. The total areal size of the Cu clusters was 200 µm x 200 µm, and they were spaced by 200 µm, as shown in Figure 16(a). Oxidation of the Cu nanoparticles occurred spontaneously during and immediately following the deposition, resulting in the formation of CuO NPs. X-ray photoelectron spectroscopy (XPS) measurements indicated that the final NP clusters are primarily (> 95 %) composed of CuO, as shown in Figure 16(b). Electron beam evaporation was used to deposit Ti/Al/Ti/Au interdigitated electrodes (IDEs) as the final step in the PD fabrication process. Figure 16(a) shows a device schematic of the entire structure.

The surface morphology of the SnO_2 and SnO_2-CuO films was measured using a Bruker Dimension FastScan atomic force microscope (AFM). Figures 16(b) and 16(c) show high-resolution AFM images of the bare SnO_2 film and the SnO_2 with a top layer of self-assembled CuO NPs. The measured root mean square (rms) surface roughness of the bare SnO_2 film was 1.8 nm, and the rms value increased to 13.8 nm after the addition of the CuO NPs. The grain sizes of the SnO_2 film and the CuO nanoclusters were estimated as (32.9 ± 13) nm and (74.6 ± 25) nm, respectively. A rough statistical analysis

performed on the image in Figure 16(c) resulted in an average CuO NP surface density of 65 μm^{-2} and an average particle height of 45 nm. These estimated parameters were used in the FDTD simulations described below.

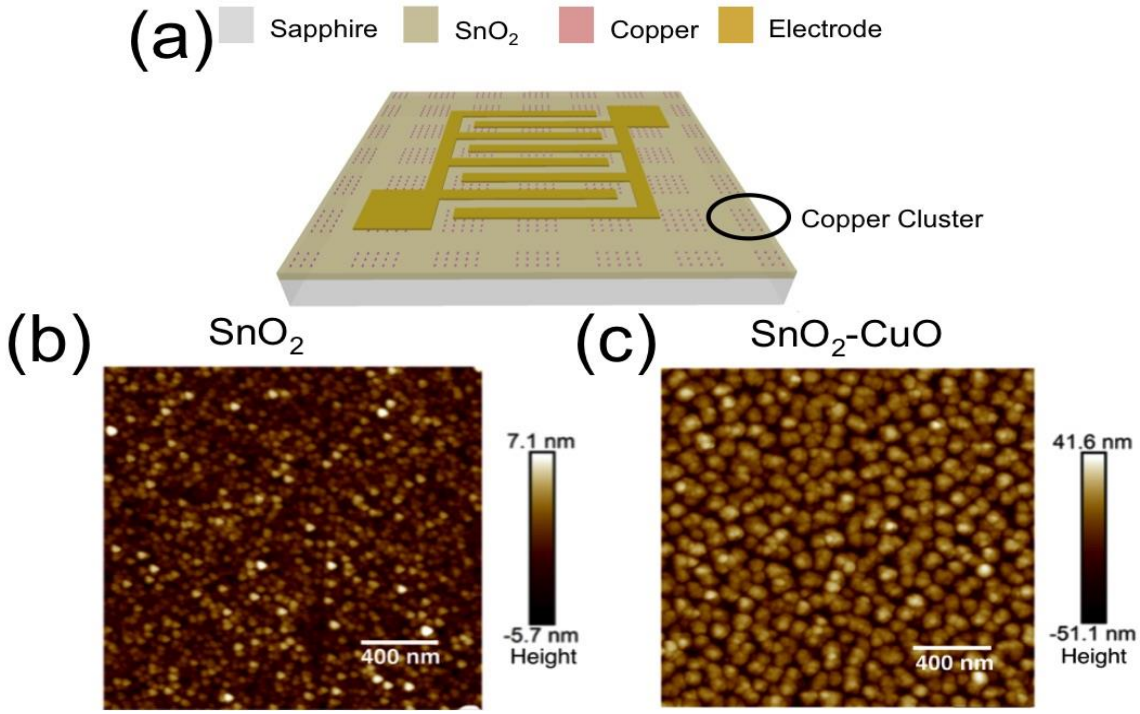

Figure. 16. (a) Schematic of a SnO_2-CuO nanocluster PD device including the top interdigitated electrodes. Dimensions are not to scale. (b) High-resolution AFM image of an as-deposited SnO_2 film. (c) High-resolution AFM image of a SnO_2 film with a top layer of CuO nanoclusters.

XPS measurements were used to confirm the chemical identity of the SnO_2-CuO films. XPS curve-fitting and analysis was performed using CasaXPS software. The binding energies of the spectra were calibrated to the hydrocarbon peak at 284.8 eV. High-resolution XPS spectra of the Sn 3d and Cu 2p regions of the SnO_2-CuO film are shown in Figures 17(a) and 17(b), respectively. As seen in Figure 17(a), the Sn 3d 5/2

peak appears at a binding energy of (487.1 ± 0.1)eV with a satellite peak characteristic of Sn 3d 3/2 at (495.5 ± 0.1) eV, which is consistent with previously reported XPS data for SnO_2.[19] The Cu 2p region of the spectrum shows a combination of Cu-related states that can be identified by referring to published reports.[20–22]

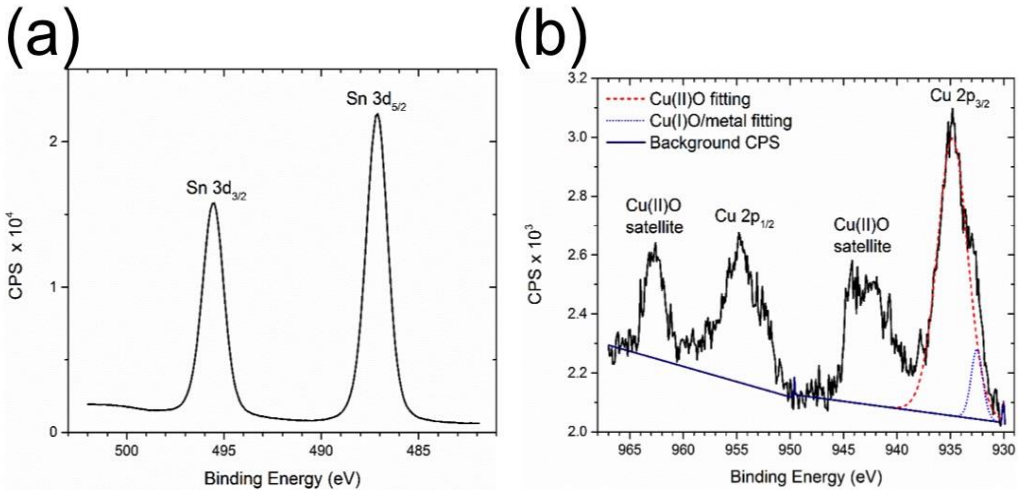

Figure. 17. High-resolution XPS spectra of (a) the Sn 3d and (b) the Cu 2p regions of a SnO_2-CuO film. CPS is counts per second.

Curve-fitting of the Cu 2p region peaks [Figure 17(b)] was used to estimate that 95 at.% of the Cu content of the sample is in the form of Cu(II)O and the other 5 at.% is in the form of Cu(I)O or Cu metal. From these measurements, we concluded that the deposited Cu NPs are substantially oxidized to form CuO during and after the deposition process.

The absorption spectra and absorption coefficients (α) of the SnO_2 and SnO_2-CuO films were measured using an Ocean Optics QE65000 spectrometer and a J. A. Woollam

M2000 ellipsometer, respectively. Optical absorbance spectra of the SnO_2 and SnO_2-CuO films are shown in Figure 13(b). A significant enhancement in the light absorption over the wavelength range of 250 nm to 475 nm is observed in the film decorated with CuO NPs compared to the bare SnO_2 film.

To verify the enhancement mechanism associated with the addition of the CuO NP clusters, FDTD simulations were used to calculate the optical properties of a 100 nm thick SnO_2 film with and without CuO nanoclusters on top. The simulated structure is shown in Figure 18(a). The CuO NPs were modeled as randomly distributed elliptic paraboloids. The particle shape, dimensions and average surface densities were derived from the analysis of the AFM images (Figure 16(c)). Refractive indices for the SnO_2 film were obtained from ellipsometry measurements, and reported values were used for the refractive indices for the CuO[23] and sapphire[24] substrate. A broadband (200 nm – 1000 nm) plane wave incident from the nanocluster side of the device was used as the excitation source for the simulations.

Figures 18(b) and 18(c) show the experimental and simulated absorption spectra for the SnO_2 films with and without CuO NP clusters. The simulated and measured spectra show qualitative agreement in the effect of the CuO NPs on the increase in absorbance across all wavelengths in the plotted range, the apparent red shift of the absorption onset, and the change in shape of the absorbance curve. Differences in quantitative agreement can be attributed to inhomogeneity in the NP size and density distributions, and uncertainty in the SnO_2 film thickness in the real devices. The simulated spatial absorption profiles for a

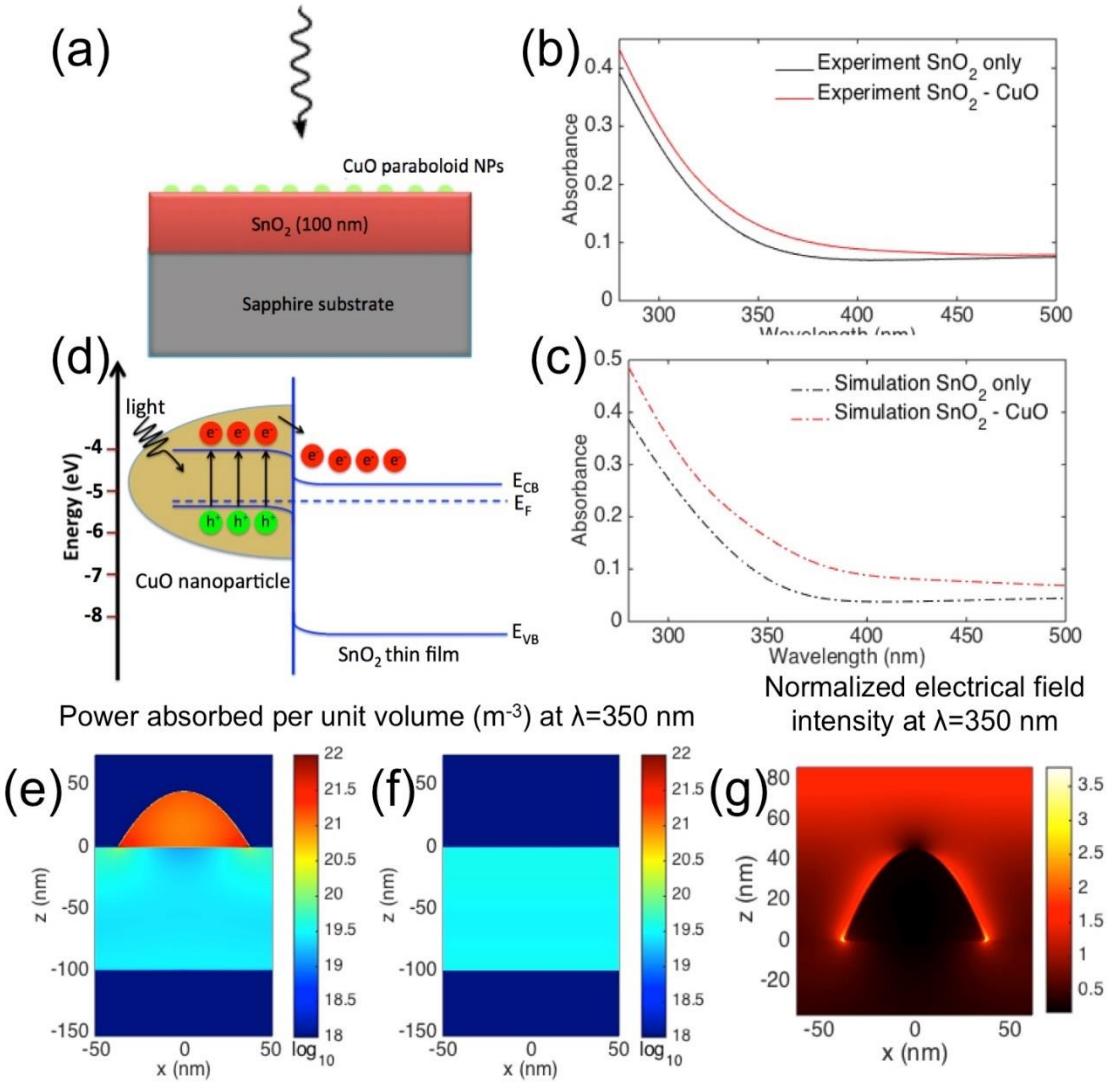

Figure. 18. (a) Diagram of the setup for the FDTD simulations. A SnO_2 film thickness of 100 nm was used for the simulations with and without CuO NPs. The CuO NP clusters were modeled as elliptic paraboloids with heights of 45 nm and diameters of 75 nm. The CuO NPs were randomly distributed on the SnO_2 film with an average surface density of 65 μm^{-2}. The size and average density values of the NPs were based on AFM measurements of the real devices. (b) Measured and (c) FDTD simulated absorption spectra of the SnO_2 and SnO_2-CuO films. (d) Schematic band diagram illustrating the hypothesized electron transfer process in the CuO-SnO_2 nanoheterojunctions under irradiation. (e) Spatial cross-section of simulated power absorbed per unit volume at λ = 350 nm in a single CuO NP on a SnO_2 film and (f) in a bare SnO_2 film. (g) Spatial cross-section of simulated normalized electrical field intensity at λ = 350 nm for a single CuO NP on a SnO_2 film.

single CuO NP on a SnO_2 film and a bare SnO_2 film at a wavelength of 350 nm are plotted in Figure 18(e) and Figure 18(f). The normalized electrical field intensity at a wavelength 350 nm is plotted in Figure 18(g). There is an enhancement of the local electrical field intensity around the NP and strong associated absorption within the NP. The enhanced absorption in the composite devices was attributed to this effect. The aim of this work was to use this increase in absorption without relying on an increase in SnO_2 film thickness to improve the responsivity of the SnO_2-based photodetectors. A schematic band diagram for the SnO_2/CuO *pn*-nanoheterojunctions is depicted in Figure 18(d) using energy levels reported for *p*-CuO[25] and *n*-SnO_2[26]. The nanoheterojunction structure takes advantage of the intense absorption in the CuO NPs to transfer a high density of photo-generated electrons from the *p*-CuO NPs to the *n*-SnO_2film, while the transfer of holes is hindered by the energy barrier at the junction. The smaller bandgap of CuO (1.35 eV[25]) results in increased absorption at the red edge of the UV spectrum, and the *pn*-heterojunction nature of the CuO/SnO_2 interface facilitates charge transfer upon illumination to increase the responsivity of the photodetector. Electrons injected into the conduction band of SnO_2 from the CuO increase the free majority carrier density in the photoconductive material, which could lead to a significant increase in photocurrent in the PD. Although the bandgap of CuO is small, the nanoscale structure of the CuO particles are predicted to allow the films to remain “visible-blind” due to poor in-coupling and low absorption in structures that are much smaller than the visible and infrared material photon absorption lengths.

Typical I-V characteristics of the SnO_2-only and CuO-SnO_2 devices measured in the dark and under UV-illumination are shown in Figure 19(a). The photocurrent generated in the PD with CuO NPs was almost double that of the SnO_2-only device under 290 nm wavelength illumination for all tested biases. The measured dark current for the CuO-SnO_2 PD was also larger than that of the SnO_2-only device, indicating that the conductivity of the CuO-SnO_2 composite film was larger than that of the SnO_2-only film.

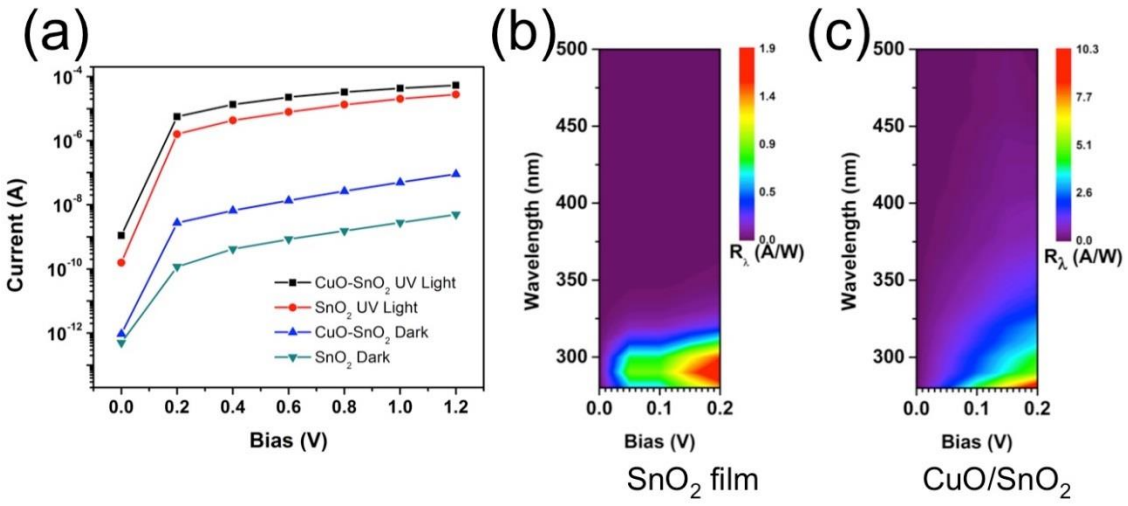

Figure. 19. (a) ON/OFF I-V curves for SnO_2-only and CuO/SnO_2 PDs under UV illumination at a wavelength of 290 nm. (b) Responsivity as a function of bias and wavelength for SnO_2 and (c) SnO_2-CuO thin film photodetecors.

To quantify the performance of the PDs, we used the photocurrent-to-dark current ratio, defined as:

$$S = \frac{I_{light} - I_{dark}}{I_{dark}} \quad (9)$$

where I_{light} is the current under UV illumination, and I_{dark} is the dark current at the same voltage, The CuO-SnO_2 PDs exhibited a PF of ~ 592 at 1.2 V under 290 nm

illumination. Responsivities of the SnO_2 and SnO_2-CuO PDs were measured at various bias voltages under a spectrally filtered light source. The measurements, calibrated using a standard NIST silicon photodiode, were associated with a total uncertainty of ± 5 % (fractional). In order to obtain stable and reliable data, the photocurrent at each wavelength was measured with a delay of 180 seconds with respect to the illumination. The need for stable photocurrent operation precluded higher resolution measurements of the PD response time.

The UV photocurrent response of the PDs was recorded over a voltage range of 0 V to 1.2 V at an illumination wavelength of 290 nm, as shown in Figure 19(a). In addition to light current enhancements, the dark current also increases after the SnO_2 surface is covered with the CuO NPs, despite the assumed formation of a depletion layer. This increase can be attributed to several potential mechanisms. The small amount of Cu(I)O or Cu metal visible in the XPS spectrum could lead to an increase in the dark current which could be ameliorated in future iterations by including a controlled oxidation step in the fabrication process. Additionally, the presence of defects close to the nanojunction interface could reduce carrier lifetimes, potentially act as dopants, and facilitate leakage paths, contributing to an increase in device dark current. Figures 19(b) and 19(c) illustrate the spectral responsivity of the SnO_2 devices with and without CuO NPs in the low bias regime. The SnO_2-only PDs reached a maximum responsivity of 1.9 A/W at 0.2 V bias under 290 nm illumination, while the devices with CuO NP clusters exhibited a responsivity of 10.3 A/W at 0.2 V bias under280 nm illumination. The incorporation of the CuO NPs resulted in a greater than 5-fold improvement of the

responsivity. Additionally, the SnO_2-only PD response had a sharp cutoff at around 320 nm in wavelength, whereas the SnO_2-CuO PDs displayed some response out to 340 nm in wavelength at low bias. The broadening of the spectral detection range can be attributed to the drastic enhancement of light absorption and charge transfer facilitated by the SnO_2-CuO nanoheterojunctions in the UVA spectral region. Although the responsivity of these devicesis lower than that of PDs based on one-dimensional structures[9,14], it is competitive with thin-film based UV PDs made from other traditional semiconductor materials.[27]Additionally,this method produces robust structures without complex fabrication processes that operate at low bias, making it suitable for practical applications.

3.2 CONCLUSION

In summary, we have demonstrated high responsivity visible-blind UV PDs based on sputtered SnO_2-CuO nanoheterojunction films. We investigated the properties of the films using AFM and XPS measurements, confirming that the sputtered Cu forms self-assembled nanoparticle clusters that are composed primarily of Cu(II)O after air exposure. The peak responsivity reached a value of 10.3 A/W at a low bias of 0.2 V in the CuO-SnO_2 devices, representing a five-fold increase over the highest responsivity achieved in devices without CuO NPs. The performance enhancement is attributed to the intense local absorption of the CuO NPs and the charge transfer facilitated by theCuO-SnO *pn* nanoheterojunction structures. This approach of utilizing CuO-based *pn* nanoheterojunctions to enhance the efficiency of visible-blind SnO_2 photodiodes

represents a viable path for building UV optoelectronic devices based on cost-effective materials.

CHAPTER FOUR: THE SOLUTION GROWTH OF ANTIMONY SELENIDE NANOSTRUCTURES ON FLEXIBLE SUBSTRATE FOR BROADBAND PHOTODETECTORS

As digital imaging devices gain in popularity, the quest for new infrared-sensitive materials that don't depend on epitaxial thin-film deposition techniques has intensified. The ability to deposit semiconducting films from solution has shown great potential for various electronic and optoelectronic applications and emerged as an attractive low-cost approach to fabricating high-quality semiconducting thin films.[41,96-101] One can simply employ "*soft*" non-vacuum processes such as spin-coating,[100,102-105] ink-jet printing,[98,106] and similar techniques to enable high-throughput device fabrication and realize new technologies particularly in the area of flexible optoelectronics.[104,107,108]

Research on solution-processed semiconductors has focused on both organic and inorganic systems.[96,98,99] However, molecular organic systems have several disadvantages including poor environmental, mechanical and thermal stability as well as poor electronic transport as compared to their inorganic counterparts. On the other hand, inorganic semiconductors can take advantage of covalently-bonded frameworks to achieve desirable electronic transport properties and band gaps.[109-111] There have been tremendous efforts to deposit inorganic films with excellent properties using chemical bath deposition,[112-115], spray pyrolysis,[116,117] and other solution-based methods.

Among various inorganic semiconductors, metal chalcogenides, particularly, group V-VI compounds have been widely studied for their opto-electrical[42,118] and thermoelectric properties[119,120] and successfully utilized in thin film transistors,[99,100] solar cells,[41,118,121]thermoelectric devices,[122,123] photodetectors (PDs),[124,125] and phase change memory[126] applications. These films have typically been prepared via sophisticated deposition techniques such as catalyst-assisted chemical vapor deposition,[127] sputtering,[128] thermal evaporation[118,129] and molecular beam epitaxy[130] that require energy-intensive, high vacuum deposition conditions not amenable to high-throughput mass production.

Although most metal chalcogenides are very difficult to dissolve in common solvents, recent developments in solution-based chemistry of chalcogenides have overcome this limitation, and homogeneous, high-quality semiconductor films derived from true molecular inks have been grown successfully.[131] Typically, an ink is made by dissolving stoichiometric amounts of elemental chalcogens with metal in hydrazine solutions.[100,132] Unfortunately, hydrazine is highly toxic and explosive, which limits the practicality of production. Some less hazardous and volatile solvents, such as mixtures of amine and thiols, have been used for solution deposition, but their application has been limited to bulk metal chalcogenide thin film growth from their respective compounds.[131,133]

Antimony selenide (Sb_2Se_3) has emerged from the group V-VI chalcogenides as an excellent candidate for optoelectronics due to its direct band gap of about 1.1 eV[41] in the NIR regime and p-type semiconductor behavior. One-dimensional (1D) Sb_2Se_3

nanostructures are of particular interest due to their high surface-to-volume ratio and tunable properties that can be used to enhance the performance of optoelectronic devices. Such NWs have been synthesized in the past using solution-based growth methods,[40,125,134] but Sb_2Se_3–based devices, (e.g., PDs) have been fabricated mostly on rigid substrates.[125]The complicated growth methods based on toxic solvents and limited performance to date have hindered Sb_2Se_3 from competing with traditional crystalline PD technologies.

This project showed a new method for template-free, facile, one-step solution-based and *in-situ* growth of Sb_2Se_3 nanowires (NWs) on flexible polyimide substrates. Our one-pot synthesis method is based on a molecular ink prepared by directly mixing elemental antimony and selenium into a solution of ethylenediamine (EDA) and 2-mercaptoethanol (ME). Chemical, structural and optical properties of the NWs obtained from this technique are characterized. Sb_2Se_3 PDs fabricated on flexible substrates exhibit excellent figures of merit, such as a broadband photoresponse spanning from the ultraviolet (UV) to near-infrared (NIR) range, fast temporal response and superior mechanical stability. Additionally, we demonstrate that the spectral response of our detectors should be tunable by adjusting the nanowire size. Results in this project indicate that molecular-ink-based flexible, scalable, and tunable systems have the potential to replace conventional broadband and NIR optoelectronic technology.

4.1 EXPERIMENTAL SECTION

***Growth of Sb_2Se_3 Nanostructures*:** In a typical synthesis, 2.5 mmol (304 mg) antimony (Alfa Aesar, 99.5+%) and 7.5 mmol (590 mg) selenium (Alfa Aesar, 99.999+%) were weighed in a 20 ml vial and transferred to a nitrogen filled globe box (MBraun, < 0.1 ppm O_2 and < 0.1 ppm H_2O). Then, 5.0 ml ethylenediamine (Alfa Aesar, 99+%) and 1.5 ml of 2-mercaptoethanol (Alfa Aesar, 98+%) were added to the vial. The solution was stirred for several days until complete dissolution of the constituent elements occurred, resulting in a dark orange color. To obtain nanograin-like morphology rather than nanowires, the selenium concentration was reduced to 4 mmol (316 mg), resulting in a final solution of light orange color.

Figure 20. Fabrication scheme for Sb_2Se_3 nanostructure formation on flexible substrates utilizing a molecular ink. The process begins with dissolution of elemental Sb and Se in ethylenediamine (EDA) and 2-mercaptoethanol (ME) to produce a molecular ink that is spin-cast onto a flexible substrate and annealed to form a flexible nanowire-based film.

***Thin Film Fabrication and Metallization*:** The obtained Sb_2Se_3 ink was spin-cast onto a polyimide film (Dupont, Kapton® HN) at 1500 rpm for 40s in a nitrogen glove box, and the deposited thin films were annealed at 350 °C for 5 mins inside the glove box.

Subsequently, the substrates were taken out from the glove box and stored in air. Interdigitated electrodes (IDEs) with metal contacts of Au/Ti/Au (20/90/20 nm) were evaporated at a rate of about (0.5 - 1) Å/s through a shadow mask using electron-beam evaporation. Both the width and the spacing between the adjacent electrodes (pitch) were fixed at 100 µm. The device area was about 16 mm^2, and four devices were patterned on each 15 mm by 15 mm polyimide substrate.

***Characterization*:** The microstructure and composition of the materials were examined using a JEOL JSM-7100 FLV variable vacuum field emission scanning electron microscope (FESEM) equipped with an Oxford Instruments 80 mm^2*X-Max* silicon-drift energy dispersive X-ray detector (EDXS SDD) and AZtec integrated microanalysis system. Scanning and transmission electron microcopy (S/TEM) imaging in various modes, selected-area electron diffraction (SAED), electron-energy loss (EEL) and EDXS spectroscopic analyses of the Sb_2Se_3 nanostructures were performed in a Schottky field-emission FEI Titan 80-300 analytical S/TEM with a point-to-point resolution of 0.19 nm and information limit below 0.1 nm equipped with S-TWIN objective lenses and operating at 300 kV accelerating voltage. For high spatial resolution nanoanalysis in the STEM mode using a 0.2 nm diameter probe, the instrument was equipped with a Fischione 3000 model high-angle annular dark-field (HAADF) detector, FEI BF- and ADF-STEM detectors, a Gatan Enfina electron spectrometer, and a 30 mm^2 EDAX Si/Li EDX detector with a 0.13 srad acceptance angle. To ensure optimal counting rates, the specimens were tilted at an angle of 15^o towards the EDX detector. Crystallinity of the deposited films was characterized using a Rigaku SmartLab X-ray diffraction (XRD)

system. An integrated HORIBA Jobin Yvon LabRAM 800HR bench-top system[135] was used for Raman spectroscopy using a 532 nm laser (Laser Quantum DPSS) with a spot size of ≈ 1 μm.

UV-VIS-NIR absorption spectroscopy (Lambda 950 Perkin Elmer) was used to determine optical band gaps, extracted by employing Tauc plots. Vacuum ultraviolet variable angle ellipsometry (VUV-VASE) measurements were also performed to determine the dielectric functions of the films from which the band gaps were extracted.

PD devices were characterized by current-voltage (I-V) and EQE measurements using a spectrally filtered light source, and the system was calibrated using a NIST-calibrated silicon photodiode. A total uncertainty of ± 5 % (fractional) is associated with the measured EQE under AM1.5 illumination. For transient response measurements, PD devices were illuminated using a Panasonic Aicure UJ30 system equipped with a 365 nm UV light emitting diode (LED), and currents were monitored with and without UV light using an Agilent B1500A semiconductor device parameter analyzer.

4.2 RESULTS AND DISCUSSION

Our deposition method for Sb_2Se_3 films is depicted in Figure 20 and involves the following steps: (i) dissolving elemental Sb with excess Se at a molar ratio of 1:3 in EDA and ME to produce the precursor solutions under magnetic stirring for several days in a nitrogen glove box; (ii) spin-casting the resulting dark orange molecular ink onto polyimide substrates and (iii) annealing the as-deposited films. The details can be found in the Experimental section.

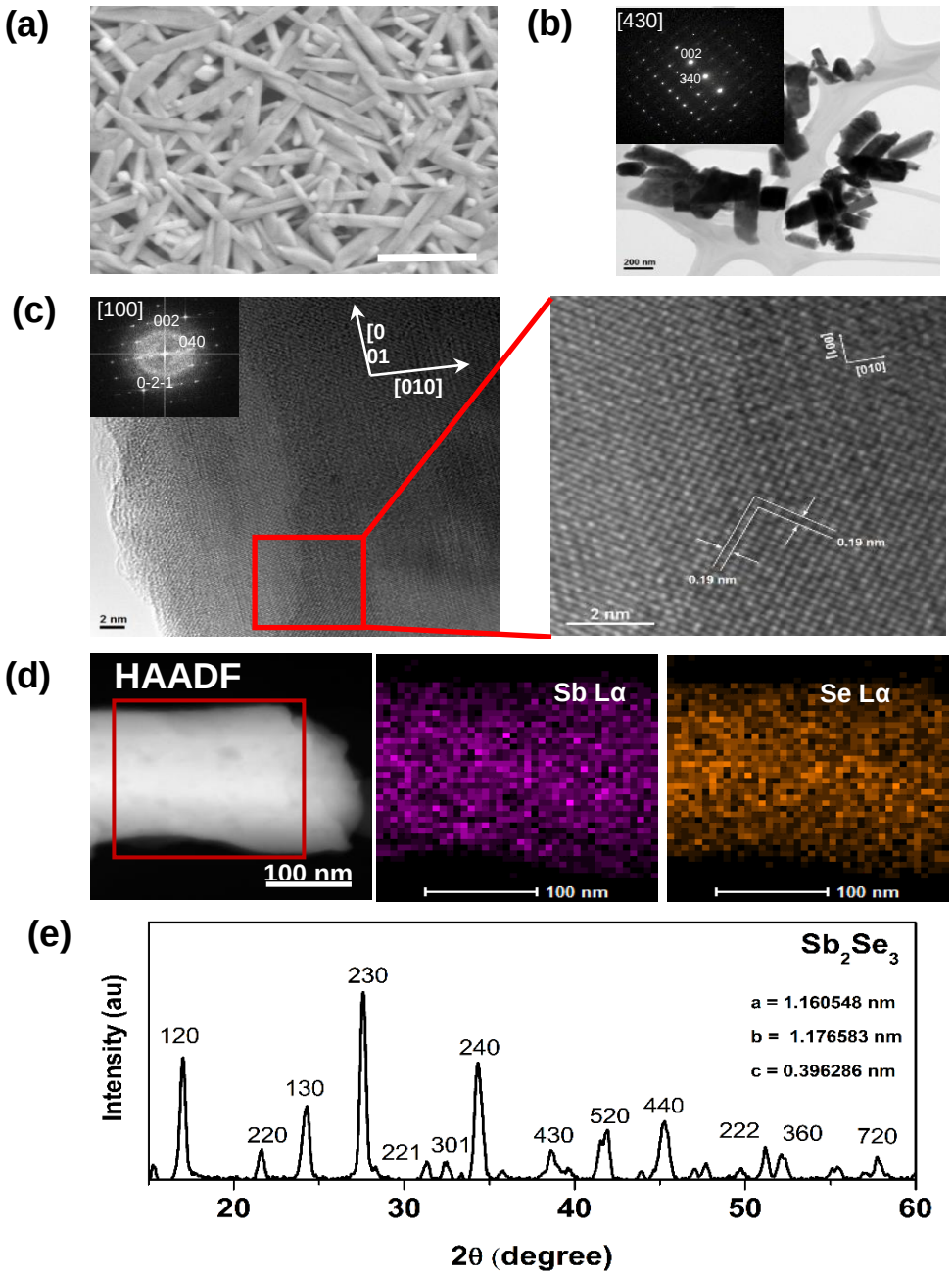

Figure 21. Analytical electron microscopy and XRD analysis of Sb_2Se_3 NWs: (a) High magnification FESEM image. The scale bar corresponds to 1 µm. (b) Bright-field (BF) TEM of Sb_2Se_3 NWs with a SAED pattern in the [430] orientation (inset), (c) HRTEM of a single crystalline orthorhombic NW growing along the <001> direction with the corresponding FFT pattern in the [100] orientation (upper left inset). The right inset shows an enlargement of the area marked by the red box on the left showing the (022) and (0-22) lattice fringes. (d) HAADF-STEM image of a Sb_2Se_3 NW and corresponding Sb Lα and Se Lα X-ray maps (right insets). (e) GIXRD pattern of the NW film and the calculated lattice constants.

4.2.1 Analytical Electron Microscopy of NWs

Field-emission scanning electron microscopy (FESEM) was used to image the Sb_2Se_3 nanostructures on flexible polyimides after thermal processing at 350 °C in the presence of excess Se, as shown in Figure 21. The FESEM image shows the formation of randomly oriented NWs having a small range of lengths and diameters. The processing temperature and selenium concentration are key fabrication parameters as they dictate the aspect ratio of the nanostructures which, in turn, affects the device optical properties. Formation of NWs from the as-deposited films takes place at around 200 °C in the presence of excess selenium; however, when the concentration of Se is lowered (to near the stoichiometric concentration), the films grow instead with a nanograin-like morphology. Compositional mapping by energy-dispersive X-ray spectroscopy (EDXS) shows the distribution of Sb and Se elements in the film, and one can clearly see the individual nanostructures in the elemental maps. The EDXS spectrum exhibits strong Sb and Se peaks, and there is no discernable sulfur present in the film.

Transmission electron microscopy (TEM) measurements revealed rod-like morphology of 0.1 µm to 1.2 µm long Sb_2Se_3 NWs with diameters ranging from 100 nm to 300 nm (Figure 21b). The corresponding selected-area diffraction (SAED) pattern (Figure 21b, inset) and phase-contrast high-resolution TEM (HRTEM) images (Figure 21c) indicate that the Sb_2Se_3 nanostructures are single orthorhombic crystals growing along the <001> direction of the *Pbnm* space group. The SAED pattern of an individual NW indexed as the [430] zone shows a 002 point reflection with 0.20 nm lattice spacing (d_{002} = 0.19810 nm) and a 340 point reflection with 0.23 nm lattice spacing (d_{340} = 0.23431 nm). More

detailed analysis of SAED patterns revealed additional splitting of {34*l*} reflections due to twinning of NWs along the growth direction likely caused by close-packed growth conditions. The latter was supported by examination of corresponding TEM micrographs. The HRTEM image in Figure 16c (left) reveals several families of interplanar lattice fringes, including large 0.58 nm (020) spacing (d_{020} = 0.5885 nm) parallel to the growth direction, and the inset shows a Fast Fourier Transform (FFT) pattern implying [100] orientation for the Sb_2Se_3 NW sample area indicated by the red box. The enlarged HRTEM fragment (Figure 16c, right) shows orthogonal 0.19 nm (022) and (0-22) lattice fringes observed in the vicinity of a partially amorphized NW surface.

For more accurate evaluation of the nanoscale elemental composition and the spatial uniformities of the Sb and Se elemental distributions, EDXS-FESEM compositional analyses were corroborated with high spatial resolution EDXS and electron energy-loss spectroscopy (EELS). Analyses of randomly selected NWs from the same sample were performed using a 0.2 nm diameter electron probe in scanning transmission electron microscopy (STEM) mode at 300 kV accelerating voltage. Elemental mapping results revealed that Sb and Se were uniformly distributed throughout the analyzed NWs (Figure 16d), and elemental line profiles confirmed the same. X-ray spectra acquired during line profiling have been further quantified using a Cliff–Lorimer thin film ratio technique with calculated k-factors for the Sb Kα and the Se Kα peaks, and absorption (mass-thickness) correction as described elsewhere.[136] Similarly, EELS spectra taken in randomly selected spots on the same sample have been quantified using a thin film ratio technique with 200 eV energy windows for both Sb $M_{4,5}$- and Se $L_{2,3}$-edges and

corresponding calculated Hartree-Slater ionization cross-sections.[137] Quantification results demonstrate that the Sb/Se atomic ratio in the NWs is close to stoichiometric with excellent agreement between the employed analytical techniques.

Table 3. Quantitative EDXS and EELS analyses of Sb_2Se_3 NWs

Utilized Techniques	Accelerating voltage, kV	Sb/Se atomic ratio, $\pm 2\sigma$ at the 95% confidence limit
EDXS-STEM Cliff-Lorimer thin film ratio method with calculated k-factors for the Sb Kα and the Se Kα peaks and absorption (mass-thickness) correction	300	0.65 ± 0.09
EELS thin film ratio method with 200 eV integration windows for the Sb $M_{4,5}$- and the Se $L_{2,3}$-edges	300	0.65 ± 0.04

4.2.2 X-ray Diffraction and Optical Properties

Crystal structure of the Sb_2Se_3 NW films was confirmed by using grazing incidence X-Ray diffraction (GIXRD), as shown in Figure 21e. All of the diffraction peaks can be indexed to the orthorhombic phase of Sb_2Se_3 (JCPDS Card No. 72-1184)with a space group of *Pbnm* (62).All of the major planes were indexed, and no secondary phases were detected. Using retrieval analysis, the lattice constants are calculated as: a = (1.160584 ± 0.0004) nm, b = (1.176583 ± 0.0005) nm and c = (0.396286 ± 0.0002) nm, very close to the ideal bulk values for Sb_2Se_3 (a = 1.162 nm, b = 1.177 nm, c = 0.3962 nm) and consistent with previously reported data.[42,138,139]

In order to determine the transition type and the optical band gap, a transmission spectrum of the Sb_2Se_3 NW thin films was recorded using UV-Vis absorption spectroscopy. The band gap was estimated by extrapolating the linear region of the Tauc

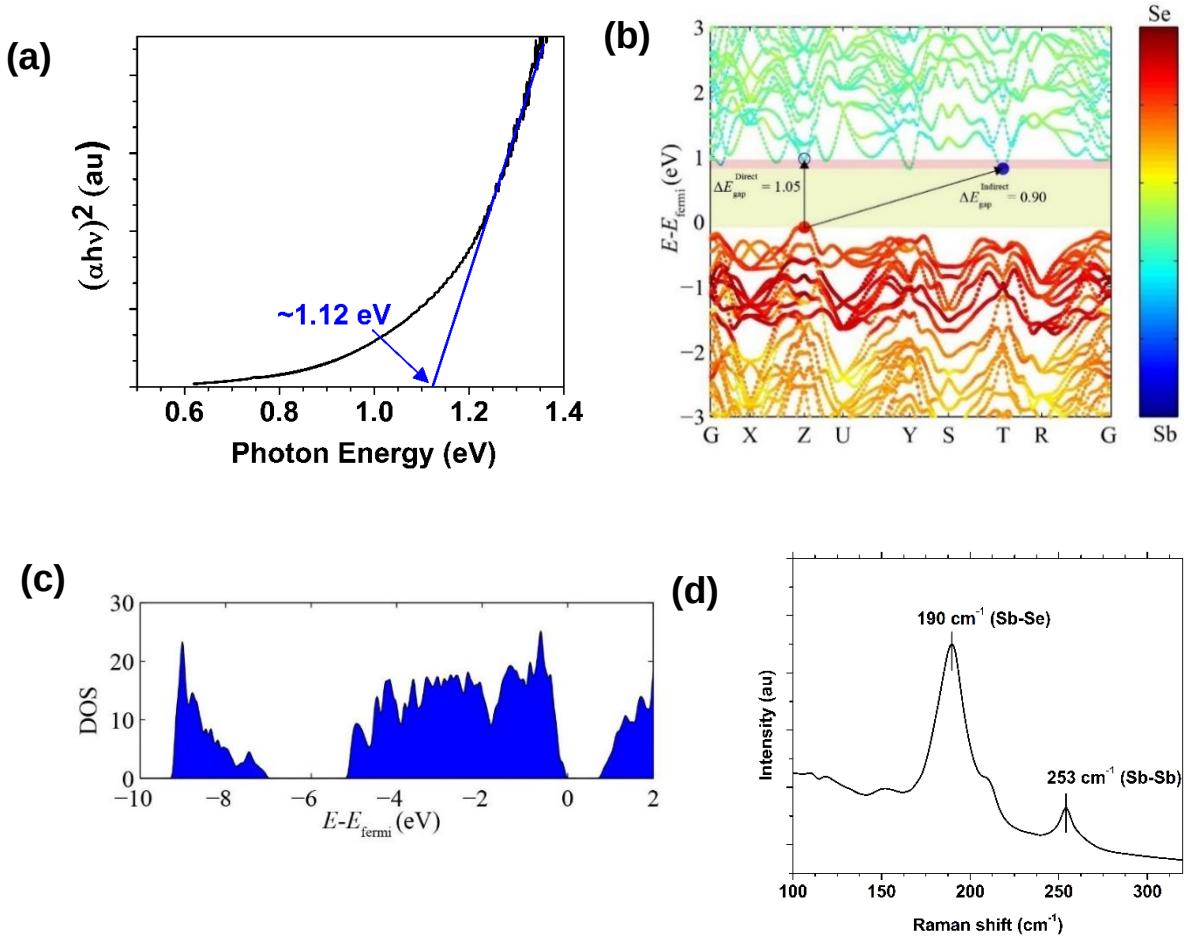

Figure 22.Optical properties of Sb_2Se_3: (a) Tauc plot used to estimate the band gap (~1.12 eV) from a linear interpolation. (b) Electronic band structure of bulk Sb_2Se_3 computed using DFT simulations. Sb_2Se_3 has an indirect band gap, $\Delta E_{gap}^{Indirect}$, of 0.90 eV and a direct band gap, ΔE_{gap}^{Direct}, of 1.05 eV. The valence band maxima and conduction band minima are marked with red and blue circles, respectively. The symbol sizes and colors denote the weights of the Sb or Se contributions to the bands. The valence band maximum is set to zero energy. (c) The calculated DOS vs. E − E_{fermi} in eV. (d) Raman spectrum showing the heteropolar Sb−Se and non-polar Sb−Sb vibrations.

plots of $(\alpha h\nu)^2$ versus $h\nu$ to $h\nu = 0$ (Figure 22), where α is the absorption coefficient and $h\nu$ is the photon energy. A direct transition type with a value of ~1.12 eV was confirmed, quite close to previously reported values,[41] as well as those measured by ellipsometry.The electronic band structure of bulk Sb_2Se_3 were also computed using density functional theory and found good agreement with the measured band gap of the deposited NWs. The calculated minimum gap of 0.90 eV for $Sb_2Se_3$was found to be indirect, and the direct gap was 1.05 eV,a difference of 0.15 eV from the indirect gap, making the direct and indirect transitions almost degenerate, as previously reported[42,138,139] (Figure 22b). Furthermore, the band structure of Sb_2Se_3 exhibits several transitions between the valence band and the conduction band with comparable energy to the fundamental indirect-gap energy,suggesting that Sb_2Se_3 can be considered a direct gap semiconductor for all practical applications. The states at the valence band edge are predominantly associated with Se p-orbitals and those at the conduction band edge are dominated by the Sb p-orbitals. The density of states (DOS) for bulk Sb_2Se_3 shown in Figure 22c agrees well with earlier work.[118] The close agreement in the band gap of bulk Sb_2Se_3 and solution-deposited Sb_2Se_3 NWs indicates surface and quantum confinement effects play little role in the electronic structure of the NWs. In addition, Raman spectroscopy performed on Sb_2Se_3 NWs revealed two Raman peaks centered at (190 ± 0.3) cm^{-1} and (253 ± 0.3) cm^{-1} which represent the hetero-polar Sb−Se and non-polar Sb−Sb vibrations[42](Figure 22d).

4.2.3. Flexible Photodetectors: Figures of Merits

After establishing the crystal structure and optical properties of the molecular-ink-based

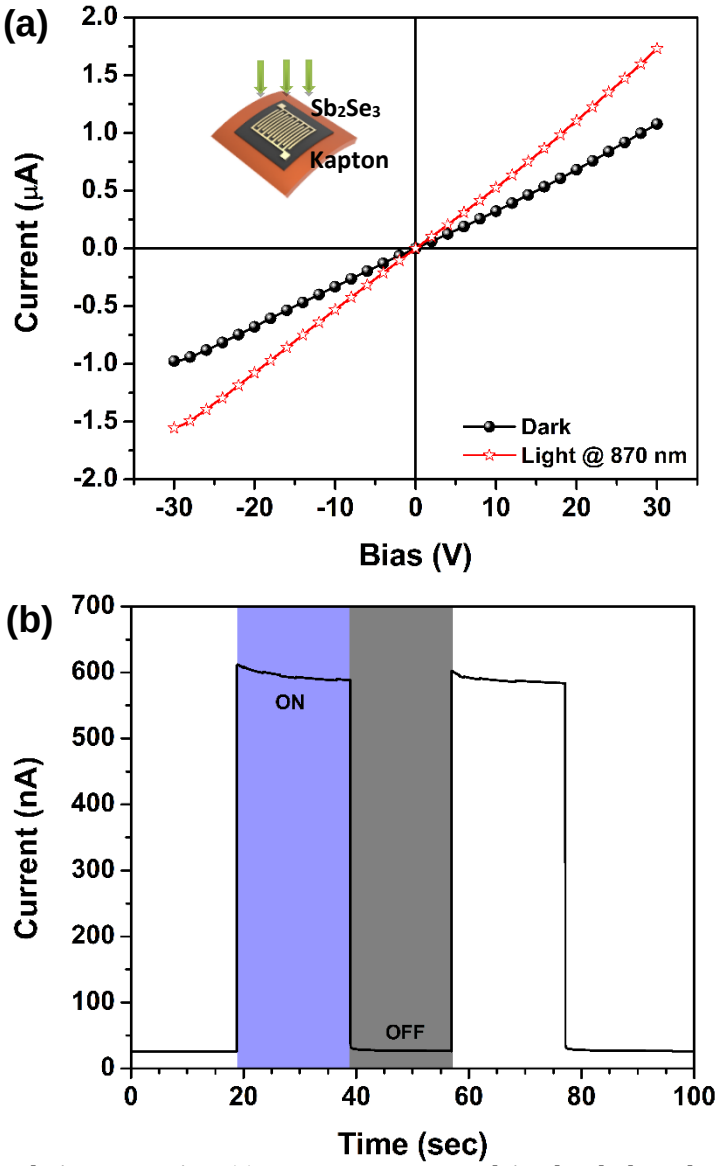

Figure 23. Photoconductive device properties: (a) I-V curves measured in the dark and under 870 nm illumination with a light intensity of 6.4 μW. The inset shows a schematic of the fabricated PD with interdigitated electrodes. (b) Temporal photocurrent response under 365 nm pulsed light (~ 30 mW/cm^2) with a period of 20 s at an applied bias of 10 V.

Sb_2Se_3 NWs, we fabricated flexible photoconductive photodetectors by depositing interdigitated Au/Ti/Au electrodes via electron beam evaporation on the NW-polyimide substrates (inset of Figure 23a). Figure 23a shows a current-voltage (I-V) characteristic curve for an Sb_2Se_3 NW PD measured in the dark and under 870 nm illumination. At an applied bias ranging from -30 V to 30 V with a very low illumination intensity of ~ 6.4 μW, the change in slope of the I-V curve indicates a strong photoresponse, and the linear I-V curve evinces the Ohmic nature of the contact between the metal electrodes and NWs.

The temporal response of the PD under pulsed 365 nm illumination (30 mW/cm^2, 20 s pulse width) and 10 V bias is presented in Figure 17b. The PD demonstrates photocurrent reproducibility and stability with two distinct states: a "low" current in the dark and a "high" current under illumination with an on/off ratio of ≈ 22. The characteristic rise time (τ_r) for the photocurrent to increase from 10% to 90% of its maximum value is (24 ± 2) ms, and the decay time (τ_f) for the photocurrent to decrease from 90% to 10% of the peak value is (9 ± 2) ms. This temporal response is significantly faster than previous Sb_2Se_3-based photodetector demonstrations.[125,134]

Device photoresponse is generally governed by complex processes such as carrier generation, trapping, and recombination. Due to the nanostructured nature of the PD active layer, abundant grain boundaries (or junction barriers) are expected to be present in the NW film. This type of defect is generally associated with the formation of deep traps leading to slow temporal response. Instead, the NW film measured here exhibits fast

decay and recovery times. This can potentially be attributed to the high quality crystalline nature of the materials, which leads to efficient optical absorption and photo-carrier generation under illumination. The increased carrier density reduces the junction barrier height between the adjacent NWs, and such light-induced barrier height modulation could lead to the fast response time. Additionally, the large surface-to-volume ratio of the NWs is likely associated with a high density of surface-associated dangling bonds/defects. Thus, when the light is turned off, the carriers can recombine quickly, resulting in short decay times. The spectral response of the PD was also obtained by scaling the measured photocurrent to that of a calibrated Si photodetector. Given nominally identical illumination conditions under applied bias, this measurement can be used to extract the external quantum efficiency (EQE) of the device. Figure 24a (top) is a contour plot of the device EQE, which increases monotonically with the applied bias. It can be seen that the applied bias influences the on/off ratio of the PDs, which is related to the bias dependence of the exciton dissociation and the background current. The EQE at 30 V reaches a maximum of ≈ 35% in the NIR (at 1.43 eV) and ≈ 51% in the UV (at 4.13 eV); however, it remains lower in the visible regime. In order to investigate the source of the partial visible transparency present in the EQE spectra, we ran a series of finite-difference time-domain (FDTD) optical simulations of single nanowires and nanowire arrays. The nanowires in the arrays were randomly oriented and modeled as cylinders with a random distribution of diameters ranging from 100 to 300 nm and lengths ranging from 100 to 1200 nm, based on the SEM measurements of the as-grown samples. Their refractive indices were determined from ellipsometry measurements, and absorption and reflection

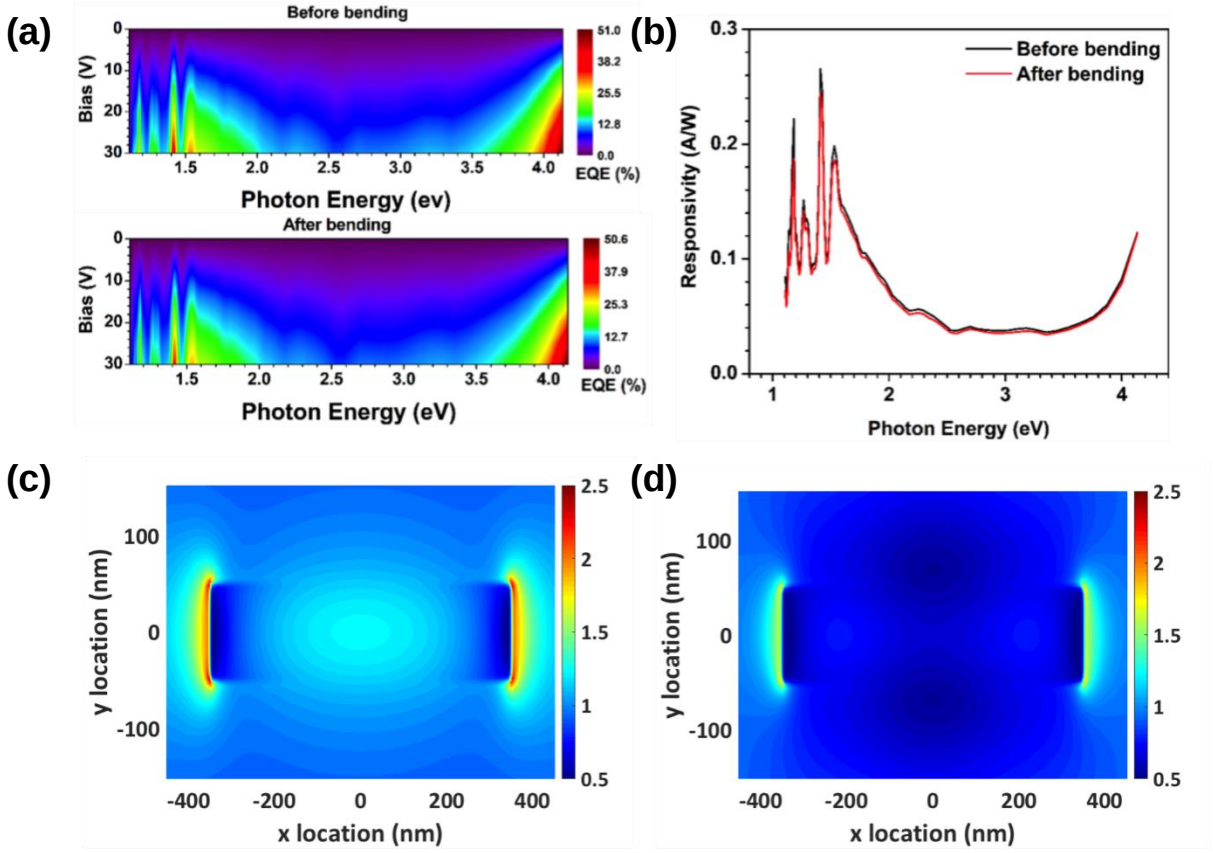

Figure 24. Figures of merit of the PDs: (a) EQE data as a function of applied bias: as-made devices (before bending: top) and after 40 bending cycles (after bending: bottom) over a radius of curvature of 1 cm. (b) Representative spectral responsivity of the same device at an applied bias of 30 V. The mechanical robustness of the devices is evident even after 40 bending cycles. (c)-(d) Calculated FDTD normalized electric field intensity for an average-sized single Sb_2Se_3 nanowire at the plane normal to the incident illumination (s-polarized source) at (c) λ= 1100 nm and (d) λ= 650 nm. The presence of a waveguide mode in (c) vs. the absence of a confined mode within the NW in (d) demonstrates a possible explanation for the enhanced NIR performance seen in (a) and (b).

as well as spatial electric field data were obtained for nanowire arrays and single nanowires. Transfer Matrix Method[42]was also used to calculate absorption and reflection for a device with a planarSb_2Se_3 film of comparable total thickness as a control. The FDTD absorption results qualitatively reproduce the observed dip in the visible region of

the EQE spectra, while the planar device absorption has less of a spectral discrepancy across the same range. The single nanowire results give a potential explanation for this phenomenon: in the visible region, the most common size of nanowire does not support a waveguide mode; however, in the NIR, the nanowire supports a strong mode, leading to enhanced in-coupling and waveguiding in the nanowire array. Nanowire spatial electric field profiles are plotted in Figure 18c and 18d for 1100 nm and 650 nm illumination, respectively.

These results imply that the spectral responsivity of the photodetectors could be tuned by changing the size of the nanowires in the array. The nanowire size is controlled by relative precursor concentration during growth and post-annealing conditions. This tuning knob could be used to enable enhanced broadband performance of the molecular-ink based photodetectors. Additionally, controlling the nanowire size would allow for the realization of spectrally-selective detection by enhancing or suppressing performance in specific spectral bands.

Mechanical stability is critical for practical applications of flexible optoelectronics. We measured the device photocurrent after 40 bending cycles over a radius of curvature of ≈10 mm. As shown in Figure 18b, there is no significant change in the EQE after many bending cycles, demonstrating the robustness of these PDs.

The responsivity (R_λ), another critical measure of PD performance, has also been calculated using the relationship:

$$R_\lambda = \frac{I_{light}}{P_0} \quad (10)$$

where I_{light} is the device photocurrent under UV illumination, and P_0 is the light intensity. The calculated responsivities of the devices at 30 V bias are shown in Figure 24b before and after bending. The maximum responsivity reaches ≈ 0.27 A/W at 880 nm and experiences only a slight decrease to ≈ 0.25 A/W after 40 bending cycles, comparable with other broadband PD technologies.

The figures of merit for these molecular-ink-based PDs could be further improved by optimizing the processing conditions and tuning the gap between the two IDEs to optimize the metallized area. Optically, tuning the nanowire size could target waveguiding and enhanced performance in the visible regime. One could also employ alternative light trapping and optical enhancement schemes such as integration of nanoscale plasmonic structures to improve in-coupling and benefit from local field enhancements.[42] Exploring these approaches is beyond the scope of this paper.

4.3 CONCLUSION

A facile, scalable, template-free route was developed to grow Sb_2Se_3 nanostructures directly on flexible substrates. Our molecular ink was prepared from elemental antimony and selenium dissolved in amine/thiol solvents and deposited at room temperature, employing a chemical method that should be extendable to other technologies. Compositional analysis and structural characterization of the resulting nanowires depict chemically pure, high-quality single-crystalline nanostructures with near stoichiometric composition. The fabricated PDs exhibit fast response and excellent figures of merit.

Manipulating the nanowire size is an additional tuning knob that could be used to enhance the broadband performance and build spectrally selective optoelectronics. The negligible change in photoresponse after multiple bending cycles is evidence of excellent mechanical stability which makes the new molecular inks a promising platform for low-cost, flexible and portable broadband photon detection, photoelectronic switches and other optoelectronic devices.

CHAPTER FIVE: ONE-STEP SOLUTION PROCESSING OF Sb_2S_3 NANO-RODS FOR HIGH-PERFORMANCE PHOTOCONDUCTORS

A large-scale, cost-effective and high-quality growth of antimony sulphide is vital in realizing its potential towards energy applications such as photoconductors, solid-state batteries, thermoelectrics and solar cells. In this paper we present a simple, low-cost and catalyst free one-step solution processing of one-dimensional Sb_2S_3 nanostructures on polyimide substrates and demonstrate its application as a photoconductor in the UV and visible regime. Using-field emission scanning electron microscopy, grazing incidence X-Ray diffraction, raman spectra and transmission electron microscopy measurements we show that the Sb_2S_3 films exhibit high quality crystallinity, uniform morphology and near-stoichiometric composition. Further, using tauc plot we find that the films have a direct bandgap of ~1.67 eV, closely matching with band gap predicted from HSE06 density-functional simulations. Metal-semiconductor-metal photoconductors fabricated using these films show a clear photo response in both UV as well as visible wavelength. These devices show UV on/off ratio as high as 160 under the light intensity of 30 mW/cm^2 and a small rise time of 44 ms and fall time of 28 ms.

5.1 EXPERIMENTAL METHODS

***Preparation of Sb_2S_3 Precursor Solution*:** In a typical synthesis, 2.5 mmol (304 mg) antimony (Alfa Aesar, 99.5+%) and 7.5 mmol (241 mg) sulfur (Alfa Aesar, 99.999+%)

were transferred to a nitrogen filled globe box (MBraun, < 0.1 ppm O_2 and < 0.1 ppm H_2O) along with a glass vial. Constantly stirring with a magnetic bar at 60° C, the mixture dissolved completely in 5.0 mL of ethylenediamine (Alfa Aesar, 99+%) and 1.5 ml of 2-mercaptoethanol (Alfa Aesar, 98+%). The final solution turned yellow in color (Figure 25a).

***Thin Film and Device Fabrication*:** The synthesized Sb_2S_3precursor was spin coated on a polyimide substrate with a speed of 1500 rpm for 40s in the glove box. Then the spin-coated thin films were annealed at 300 °C for 5 minutes on a hot plate inside the glove box. Au/Ti/Au (20/80/20 nm) metal contacts were deposited through a shadow mask to make interdigitated structure electrodes using electron-beam evaporator. Width of each metal finger and the distance between two consecutive fingers are 100 µm and the total area of each device is ~16mm^2.

***Film and Device Characterization*:** Rigaku SmartLab X-ray diffraction (XRD) system was used to characterize the crystallinity and lattice constant of the film. Lambda 950 Perkin Elmer UV-VIS-NIR absorption spectroscopy was used to measure absorbance spectrum of the film from which optical band gap could be determined using tauc's formula. An integrated HORIBA Jobin Yvon's LabRAM 800HR bench-top system[135] equipped with a 532 nm laser (Laser Quantum DPSS) and spot sizes of ≈ 1 µmwas used for Raman spectroscopy.

Photoconductor devices were characterized for current-voltage (I-V) characteristic in dark and under AM1.5 illumination to measure the photoresponse of the device in visible

wavelength (550 nm). Panasonic Aicure UJ30 system equipped with 365 nm UV light emitting diode (LED) along with Agilent B1500A semiconductor device parameter

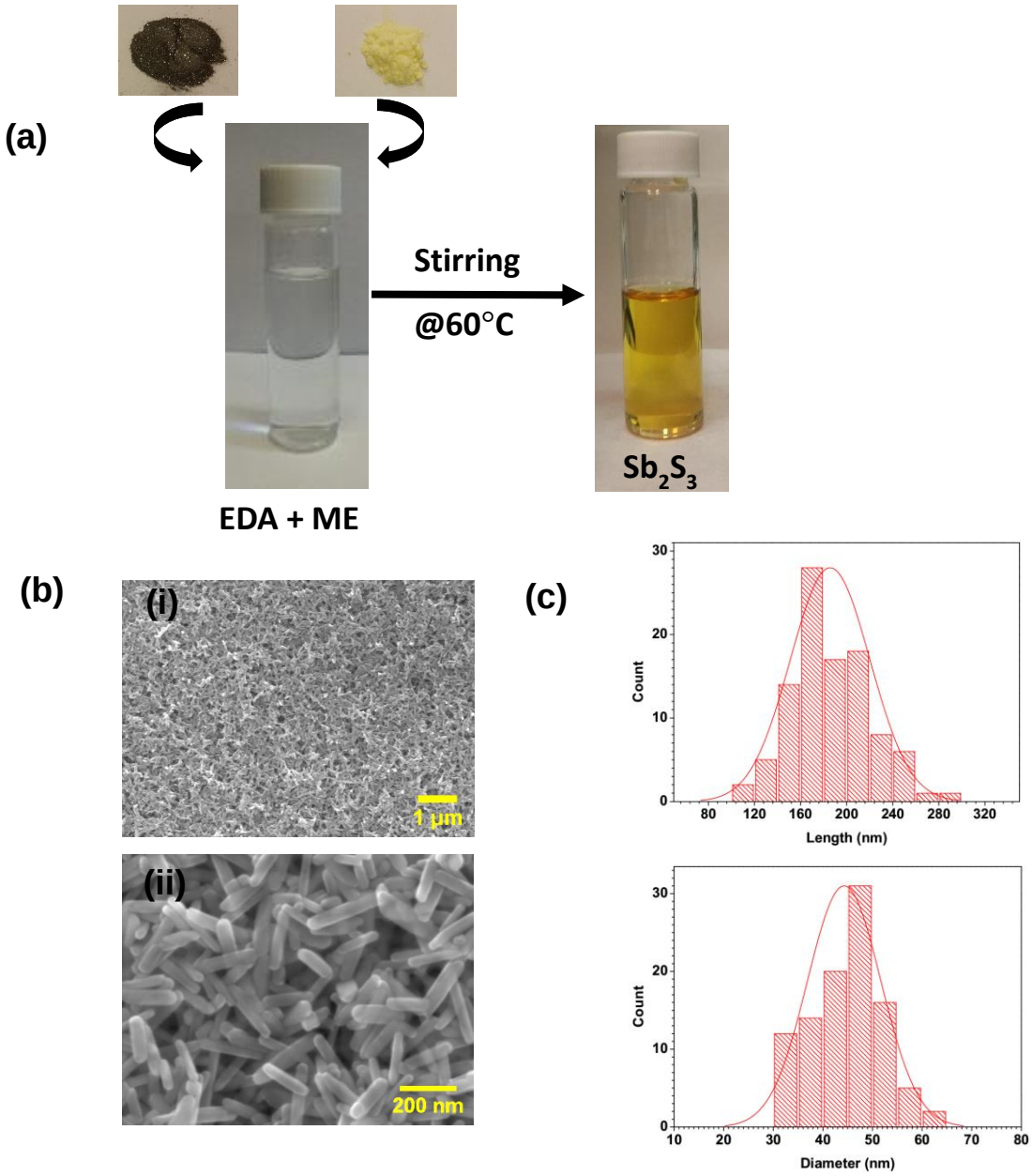

Figure 25. (a) Preparation of molecular ink for Sb_2S_3 and NR thin film on polyamide; (b) FESEM image of NR film as well as (c) size distribution for length and diameter of nano-rod

analyzer was used to illuminate the fabricated photoconductor and measure the transient response (rise time, fall time and UV on/off ratio) of the device. X-ray photoelectron spectroscopy (XPS) measurements confirmed the chemical composition of the Sb_2S_3 films. XPS curve-fitting and analysis was performed using CasaXPS software.

5.2 RESULTS AND DISCUSSION

Sb_2S_3 films we obtained on a polyimide substrate using the synthesis method illustrated in Figure 25a. A Sb_2S_3 molecular ink was prepared by dissolving 1:3 molar ratio of elemental Sb and Sin ethylinediamine (EDA) and 2-Mercaptoethanol (ME) at a temperature of 60° C by constant stirring with a magnetic bar for several hours. Spin coating this ink on a polyimide substrate followed by an annealing at 300° Celsius for 5

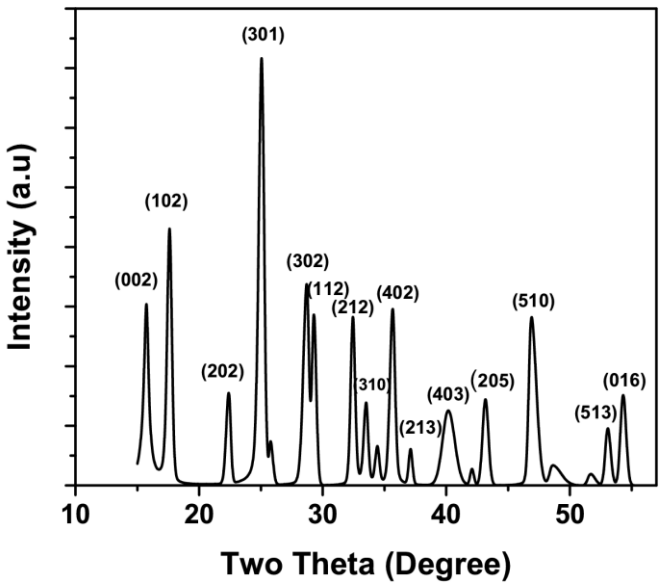

FIG. 26. XRD analysis of Sb_2S_3 NR

minutes give a film of randomly oriented Sb_2S_3 nanorods (NR) (Figure 25b). More details pertaining to the synthesis technique can be found in the experimental section. A field-emission scanning electron microscopy (FESEM) image of the Sb_2S_3 NR film,

shown in Figure 25(b), establishes that the Sb_2S_3 crystallizes as a film of randomly scattered 1 dimensional NR structures. Moreover, the absence of large scale features or undulations in the film suggests a uniform coverage of the NR over > 1μm regions. To estimate the size distribution of the NR we measured the length and diameter of 100 nanorods selected randomly from different sections of the film. Figure 25(c)shows a histogram of the lengths and diameters of these nanorods fit to a normal distribution to extract average nanorod dimensions and their variation across the film. Results show an average nanostructure length and diameter of 184±30 nm and 44±6 nm, respectively. Figure 26 shows the grazing incidence X-Ray diffraction (GIXD) pattern of the Sb_2S_3NR films and all the diffraction peaks match with the standard files for mineral stibnite (JCPDS Card No. 78-1347) indicating that the NR film has an orthorhombic phase of $Sb_2S_3$with space group of *Pcmn*(62). All the major planes were indexed in the figure using Scherer's formula, the lattice constants are calculated as: a = (11.2333 ± 0.003709) Å, b = (3.83984 ± 0.001459) Å and c = (11.31141 ± 0.004979) Å which were almost similar to the bulk value of the Sb_2S_3 stibnite (a = 11.2217Å, b = 3.8351Å, c = 11.3018Å).

Raman spectrum of the NR film is shown in figure 27(a).Raman peaks centered at 281±0.5 cm^{-1}, 309±0.4cm^{-1} and 236±0.5 cm^{-1} can be attributed to stibnite[140,141,142]. And a very weak vibrational peak located at 263±0.4 cm^{-1} can be ascribed to Sb_2O_4[143,144]. The

presence of a nominal oxygen content in the NR film is also confirmed by the (EDXS) electron dispersive X-ray spectroscopy.

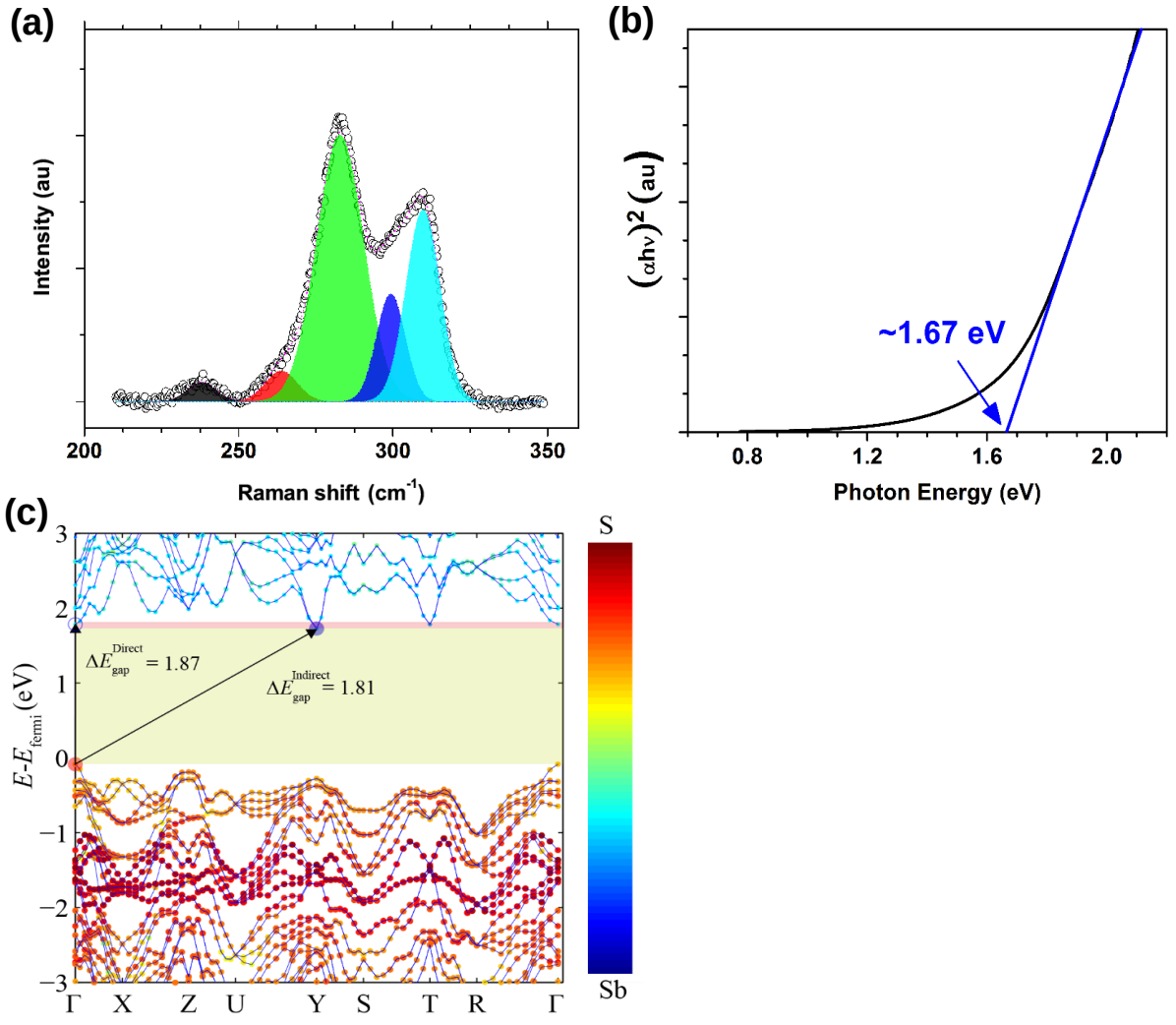

Figure 27. (a) Raman spectroscopy (b) Direct bandgap of Sb_2S_3 from tauc's plot. (c) Electronic band structure of bulk Sb_2S_3 computed using DFT simulations with a HSE06 functional. Sb_2S_3 has an indirect band gap, $\Delta E_{gap}^{Indirect}$ of 1.81 eV and a direct band gap, ΔE_{gap}^{Direct} of 1.87 eV. The valence band maxima and conduction band minima are marked with red and blue circles, respectively. The symbol sizes and colors denote the weights of the Sb or S atoms to the bands. The valence band maximum is set to zero.

For energy conversion applications it is essential to determine the band gap of the NR film. The absorbance spectrum was measured in the transmission mode using UV-Vis spectroscopy so that the bandgap of the material can be derived using the famous tauc formula[145]. Figure 27(b)shows the bandgap of the Sb_2S_3NR film extracted from the tauc plot. A direct bandgap of synthesized Sb_2S_3NR film was estimated as ~1.67±0.02 eV by extrapolating the linear region of the Tauc plot $(\alpha h\nu)^2$ versus $h\nu$ to $h\nu = 0$, where α is the absorption coefficient and $h\nu$ is the photon energy. The bandgap value is consistent with the previously reported data[146,147,148]. Nanostructured materials are well-known to display electronic properties which are different from their bulk counterparts. It is likely that the NR film of Sb_2S_3 shows an electronic structure that is similar the stibnite because of short Debye length of the nanorods, much shorter than the nanorod dimensions. To verify this, electronic band structure of the band gap of $Sb_2S_3$was simulated using density functional theory.

Figure 27(c)shows the atom-projected electronic band structure of bulk Sb_2S_3 computed *via* density functional theory using a hybrid functional, HSE06. The atom-projected band structure reveals that the states at the top of the valence band are predominantly associated with S *p*-orbitals and those at the bottom of the conduction bands are dominated by the Sb *p*-orbitals. It is well known that the standard DFT with a generalized gradient approximation (GGA) suffers with the bandgap underestimation problem which can be circumvented by using the HSE06 functional. The band structure of Sb_2S_3 obtained from GGA can be found in the supplementary section. It is clear that the band structure remains qualitatively unaffected between the two functionals, however,

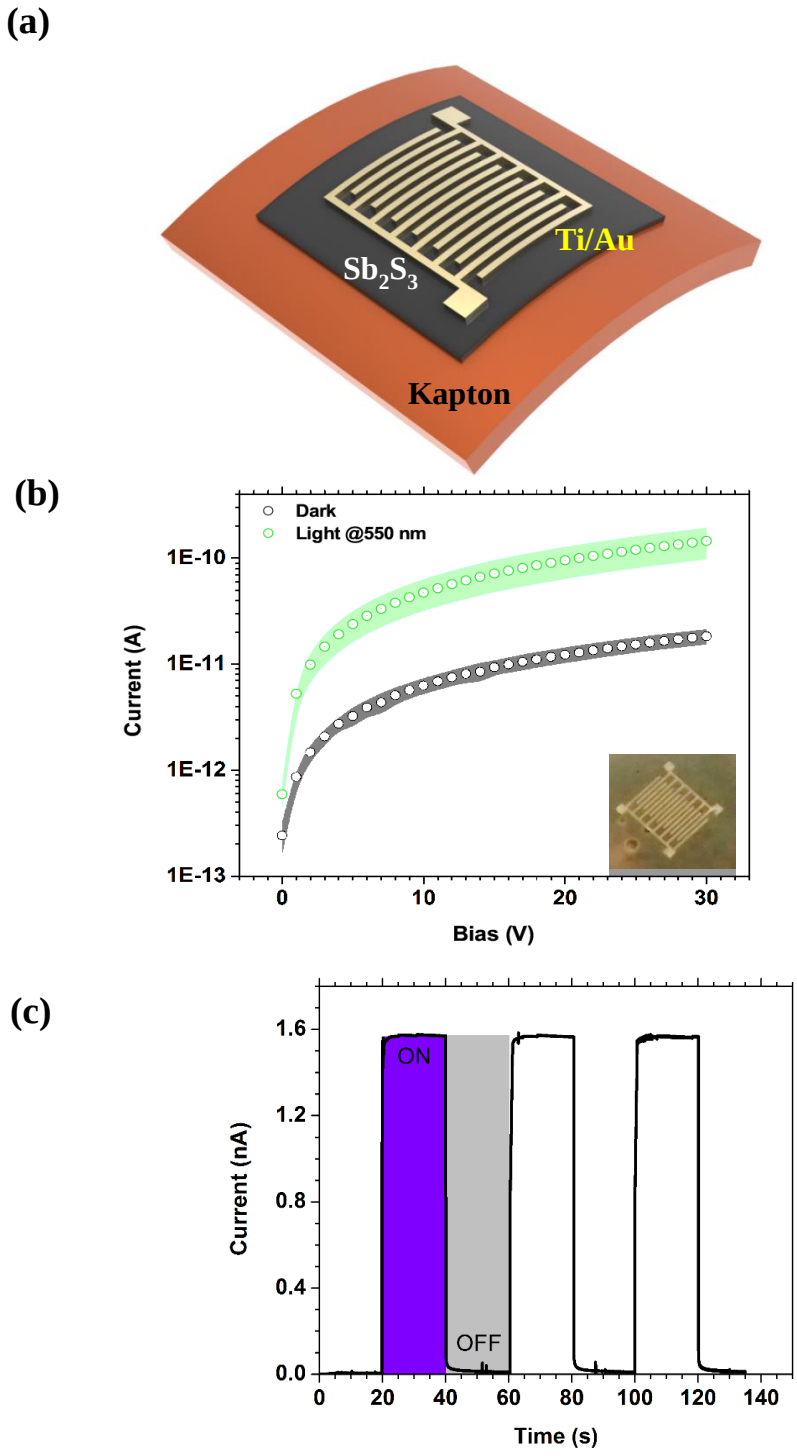

Figure 28. (a) Device schematic, (b) Current-voltage characteristic curve under dark and 550 nm illumination (power ~11.5 uW). Light current to dark current ratio is ~8 under this ultra-low intensity light. (c) Transient response of the photoconductor. UV on/off ratio is calculated as ~160, rise time and fall is 44 ms and 28 ms respectively.

as expected, the energies of direct and indirect band transition are larger for the HSE06 functional. The calculated HSE06 minimum gap of Sb_2S_3 is found to be indirect, of 1.81 eV, and the direct gap is 1.87 eV, merely 0.06 eV different from the indirect gap, making the direct and indirect transitions almost degenerate (Figure 27(c)). The close agreement in the band gap and band transition of the bulk Sb_2S_3 and Sb_2S_3 NR films indicates a weak surface and size-effect towards the electronic structure of the NR film.

As the band gap of the fabricated films is suitable for photoconduction in the UV and visible range we fabricated metal-semiconductor-metal (MSM) photoconductors from the Sb_2S_3 NR film on the polyimide substrate. Figure 28a shows a schematic of one such device. Interdigitated Au/Ti/Au (20/80/20 nm) metal pattern was deposited by shadow mask using an e-beam evaporator, with 4 IDE patterned devices in each sample. Details of the device dimensions can be found in the experimental section. Figure 28bshows current-voltage (I-V) characteristic curve for Sb_2S_3 NR Photoconductor measured in the dark and under 550 nm light illumination. Three devices fabricated from the same sample were measured and the mean value of current under each applied bias along with the standard deviation from device to device is plotted. The inset shows the fabricated Photoconductor on Sb_2S_3 NR film. At an applied bias ranged from 0 V to 30 V with a very low light intensity of ~ 11.57 μW, the photoresponse from the device is clearly visible. At 30 V of applied bias, the dark current is 18±3 pA and the current under 550 nm illumination is 145±48 pA. Photocurrent (550 nm) to dark current ratio is ~8 with a very small light intensity of 11.57 μW. We find that the conductivity of the film is very

low under dark (in the range of instrument noise) and it generates electron-hole pair upon illumination even with a very ultra-low intensity light.

Figure 28c exhibits the temporal response of the NR photoconductor. 365 nm light pulse was applied for 20 second with an applied bias of 10 V and the characteristic rise time, t_r(time needed to rise from 10% to 90% of the maximum photocurrent), of the photoconductor was measured as 44±1 ms. When the UV light is turned off after 20 seconds, the device took 28±0.5 ms to fall from 90% to 10% of the peak photocurrent. UV on/off ratio was measured as ~160 with an input light intensity of 30 mW/cm^2. We confirmed the reproducibility and stability of the temporal response applying multiple pulses and conducting several scans. We observed photoresponse both in UV and visible wavelength as expected from the obtained bandgap of Sb_2S_3 (1.67 eV ≈ 750 nm).

5.3 CONCLUSION

In summary a simple, cost-effective and high-quality one-step solution based synthesis of Sb_2S_3 nanorod films was presented. Using Sb and S as precursors a molecular ink of Sb_2S_3 in EDA and ME was developed, which is then spun coated on polyimide substrates resulting in highly crystalline and near composition Sb_2S_3 nanorod film of thickness XYZ nm. Using SEM, GIXRD, EDS, raman spectroscopy and TEM measurements, the structure, composition and dimensions of the NR in the Sb_2S_3 film were established. Absorption spectroscopy results show that the film has a direct band gap of 1.67 eV, which is confirmed by HSE06 density functional theory simulations. Photoconducting devices of the film show a photoresponse in UV and visible range with UV on/off ratio as

high as 160 under the light intensity of 30 mW/cm^2 and a small rise time of 44 ms and fall time of 28 ms. The solution based synthesis shown in this work can help in the realization of printable, large scale, cost effect and efficient photoconductors. Next-generation energy conversion materials engineered via solution based promise low-cost and high-quality devices.

CHAPTER SIX: EFFECT OF CONTACT PAD GEOMETRY AND ORIENTATION OF BONDING WIRE ON COUPLING OF SUB-THz RADIATION FOR IMAGING

The terahertz part of the electromagnetic spectrum, which is considered in the frequency range of 100 GHz to 10 THz, has emerged as an important area of research for many potential applications in recent years. Much of this interest has been inspired by the promise of valuable new applications for terahertz imaging and sensing[54]. The field of terahertz (THz) spectroscopy, imaging, and technology has grown dramatically over the past fifteen years.[1] THz sources and detectors,[149-154] THz imaging systems[54] have improved a lot and have found several industrial applications including explosive and concealed weapon detection,[155-157] pharmaceutical quality control,[158] biology/medicine,[159] and nondestructive evaluation/quality control.[160]

The terahertz (THz) region of the electromagnetic spectrum lies in the gap between microwaves and infrared. This so-called 'terahertz gap' has historically been termed as the deficiency of convenient and inexpensive sources, detectors, and systems for terahertz waves. For frequencies below about 100 GHz (corresponding to a free-space wavelength of λ = 3 mm), electronic components are available to purchase from commercial suppliers, and millimetre-wave imaging systems have become available. Thermal sources

are used for generating radiation of frequency above 10 THz ($\lambda = 30$ μm). The frequency spectrum in between these two frequencies are much less well explored[54].

The channel of a field effect transistor (FET) can act as a resonator for plasma waves. The plasma frequency of 2-dimensional electron gas (2DEG) channel depends on its dimensions and for gate lengths of a micron and sub-micron (nanometer) size can reach the terahertz (THz) range. Dyakonov and Shur[161] predicted that a steady current flow in a FET channel becomes unstable when plasma waves are generated. The same authors have shown later on that the nonlinear properties of the 2D plasma in the transistor channel can be used for detection and mixing of THz radiation[50,47].

The main known facts about THz detection by FETs so far are: i) the resonant detection observed at cryogenic temperatures is due to plasma waves related rectification and ii) at room temperature, the plasma wave oscillations are overdamped but the rectification mechanism is still efficient and enables a broadband THz detection and imaging.

Spatial variation dependence of sub-THz photoreponse was shown in some wroks[49,53,162], but they associated the sign change of spatial images with the position of the devices with respect to incoming radiation. Not much work has been reported to show the effect of orientation of bonding wire on coupling of THz radiation and thus on spatial variation image patterns in a multi-channel FET. In this work, the effect of contact pad geometry and bonding wire orientation on coupling of sub-THz radiation in multi-channel FET has been shown along with the mechanism of coupling.

6.1 EXPERIMENTAL SETUP

300 GHz light source was used and the incoming radiation was chopped with a modulation frequency of 200 Hz and then the THz beam was focused on the device using some parabolic mirrors and polarizer. Two grid polarizers were employed to control polarization of incident radiation. The radiation-induced change of the voltage at the drain of the device, was recovered by a SR830 lock-in amplifier. The device was

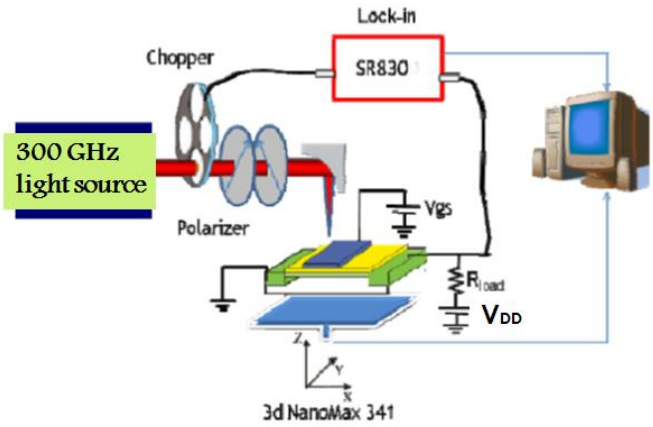

Figure 29. THz photoresponse measurement setup at Rensselaer Polytechnic Institute[162]

mounted on a 3D Nanomax 341 nanopositioning stage from ThorLabs, which was movable in x,y and z directions by a computer program with a very high resolution to record spatial variation images. External batteries were used to bias the drain and gate of FET. This measurement was done at Rennselaer Polytechnic Institute (RPI).

6.2 RESULTS AND DISCUSSION

Figure 30 shows the wire bonded Commercial Qorvo-triquint FET having 3 shorted drain pads and 2 shorted gate pads. Each drain and gate pad was bonded with one wire and large source pad with 3 wires in different positions to observe how the coupling mechanism at 300 GHz radiation changes if different pads are connected.

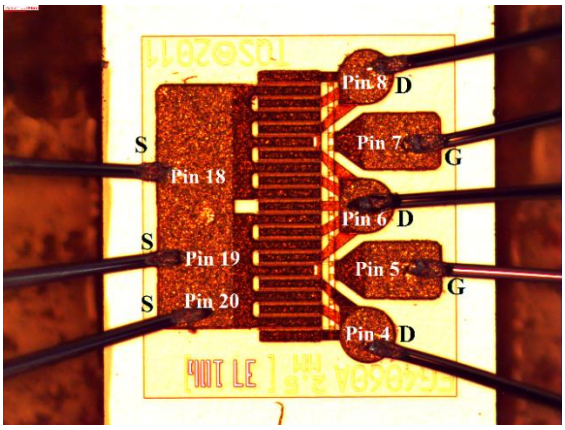

Figure. 30. Image of the GaN/AlGaN FET

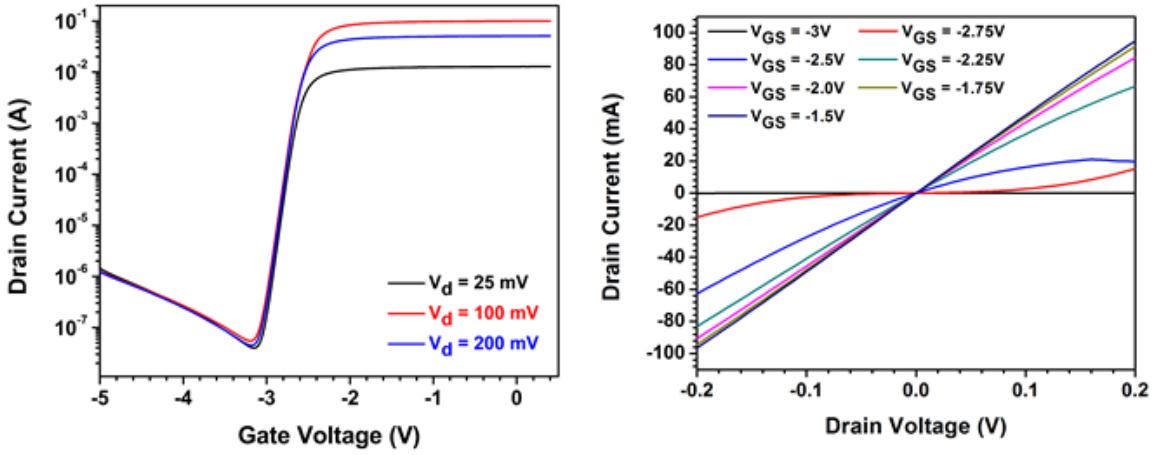

Figure. 31. (a)I_d-V_g curve of the FET and (b) I_d-V_d curves of the FET

The device has interdigitated source and drain pads with 20 parallel channels and small gate fingers of 1 µm. DC characterization of the device was done by Agilent B1500A semiconductor parameter analyzer. Figure 31 shows the I_d-V_g curves and I_d-V_d curves of the FET. Threshold voltage is around ~-3V for the device and the on-off ratio is 10^6-10^7 orders for different applied drain voltages. Subthreshold swing is calculated as 90 mV/decade. From figure 31(b), it is quite clear that, current increases very quickly and reached to compliance limit value as the channel resistance is very low (~100Ω in linear region) and it cannot reach saturation region for most of the gate voltages, but hits the compliance limit set by the instrument.

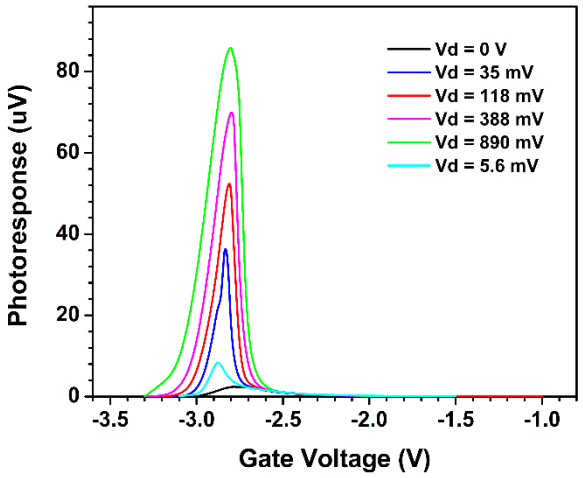

Figure. 32. Terahertz photoresponse vs V_{GS} for different V_{DS}

Figure 32 shows the terahertz photoresponse vs gate voltage curves for different applied drain voltages. Gate bias dependent photoresponse curve shows that, photoresponse reaches to maximum value near V_{th} and slightly shifts to right with higher drain voltages

at room temperature, which is consistent with reported data[163,164]. At zero drain bias, the induced photovoltage was 2.8 μV. When the drain bias is applied, the asymmetry between the source and drain is further increased which assists more coupling of radiation. As a result, induced photoresponse increases with increased drain bias and the maximum of 84 μV was induced at V_{ds} =890 mV. For Imaging of THz radiation, V_{DS} = 200 mV was applied, and the peak photoresponse at this drain bias appears at V_{GS} =-2.75V. Figure 33 shows the Noise Equivalent power (NEP) (left black scale) and Responsivity (right red scale) graphs against the gate voltage. A maximum responsivity of 2.5mV/W is obtained near V_{GS} =-2.75V. NEP reaches the minima at -2.5V and tends to rise after that and at -2.75V, the value of NEP is $5\times10^{-6}W/\sqrt{Hz}$. The minimum value of NEP for this device is $7\times10^{-7}W/\sqrt{Hz}$.

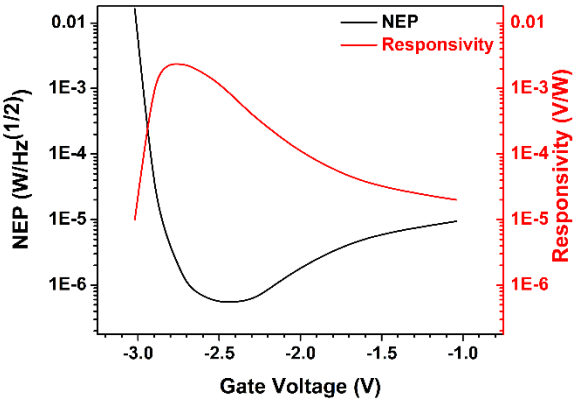

Figure. 33. NEP (left scale) and Responsivity (right) vs V_{GS} of detector

Low Frequency Noise measurement

Low frequency noise measurements were done to see the effect of applied V_{GS} on the noise for imaging and also to understand the degree of channel resistance fluctuation present in the device. Figure 34 shows the drain current noise spectrum for different gate

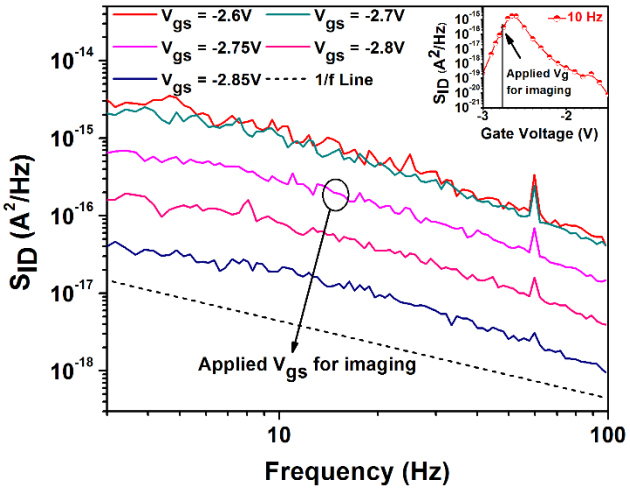

Figure. 34. Drain current noise spectral density vs Frequency for different V_{GS}

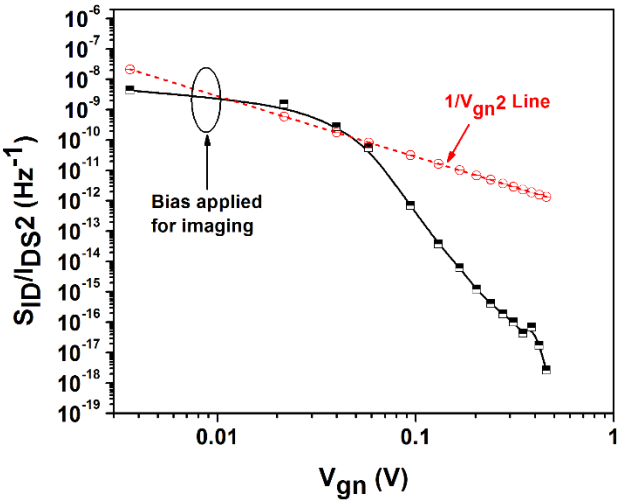

Figure. 35. Normalized drain current NSD vs Vgn at 10 Hz

voltages. S_{ID} for all applied V_{GS} follow 1/f dependence and the noise level is gradually decreasing with the gate voltage moving towards pinch off voltage. The lowest noise level in A^2/Hz is obtained at V_{GS} =-2.85V. The noise level is in the order of 10^{-15} A^2/Hz or smaller for the V_{GS} =-2.75V, which is quite low. Inset shows, how the noise spectral density changes with gate voltage. Figure 35 shows the normalized drain current NSD (noise spectral density) vs V_{gn} at 10 Hz. V_{gn} is normalized threshold voltage, which is defined as $V_{gn} = (V_{GS}-V_t)/V_t$. This graph also shows the $1/V_{gn}^2$ trend line in red color. If S_{ID}/I_{DS}^2 follows the $1/V_{gn}^2$ line, then the noise arising from channel resistance fluctuation is dominant than access resistance (ungated part and contact resistance added together), but if channel resistance is smaller or comparable to the access resistance, then S_{ID}/I_{DS}^2 graph falls much quicker than $1/V_{gn}^2$ line at higher V_{gn}[165]. In this device, the fall of the drain current NSD line is much quicker than $1/V_{gn}^2$ showing that, access resistance is comparable or higher than channel resistance.

Imaging

The spatial variation depenedent photoresponse images were taken by raster scanning from -2mm to +2mm in both and x and y directions with a step of 0.07mm and wait time of 2 seconds in between consecutive steps. For all the scans, the bias applied was V_{GS} =-2.75V and V_{DS} =200 mV. Figure 36 shows the spatial variation of induced photoresponse for different connection configurations. Source, drain and gate pads with respective pin numbers are shown above all the spatial variation images to understand better the effect of geometry of contact pad and bonding wire. Pins 4,6 and 8 are connected to 3 drain pads; Pins 5 and 7 are connected to 2 gate pads and pins 18,19 and 20 are connected to

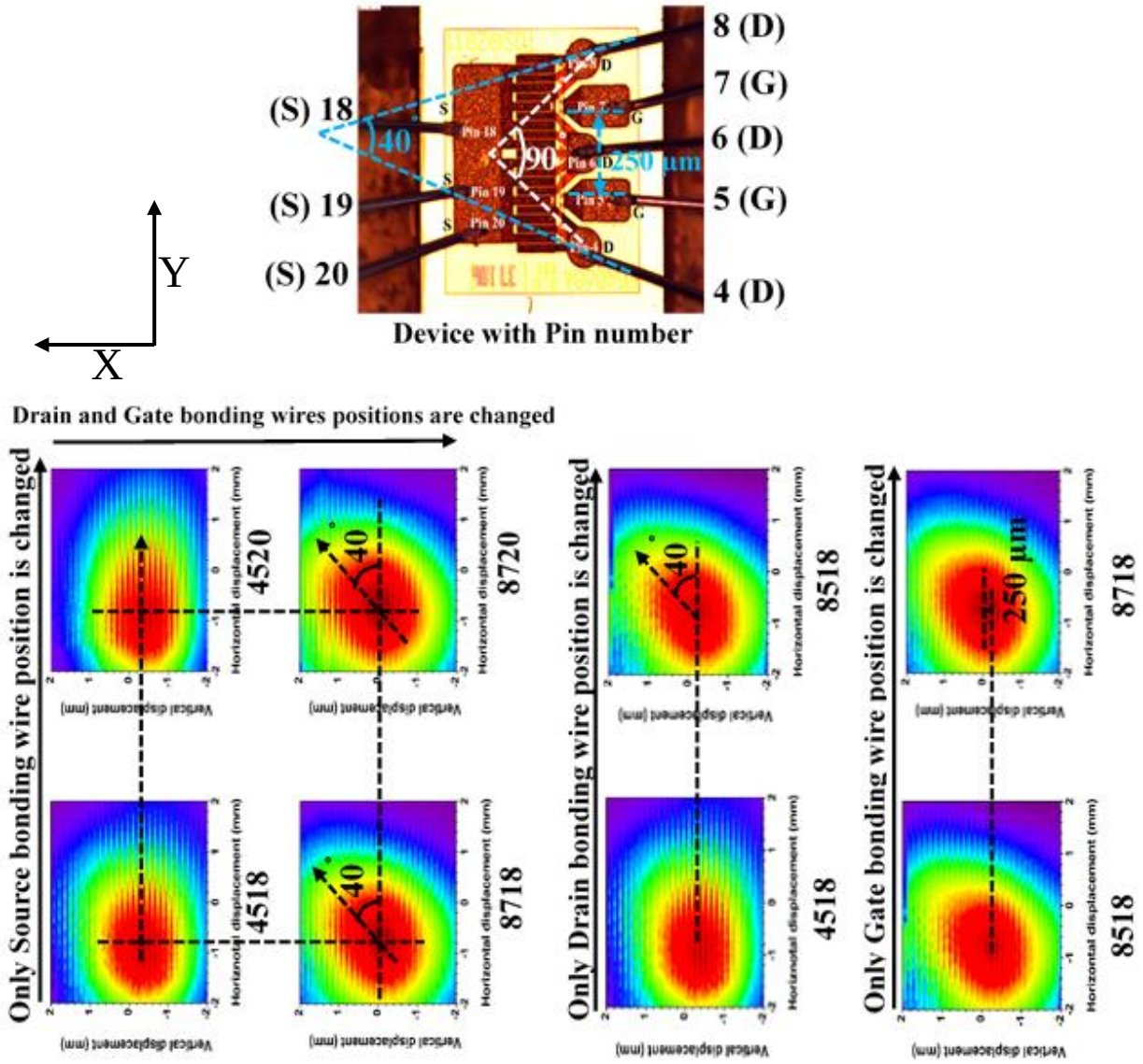

Figure 36. Effect of metal pad geometry and bonding wire on the spatial variation image at 300 GHz

single large source pad with the aluminium bonding wires. Three drain pads and 2 gate pads are electrically shorted separately. Pin configuration is mentioned for each image. In the notation, number of drain pad is mentioned first, which is followed by numbers of

gate pad and source pad, respectively. When drain and gate are connected to 4 and 5 respectively, but source pad is changed from 18 to 20, there is no effect on the image. Both the center position and the direction of image remains unchanged. The effect of source pad on coupling of radiation was further confirmed by another set of images, i.e; from 8718 to 8720 and same effect was found. But when positions of both drain and gate pads are changed together, from 4518 to 8718 and 4520 to 8720, then the images are tilted to 40° in both the cases and also the center point of focused beam is slightly shifted to the positive x direction.

To understand the effect of drain coupling and gate coupling on the spatial variation of photoresponse, another 2 combinations of images were plotted in right side of figure 36. When pin-configuration is changed from 4518 to 8518, i.e.; only drain pad's position is changed from pin-4 to pin-8, then the image is tilted to 40° without changing the image center. The angle between contact pad 4 and 8 is $\sim 90^{\circ}$, but the image is tilted to 40°(the gate pad is unchanged at pin-5). As the radiation is of 300 GHz and the wavelength is 1 mm , some part of drain pad bonding wire acts as antenna (quarter wave is 250 μm) and contributes in the coupling as the drain pad diameter is merely about 100 μm. Now, interestingly the angle between these two bonding wires is 40° (figure 36). So, the orientation of drain bonding wire with respect to gate pad is basically defining the angle of image.

The effect of gate pad coupling can be understood from the last set of images, where pin-configuration is changed from 8518 to 8718 and it does not cause any change to the angle of the image but center point is slightly moved by about 250 μm in the +X direction,

which is equal to quarter of wavelength. This change of center point can easily be attributed to the distance of the two pads (5 and 7).

So, in summary the change of this image is caused basically because of the geometry of the gate and drain pad, but it is completely insensitive to source pad and it's geometry or bonding wire position. In case of gate, the length of the gate pad is large enough (~250 µm) to couple the entire radiation and thus, there is no effect of the orientation of gate bonding wire.

Apart from the effect of geometry of metal pad and bonding wire, the effect of drain voltage also causes the asymmetry as reported by many researches[166,167]. To understand the effect of voltage difference between pin-4 and pin-8, current-voltage measurement was done for a small range of voltage (from -100 mV to +100 mV). Equivalent transmission line circuit(left) and current-voltage curves (right) between pin-4 and pin-8 of the device are shown in figure 37. $R_{f\text{-}1}$ to $R_{f\text{-}11}$ represents the drain finger

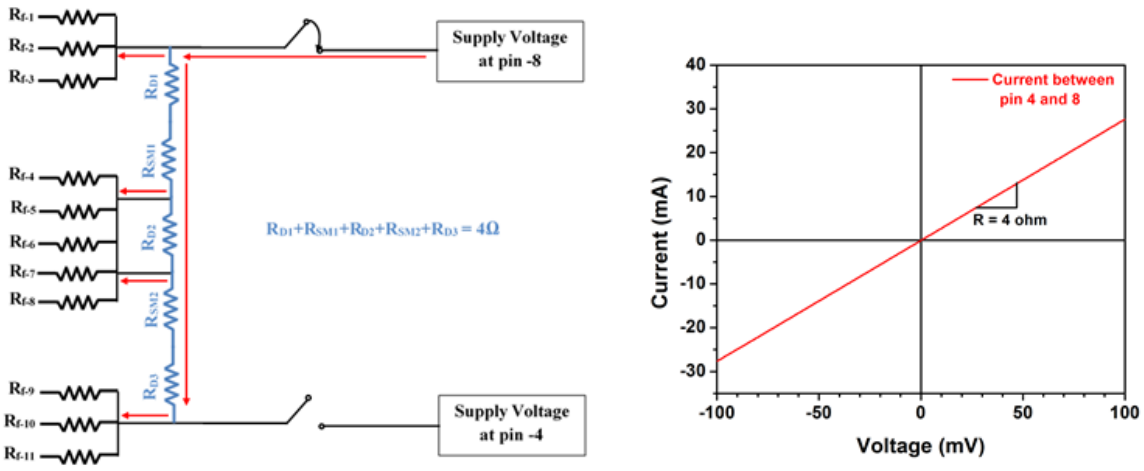

Figure 37. Equivalent transmission line circuit (left) and I-V curve (right) between pin 4 and 8 of the device

resistances of 11 drain fingers respectively. R_{D1},R_{D2} and R_{D3} are the drain pad's resistances, which are connected to pin-8, pin-6 and pin-4 respectively. R_{SM1} represents the resistance of shorting metal between pin-8 and pin-6 and R_{SM2} represents the resistance of shorting metal between pin-6 and pin-4. Direction of current flow is shown in red arrow when pin-8 is connected. When pin-8 is connected and pin-4 remains open, then there is a voltage difference between the two pins. Total resitance between pin-8 and pin-4 was extracted from the I-V measurements and it is 4Ω (figure 37). And the current in the circuit is ~15 mA at V_{GS} = -2.75V and V_{DS} = 200 mV, which is obtained from figure 31(b). So, the voltage difference between pin-8 and pin-4 is 60 mV. To check the effect of drain voltage difference between pin-4 and pin-8, the drain voltage dependent

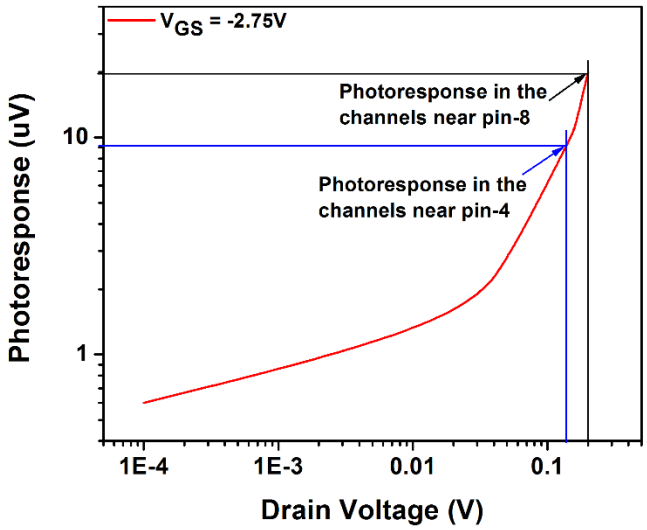

Figure 38. Photoresponse vs Drain voltage for different V_{GS}

photoresponse curve is drawn in figure 38. And it is clearly seen that, photoresponse in the channels near to pin-8 is doubled compared to photoresponse in the channels nearer to

pin-4. There is effect of potential difference between the two drain pads, depending on which pin is connected, on the THz imaging. This voltage difference causes different portions of the multi-channel FET to excite differently than the other for different connection configurations and thus the image pattern changes.

6.3 CONCLUSION

In summary, in a multi channel FET detector, THz imaging depends on geometry of the contact pads and bonding wire orientation and also the voltage difference between different drain pads. In this work, THz radiation was coupled with bonding wires as well as drain contact pads and bonding wire orientation basically defined the angle of the image. The potential difference between drain pads helped to energize some portion of the multi-channel FET more than the other portion and this behavior can be applied in failure analysis of the multi-channel FET. It was also observed that, source pad has almost no effect on coupling the radiation.

CHAPTER SEVEN: FABRICATION AND COMPARATIVE STUDY OF DC AND LOW FREQUENCY NOISE CHARACTERIZATION OF GaN/AlGaN BASED MOS-HEMT AND HEMT

This work presents the effect of Al mole fraction and gate oxide on the DC and low frequency noise characterization of GaN/AlGaN HEMT. MOS-HEMT with SiO_2in the gate stack improved the $I_{d(on)}/I_{d(off)}$ ratio up to more than 8 orders, while it is only ~10 times in conventional HEMT. It was shown that the gate leakage and isolation leakage suppression efficiency improved dramatically with the oxide. Subthreshold swing (SS) of MOS-HEMTs with different Al mole fraction (from 20% to 35%) vary slightly from 72 mV/decade to 79 mV/decade, but the conventional GaN/AlGaN HEMT showed SS of 2.4V/decade. Low frequency noise study revealed the difference in transport mechanism between HEMT and MOS-HEMTs. By using Carrier number fluctuation (CNF) model on the measured data, it was found that the noise is predominantly coming from the surface states. While generation-recombination is very prominent in conventional HEMT, it is very insignificant in both MOS-HEMTs at much higher frequencies. This study reveals that very high number of surface states assisting the tunneling in schottky/AlGaN barrier is responsible for unusually high leakage and higher noise level in conventional HEMT. Leakage level is improved from mA/mm range for HEMT to pA/mm range for MOS-HEMTs. Leakage suppression improvement and minimization of noise level can be

mainly attributed by to high quality SiO_2. Hooge's constant was in the order of $5\text{-}6\times10^{-3}$, which is 5×10^{-2} for conventional HEMT.

AlGaN/GaN high electron mobility transistor (HEMT) is widely known for its wide bandgap properties and high frequency, high power applications[168-171].In addition to that, the 2D Electron gas created due to spontaneous and piezoelectric polarization effect made it to exhibit high electron mobility needed for many applications[172].

For conventional GaN/AlGaN HEMT, high gate and drain leakage currents due to surface states and trap state assisted tunneling are very common in HEMT and thus leakage suppression and high on/off ratio is desired to make a good HEMT[55,56]. Many techniques were followed so far to effectively suppress the leakage and minimize noise level[56-60]. Metal-Oxide-Semiconductor is an effective structure to suppress the gate leakage by creating a blocking insulating layer. But to reduce the leakage effectively and prevent the negative shift of threshold voltage, generally high-k dielectric materials such as hfO_2[61,62], Al_2O_3[63-66]and ZrO_2[67] were used. Not much work has been done on the use of SiO_2 for improving the HEMT performance reported[68].

Low frequency noise measurement is an important characterization method to evaluate the suitability of HEMT's for application in the communication system[173] and it's also a powerful tool to study the impurity and trap states in the device[174,175]. There were many efforts to show the origin of noise in GaN/AlGaN using different models. The tunneling of carriers to 2DEG channel is the main reason for low frequency noise[176,177]. Noise mechanism of MOS-HEMT and HEMT were discussed in some papers[178], but very limited data is available on the thorough comparative study on the effect of Al mole fraction and additional

SiO_2 oxide layer (instead any high-k dielectric material) on DC and low frequency noise characterization of GaN/AlGaN based HEMT.

In this work, the effect of Al mole fraction on the electrical and noise property of MOS-HEMT is studied. And also, the effectiveness of SiO_2 added to HEMT on the electrical and low frequency noise characteristics is compared with conventional GaN/AlGaN HEMT.

7.1 DEVICE STRUCTURE AND FABRICATION

AlGaN/GaN layer structure, grown on c-plane Sapphire substrate using MOCVD technique was used in this study. The layer structure consists of a layer of i-GaN (1 µm

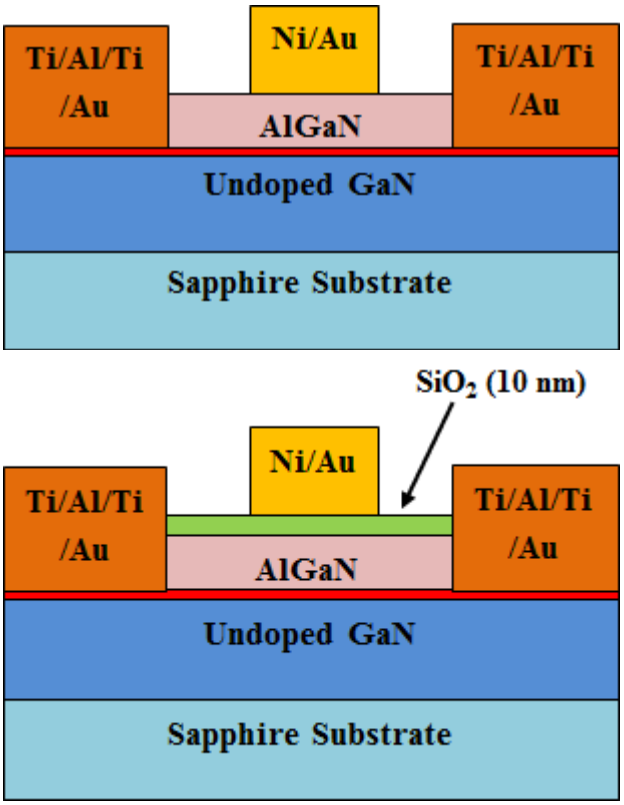

Figure 39. Layer structure of AlGaN/GaN based HEMT (upper) and MOS-HEMT (lower)

thickness) on Sapphire substrate and 1nm of AlN spacer and 20 nm of undoped AlGaN sequentially. The schematic layer structure of AlGaN/GaN conventional HEMT and MOS-HEMT with SiO_2 is shown in figure 39 The first step of FET fabrication was MESA isolation, which was done using Cl_2 based ICP-RIE etching. RF power of 300W and ICP power of 800W was applied in the $Cl_2/N_2/Ar$ ambience to do the MESA etching. Metal mask of Ti/Ni (120/50 nm) was deposited using standard lift-off lithography before MESA patterning. Second layer of micro-lithography was done after that to open the source and drain windows.Then Ti/Al/Ti/Au (30/100/30/30 nm) ohmic metal contacts were deposited using e-beam evaporator with a chamber pressure below $<10^{-7}$ mtorr. In order to make the source and drain contacts more ohmic, RTA annealing was done at 800°C for 40 seconds in Ar gas. For MOS-HEMT device, 10 nm of $SiO_2$was deposited using atomic layer deposition (ALD) technique as a gate dielectric.

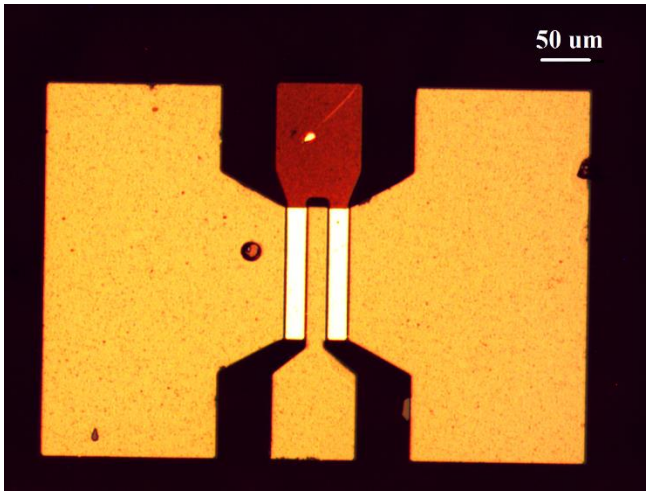

Figure 40. Image of the fabricated GaN/ALGaN FET

finally the gate schottky contact of Ni/Au (120/80 nm) was deposited employing the standard lithographic process and lift-off. Figure 40 is showing the layout image of fabricated device with scale. Gate length and gate width was 40 µm and 153 µm, respectively, for all devices.

7.2 EXPERIMENTAL RESULTS AND DISCUSSION

Electrical characterization of the devices was done by using Agilent B1500A Semiconductor parameter analyzer and the low frequency noise characterization was done using SR770 FFT Spectrum analyzer.

Effect of gate oxide was observed by comparing the results of MOS-HEMT and conventional HEMT. And also, effect of Al mole fraction in the AlGaN layer was observed by comparing the results of two different MOS-HEMTs, one having 20% Al and another having 35% Al mole fraction in the AlGaN layer.

A. Transfer Characteristics

Figure 41(a) shows the DC transfer characteristics of MOS-HEMTs and (b) Gate leakage current under different gate bias. The devices compared are of same dimension having L_g=40µm and W_g =153 µm and t_{ox}=10 nm. Fabricated MOS-HEMTs clearly exhibited depletion type FET behavior. From figure 41(a), Maximum drain current density for MOS-HEMT is 1.38 mA/mm for applied drain voltage of V_{ds} = 0.2V, the off state drain current is ~ 10 pA/mm and calculated I_{on}/I_{off} ratio is greater than 8 orders for MOS-HEMT-1, but slightly less in MOS-HEMT-2 (greater than 7.5×10^7). This low level

of leakage current confirms that SiO_2 quality and also SiO_2/AlGaN interface quality were good and combination of them successfully suppressed the leakage current. The

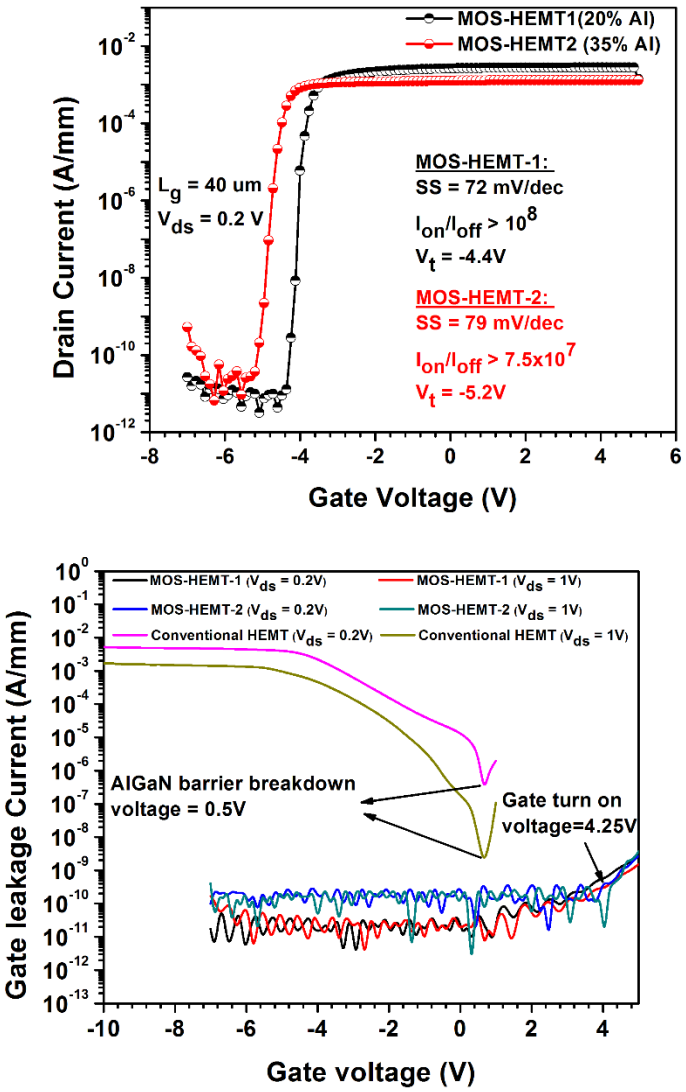

Figure 41. Comparative DC transfer characteristic of (a)(upper one) MOS-HEMTs (20% and 35% Al) and (b)Measured I_g vs V_{gs} of MOS-HEMT-1 and 2 and Conventional HEMT

Subthreshold swing of MOS-HEMT-1 (20% Al) and MOS-HEMT-2 (35% Al) was obtained as 72 mV/decade and 79 mV/decade respectively, which are comparable or

better than reported GaN/AlGaN MOS-HEMT[179-181]. Threshold voltage or pinch off voltage of MOS-HEMT varies from -4.4V to -5.2V for Al mole fraction of 20% and 35% in AlGaN layer, respectively. Figure 41(b) shows the gate leakage current of MOS-HEMT with SiO_2 and conventional HEMT for varying gate bias. The measurements were done at drain voltages of 0.2V and 1V and it is evident from the figure that, gate leakage of MOS-HEMT-1 is almost 10 times smaller than MOS-HEMT-2. This may be attributed to the presence of higher surface states in the oxide-AlGaN interface of the device with 35% Al than for the 20% Al mole fraction. The gate turn-on voltage is 4.25V for both the devices. AlGaN bandgap is dependent on the Al mole fraction in the AlGaN layer and the precise band diagram is shown in figure 42 which was drawn by using the information

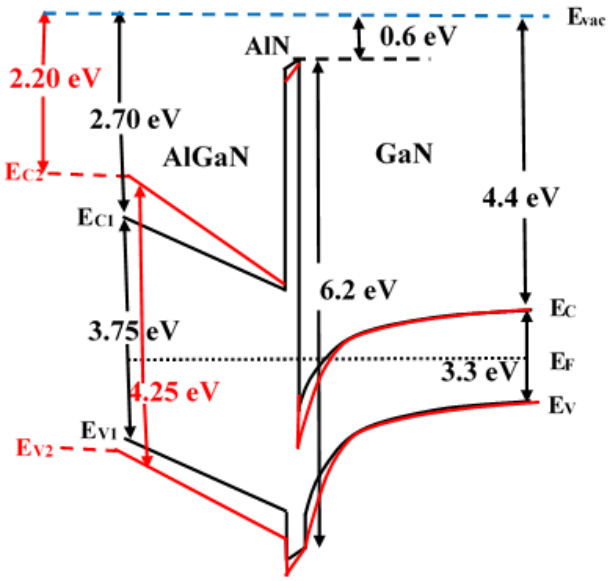

Figure 42. Energy band diagram of GaN/AlGaN for different Al mole fraction [black(20%) and red(35%)]

taken from the literature[182,183.] From the band diagram, it is evident that, with the increase of Al mole fraction, band gap increases, electron affinity decreases and more serious band bending occurs due to increased electric field. So, 2D electron sheet concentration increases and mobility decreases, which consequently decreases the drain current but increases the probability of tunneling of carriers even in the off state. This explains why drain leakage (off-state drain current) increases with the Al mole fraction (see figure 41a). Figure 43 exhibits the transfer characteristic curves for MOS-HEMT-1 and HEMT at V_{ds} of 0.2V and 1V. While the $_{Ion}/I_{off}$ ratio is hardly 10 times in conventional AlGaN/GaN HEMT, it is more than 8 orders of magnitude in case of SiO_2/AlGaN/GaN MOS-HEMT. This drastic improvement with SiO_2 is due to the gate leakage and isolation leakage suppression by the gate oxide. This huge improvement of on-off ratio is better than most other reported literatures[55].Off-state drain leakage of Conventional HEMT was even in the mA/mm range and it may be due to large density of surface states present in the AlGaN layer or the dislocations from GaN layer or substrate. Off state high drain leakage may be attributed to trap assisted tunneling of carriers to the 2DEG channel. The gate leakage current through the schottky barrier in the conventional HEMT is also in the range of mA/mm (figure 41), but it decreases with increasing drain voltage. AlGaN barrier breakdown voltage was observed as 0.5V. Improvement factor, which can be defined as the ratio of on-off current ratio of MOS-HEMT to conventional HEMT and this is greater than 10^7, which is better than the reported results[55]. Moreover, most of the reported results compared MOS-HEMT having high-k dielectric such as hfO_2 or Al_2O_3

with the conventional AlGaN/GaN HEMT. But, in this work, the improvement was achieved using SiO_2 as gate dielectric. Subthreshold swing of the HEMT and MOS-

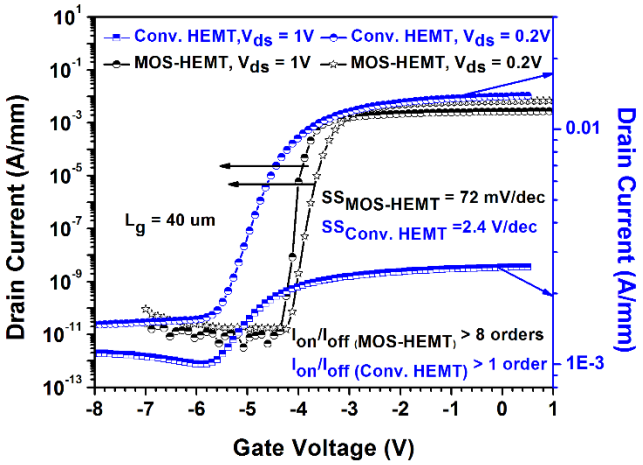

Figure 43. I_D-V_G curves of MOS-HEMT and Conventional HEMT

HEMT is 2.4V/decade and 72 mV/decade respectively, which is a big improvement too.

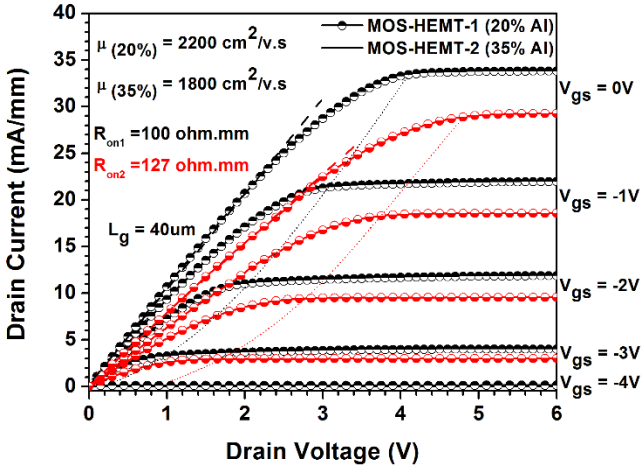

Figure 44. I_D-V_D curves of MOS-HEMT-1 and MOS-HEMT-2. The short dashed line shows the locus of overdrive voltage.

Another important observation was the shift of threshold voltage of the MOS-HEMT to the right compared to conventional HEMT.

B. Output I-V Characteristic curves

Figure 44 shows the output current-voltage characteristic curves (I_d-V_d) of MOS-HEMT-1 and MOS-HEMT-2 for different gate voltages. Maximum drain current at V_{gs} =0V is 33mA/mm for MOS-HEMT-1 while for MOS-HEMT-2, I_{dmax} is 28 mA/mm.

The On-resistance and peak transconductance were calculated as 100 Ω.mm and 127 Ω.mm, respectively, and 6mS/mm and 4.9 mS/mm, respectively, for MOS-HEMT-1 and 2. Extracted mobility of the HEMTs are 2200 cm^2/v.s and 1800 cm^2/v.s which are very close to the Hall measured mobility (2223 cm^2/v.s and 1767 cm^2/v.s respectively) values.

Figure 45 shows the effect of drain voltage on gate leakage current for both the MOS-

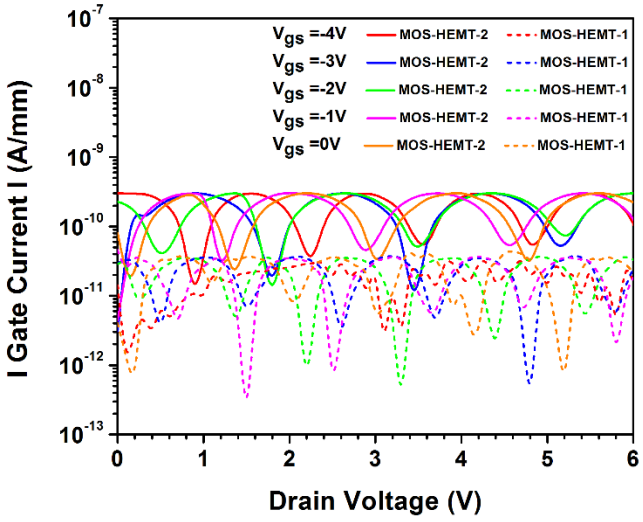

Figure 45. I_G-V_D curves of GaN/AlGaN MOS-HEMTs

HEMTs and it remains same for increasing drain voltage or gate voltage. The I_d-V_d curve in figure 46 shows that saturation drain current is higher in conventional HEMT than in the MOS-HEMT for all the gate voltages. And the on resistance is same 100 Ω.mm for both the devices. The maximum current is 37.5 mA/mm for conventional HEMT whereas it is 33 mA/mm for the MOS-HEMT. Figure 47 shows the gate leakage behavior with drain voltage. For MOS-HEMT it does

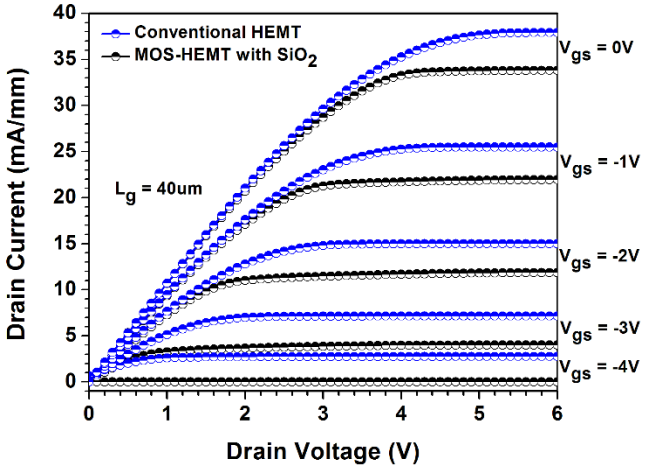

Figure 46. Output I_D-V_D curves of Conventional GaN/AlGaN HEMT and MOS-HEMT

neither increase with drain voltage nor with gate voltage showing a very good leakage suppression by gate oxide. But, in Conventional HEMT, the gate leakage is very high (in mA/mm range) and does not change much with drain voltage. Leakage Current actually flows from source to gate (I_{SG} is shown on right side of the graph) in conventional HEMT. With increasing gate voltage, it went down. At V_{GS} = 0V and drain voltage

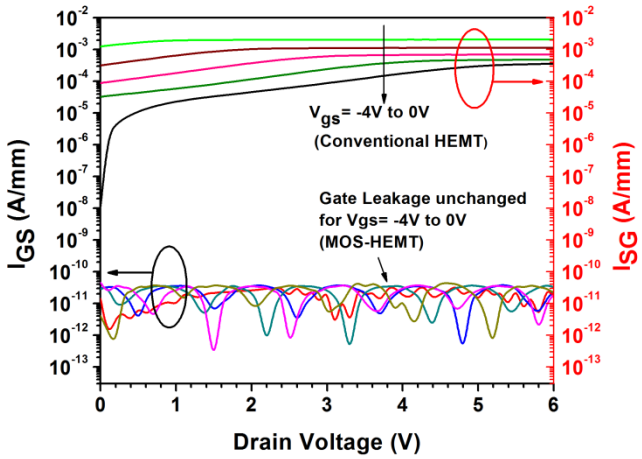

Figure 47. I_G-V_d curves of Conventional GaN/AlGaN HEMT and MOS-HEMT

of few hundred mV, the gate leakage, I_{SG}suddenly rises sharply, showing a poor schottky barrier between Ni/Au gate and AlGaN layer.

C. Low Frequency Noise (LFN) characterization

Figure 48 shows the normalized noise spectral density vs freqency of conventional HEMT from 1 Hz to 10 KHz. All the measurements were done at the drain voltage of 200mV (linear region). in the saturation region (Vg= 0 to ~-3V), the normalized drain current noise PSD follows 1/f pattern till several hundred Hz and a clear generation-recombination bulge is visible at 550 Hz. This confirms the presence of a significant number of trap states in the AlGaN layer of HEMT which explains more clearly why the gate leakage is much higher in conventional HEMT compared to the MOS-HEMT with SiO_2. In the linear region, towards off state from saturation region, it showed increasing relative noise level and follows 1/f pattern. It is because, the lower the current in the

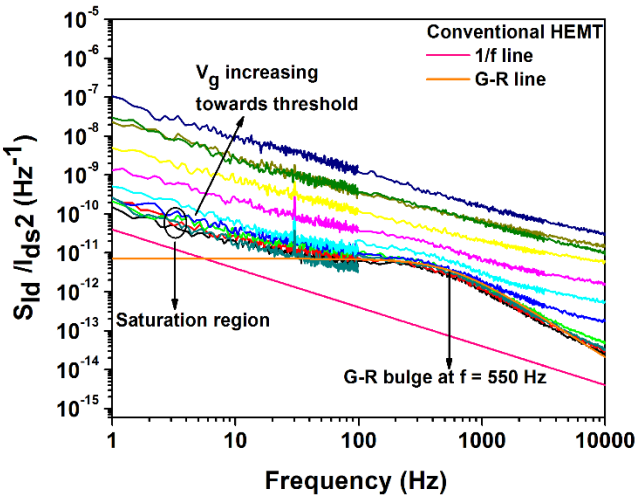

Figure 48. Normalized drain current noise spectral density vs Frequency of conventional GaN/ALGaN HEMT

channel, the higher is relative 1/f noise. Figure 49 and 50 show the normalized I_D noise density spectrum for MOS-HEMT-1 and MOS-HEMT-2. In both the devices, S_{ID}/I_{DS}^2does not change significantly with gate voltages, where I_d is saturated and follows 1/f trend clearly. With the gate voltage increasing towards threshold voltage, the channel current decreases and thus the relative noise also increases though it follows the same 1/f trend. When the device is completely switched off (at V_{gs} = -4.5V for MOS-HEMT-1 and -5.2V for MOS-HEMT-2), it does not follow 1/f trend anymore, but only gives the background noise from the instrument. As it is relative noise PSD, so it gets more sensitive as the current in the channel decreases and maximum is occurred after the pinch off voltage. There is a slight G-R bulge present in both the MOS-HEMT-1 and MOS-HEMT-2 at 4KHz and 2.6 KHz respectively. This insignificantly small but visible G-R

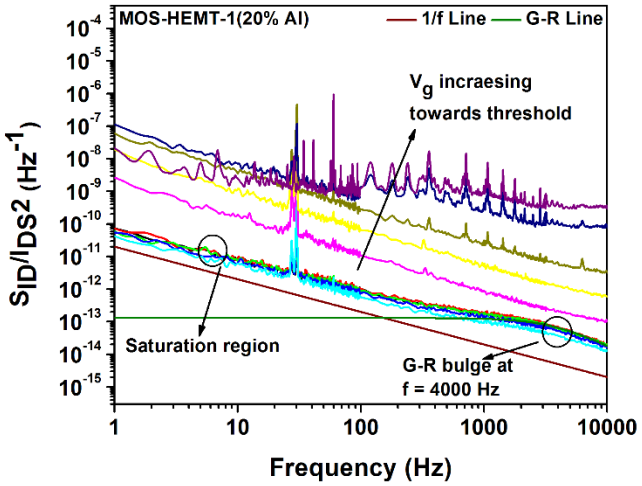

Figure 49. Normalized drain current noise spectral density vs Frequency of MOS- HEMT-1

bulge shows the possibility of having some trap states in the oxide layer of MOS-HEMTs. Figure 51 shows the relative NSD level of all three devices at no applied gate

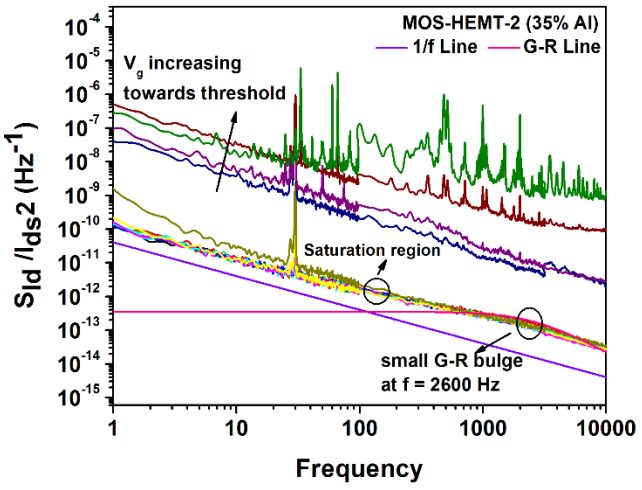

Figure 50. Normalized drain current noise spectral density vs Frequency of MOS- HEMT-2

bias. The graph confirms that MOS-HEMT-1 has the lowest noise level and conventional HEMT has the highest noise. The trap states might have arisen from unintentional doping of AlGaN layer or propagation of dislocations from GaN layer or substrate. MOS-HEMT-2 having a little higher noise level is coherent with the previous gate and drain leakage behavior.

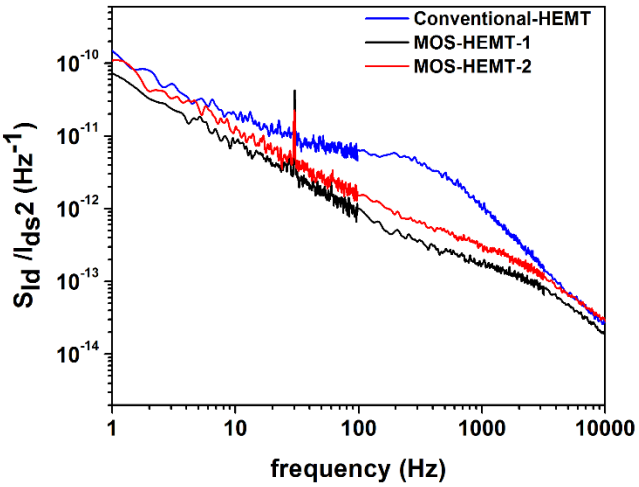

Figure 51. Normalized drain current NSD vs Frequency of all the devices at V_{gs} = 0V

S_{ID}/I_{DS}^2 vs V_{gn} for f =10Hz was plotted in log-log scale in figure 52. V_{gn} is defined as $V_{gn} = (V_{gs}-V_{th})/V_{th}$. Information on the mechanism of noise and the source of G-R noise can be obtained from this graph.

$$\frac{S_I}{I^2} = \frac{S_{RCh}}{R_{Ch}^2}\left(\frac{R_{Ch}}{R_{Ch}+R_{Acc}}\right)^2 + \frac{S_{acc}}{R_{acc}^2}\left(\frac{R_{acc}}{R_{Ch}+R_{Acc}}\right)^2 \quad (11)$$

This is the expression to explain the gate voltage dependence of noise[165]. $\frac{S_{RCh}}{R_{Ch}^2}$ is the spectral noise density of the channel resistance fluctuations, which depends on V_{gn} and consequently follows $1/V_{gn}^2$ line. Access resistance R_{acc}, does not depend on the gate voltage. $\frac{S_{acc}}{R_{acc}^2}$, which is noise of the access resistance, also does not depend on the gate voltage.

Generally, at high gate voltage access resistance dominates the channel resistance and noise of it also dominates, therefore measured noise does not depend on the gate voltage. At small gate voltage channel resistance dominates and noise from it as well[165].

If the channel resistance is still comparable or smaller than the access resistance, then first term in equation (11) dominates and it decreases with the gate voltage faster than $1/V_{gn}^2$. In Conventional HEMT, at V_{gn} greater than 0.1V, it follows the trend line of

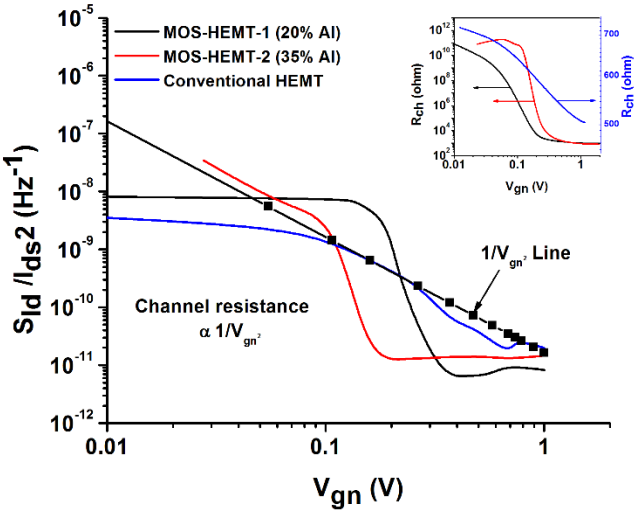

Figure 52. Normalized drain current NSD vs V_{gn} of all the devices at f=10 Hz. Inset is showing the channel resistance vs V_{gn} of the devices.

$1/V_{gn}^2$. In conventional HEMT, channel resistance noise dominates the noise originating from access resistance. Noise in MOS-HEMT-1 decreases with the gate voltage faster than $1/V_{gn}^2$ which means channel resistance noise is smaller or comparable than that of access resistance. For MOS-HEMT-2, at V_{gn}<0.1V, noise spectral density follows $1/V_{gn}^2$showing its dependence on channel resistance at that range of voltage. There are two most popular models to explain the origin of noise mechanism. One is CNF model (Carrie Number Fluctuation), which is a surface phenomenon by trapping and de-trapping the free carriers near the surface[69,184] and the other is HMF model (Hooge's Mobility Fluctuation) model, which explains noise better in the bulk [185]. To reveal the origin of noise fluctuation in the HEMTs, S_{ID}/I_{DS}^2 vs I_{DS} was plotted in log-log scale in figure 53. If variation of S_{ID}/I_{DS}^2 with I_{DS} is proportional to $(G_m/I_{DS})^2$, then the carrier number fluctuation is the source of noise[186,187]. In figure 53, Conventional HEMT and MOS-HEMT bothfollow the trend line of $(G_m/I_{DS})^2$ and thus it can be said that, carrier number

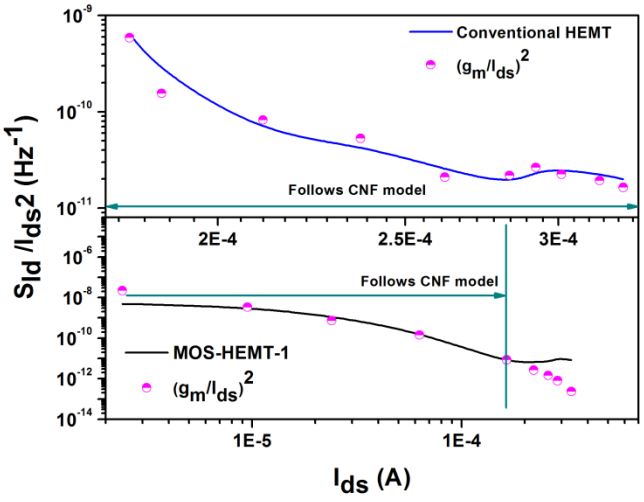

Figure 53. Normalized drain current NSD vs I_{DS} of conventional HEMT and MOS-HEMT at f=10 Hz

fluctuation is the dominant source of noise in the device. This Carrier number fluctuation in conventional HEMT can be attributed to trap assisted tunneling in the AlGaN barrier layer. The carrier number fluctuation in MOS-HEMT might be due to dynamic trapping and de-trapping of carriers at AlGaN/SiO_2 interface. In MOS-HEMT, at very high drain current, resistance of contact and ungated part comes into play and deviates the normalized NSD from CNF model. Figure 54 shows the input gate referred voltage NSD vs (V_{GS}-V_T). For conventional-HEMT, parabolic dependence is clear showing that the correlated mobility fluctuation is also present. In absence of surface correlated mobility fluctuation, the plot should show a constant value. As, the graph has a minima, it has a mixture of acceptor and donor like traps in the oxide interface[188]. In the MOS-HEMT, S_{VG}does not change with gate voltage.

Whatever may be the main sources of noise in a device, Hooge's equation can describe

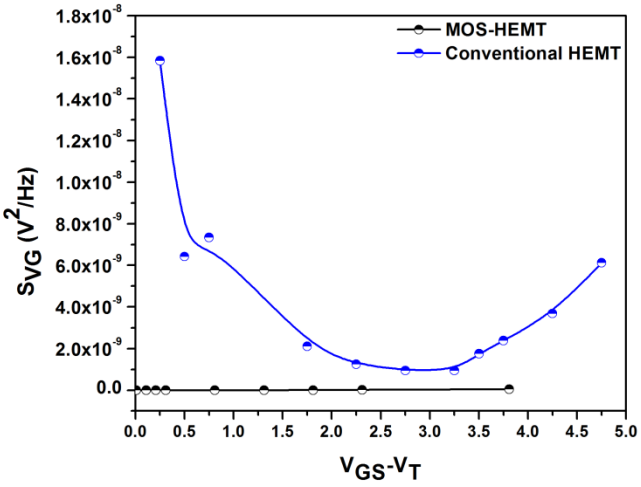

Figure 54. Gate referred voltage NSD vs (V_{GS}-V_T) of conventional HEMT and MOS-HEMT

the noise mechanism if it exhibits 1/f noise. The equation is:

$$\frac{S_I}{I^2} = \frac{\alpha_H}{Nf} \tag{12}$$

Where α_H is the Hooge constant and N is the total number of carriers calculated as $N=(V_{GS}-V_T)\times L\times W\times C_{ox}/q$ where L and W is gate length and width and q is the charge of an electron. Hooge's constant compares directly the noise level of various devices.

Table 4. Comparison of Hooge's constant for conventional HEMT and MOS-HEMTs

	Conventional HEMT	MOS-HEMT-1 (20%)	MOS-HEMT-2 (35%)
Hooge's constant	0.05	0.005	0.006

This value for MOS-HEMT is comparable with already reported literatures[189-191].

7.3 CONCLUSION

In summary, MOS-HEMT with SiO_2 in the gate stack improved the $I_{d(on)}/I_{d(off)}$ ratio up to more than 8 orders, while it is only ~10 times in conventional HEMT. Subthreshold swing (SS) of MOS-HEMTs with different Al mole fraction (from 20% to 35%) vary slightly from 72 mV/decade to 79 mV/decade, but the conventional GaN/AlGaN HEMT showed SS of 2.4V/decade. By using Carrier number fluctuation (CNF) model on the measured data, it was found that the noise is predominantly coming from the surface states. While generation-recombination is very prominent in conventional HEMT, it is very insignificant in both MOS-HEMTs at much higher frequencies. This study revealed that very high number of surface states assisting the tunneling in schottky/AlGaN barrier

is responsible for unusually high leakage and higher noise level in conventional HEMT. Hooge's constant was in the order of $5\text{-}6\times10^{-3}$, which is 5×10^{-2} for conventional HEMT.

CHAPTER EIGHT: CONCLUSION AND FUTURE WORK

Structural, Electrical and optical properties of metal oxide and Group V-VI Chalcogenide based semiconductor materials and their optoelectronic response when used as UV-Visible-NIR photodetectors were studied. Sputter deposited p-NiO/n-ZnO Self-powered ultraviolet (UV) photodetector (PD) showed excellent photoresponse of ~2600 and external quantum efficiency of 63% under UV illumination. Significant performance enhancement of metal oxide based UV detectors was exhibited by fabricating Tin oxide (SnO_2) thin film ultraviolet (UV) photodetectors through incorporation of sputtered Cu clusters that oxidizes in ambience to form CuO. The performance improvement was attributed to enhanced UV absorption and electron transfer facilitated by the nanoheterojunctions between CuO and SnO_2. The peak responsivity of the PDs at a bias of 0.2 V improved from 1.9 A/W in a SnO_2-only device to 10.3 A/W after CuO deposition.

A flexible, low-cost and catalyst-free one-step solution-processed novel approach produced high-quality single-crystalline material with orthorhombic crystal structure and a near-stoichiometric Sb/Se atomic ratio. The fabricated metal-semiconductor-metal photodetectors exhibited fast response, reasonably high responsivity ~ 0.27 A/W as well as excellent mechanical flexibility and durability.

In the study of coupling mechanism of THz radiation in a multi-channel FET,it was observed that, effect of bonding wire orientation is negligible for the large source pad as the radiation is coupled basically between drain and gate pad. Position of activated Drain pad and orientation of respective bonding wire defined the image tilting angle. Drain geometry was observed as the most sensitive to coupling of THz radiation. And there was no effect of gate pad bonding wire orientation on the coupling of THz radiation.

In the comparative study between GaN/AlGaN HEMT and MOS-HEMT with SiO_2, the effect of oxide layer and effect of Al mole fraction on the performance of device was observed.MOS-HEMT with SiO_2 improved the $I_{d(on)}/I_{d(off)}$ ratio up to more than 8 orders, while it is only ~10 times in conventional HEMT. It was shown that the gate leakage and isolation leakage suppression efficiency improved dramatically with the oxide. Subthreshold swing (SS) of MOS-HEMTs with different Al mole fraction (from 20% to 35%) vary slightly from 72 mV/decade to 79 mV/decade, but the conventional GaN/AlGaN HEMT showed SS of 2.4V/decade. It was found that the noise of both devices is predominantly coming from the surface states. While generation-recombination is very pre-dominant in conventional HEMT, it is very insignificant in both MOS-HEMTs at much higher frequencies. Leakage level is improved from mA/mm range for HEMT to pA/mm range for MOS-HEMTs. Hooge's constant, which is a measurement of noise level in the device, was in the order of $5\text{-}6\times10^{-3}$ in MOS-HEMTs, and 5×10^{-2} for conventional HEMT indicating much lower noise level in the MOS-HEMTs.

The future work may include synthesis of good quality V-VI chalcogenide based ternary alloys, which renders the opportunity to vary the composition of alloys and thus tune the bandgap in the near-infrared (NIR) regime. By employing low cost solution processed synthesis technique, Group V-VI chalcogenide materials such as Bi_2Se_3, Bi_2S_3 and their ternary allows such as $Sb_2(Se_xS_{(1-x)})_3$and $Bi_2(Se_xS_{(1-x)})_3$ may be prepared. Engineering the composition of the ternary alloys can vary the bandgap, which will ensure detection of selected frequency spectrum of NIR range wavelength. Future work may also include Modulation of the nanostructure dimensions to understand their effect on optoelectronic application, and Characterizing the synthesized nanostructured materials and photodetector to observe the relation between crystallinity, defect states and efficiency of the devices.

For GaN/AlGaN THz detection, future work may include: (i)fabrication of arrays of GaN/AlGaN (core/shell) nanostructure multi-channel field-effect transistors (FETs) for tunable terahertz (THz) detection in the range 0.5-5 THz at room temperature and (ii) understanding the THz interaction with the FET arrays by utilizing various antenna structures for understanding and improving the radiation coupling.

REFERENCES

1 K. Liu, M. Sakurai, and M. Aono, Sensors **10,** 8604 (2010).

2 E. Monroy, F. Calle, J. L. Pau, E. Muñoz, F. Omnès, B. Beaumont, and P. Gibart, Journal of Crystal Growth **230,** 537 (2001).

3 L. Hu, J. Yan, M. Liao, L. Wu, and X. Fang, Small **7,** 1012 (2011).

4 A. Ohtomo and H. Y. Hwang, Nature **427,** 423 (2004).

5 H. Y. Hwang, Y. Iwasa, M. Kawasaki, B. Keimer, N. Nagaosa, and Y. Tokura, Nat Mater **11,** 103 (2012).

6 M. Mostovoy, Nat Mater **7,** 269 (2008).

7 D. Xiao, W. Zhu, Y. Ran, N. Nagaosa, and S. Okamoto, Nat Commun **2,** 596 (2011).

8 A. Tsukazaki, A. Ohtomo, T. Kita, Y. Ohno, H. Ohno, and M. Kawasaki, Science **315,** 1388 (2007).

9 P. Poizot, S. Laruelle, S. Grugeon, L. Dupont, and J. M. Tarascon, Nature **407,** 496 (2000).

10 J. J. Yang, M. D. Pickett, X. Li, A. A. OhlbergDouglas, D. R. Stewart, and R. S. Williams, Nat Nano **3,** 429 (2008).

11 X. Lang, A. Hirata, T. Fujita, and M. Chen, Nat Nano **6,** 232 (2011).

12 A. Tsukazaki, A. Ohtomo, T. Onuma, M. Ohtani, T. Makino, M. Sumiya, K. Ohtani, S. F. Chichibu, S. Fuke, Y. Segawa, H. Ohno, H. Koinuma, and M. Kawasaki, Nat Mater **4,** 42 (2005).

13 M. Law, L. E. Greene, J. C. Johnson, R. Saykally, and P. Yang, Nat Mater **4,** 455 (2005).

14 R. Ahmad, N. Tripathy, D.-U.-J. Jung, and Y.-B. Hahn, Chemical Communications **50,** 1890 (2014).

15 S. Xu, Y. Qin, C. Xu, Y. Wei, R. Yang, and Z. L. Wang, Nat Nano **5,** 366 (2010).

16 Y. Jin, J. Wang, B. Sun, J. C. Blakesley, and N. C. Greenham, Nano Letters **8,** 1649 (2008).

17 K. Nomura, H. Ohta, A. Takagi, T. Kamiya, M. Hirano, and H. Hosono, Nature **432,** 488 (2004).

18 N. Xu, L. Liu, X. Sun, X. Liu, D. Han, Y. Wang, R. Han, J. Kang, and B. Yu, Applied Physics Letters **92,** 232112 (2008).

19 J. M. Caruge, J. E. Halpert, V. Wood, V. Bulovic, and M. G. Bawendi, Nat Photon **2,** 247 (2008).

20 R. Waser and M. Aono, Nat Mater **6,** 833 (2007).

[21] K. Oka, T. Yanagida, K. Nagashima, H. Tanaka, and T. Kawai, Journal of the American Chemical Society **131,** 3434 (2009).
[22] E. A. Gibson, A. L. Smeigh, L. Le Pleux, J. Fortage, G. Boschloo, E. Blart, Y. Pellegrin, F. Odobel, A. Hagfeldt, and L. Hammarström, Angewandte Chemie **121,** 4466 (2009).
[23] Y. Y. Xi, Y. F. Hsu, A. B. Djurisic, A. M. C. Ng, W. K. Chan, H. L. Tam, and K. W. Cheah, Applied Physics Letters **92,** 113505 (2008).
[24] H. Ohta, M. Hirano, K. Nakahara, H. Maruta, T. Tanabe, M. Kamiya, T. Kamiya, and H. Hosono, Applied Physics Letters **83,** 1029 (2003).
[25] D. Y. Kim, J. Ryu, J. Manders, J. Lee, and F. So, ACS Applied Materials & Interfaces **6,** 1370 (2014).
[26] N. Park, K. Sun, Z. L. Sun, Y. Jing, and D. L. Wang, Journal of Materials Chemistry C **1,** 7333 (2013).
[27] X. M. Chen, K. B. Ruan, G. H. Wu, and D. H. Bao, Applied Physics Letters **93,** 3 (2008).
[28] Y. Y. Xi, Y. F. Hsu, A. B. Djurišić, A. M. C. Ng, W. K. Chan, H. L. Tam, and K. W. Cheah, Applied Physics Letters **92,** 113505 (2008).
[29] S.-Y. Tsai, M.-H. Hon, and Y.-M. Lu, Solid-State Electronics **63,** 37 (2011).
[30] Y. Vygranenko, K. Wang, and A. Nathan, Applied Physics Letters **89,** 172105 (2006).
[31] N. Park, K. Sun, Z. Sun, Y. Jing, and D. Wang, Journal of Materials Chemistry C **1,** 7333 (2013).
[32] D. Y. Kim, J. Ryu, J. Manders, J. Lee, and F. So, ACS Applied Materials & Interfaces **6,** 1370 (2014).
[33] P. Bhattacharya, R. R. Das, and R. S. Katiyar, Thin Solid Films **447,** 564 (2004).
[34] J. A. Rogers, T. Someya, and Y. Huang, in *science* (2010), p. 1603.
[35] I. M. A. L. Salas-Villasenor, M. A. Quevedo-Lopez, in *ECS Journal of Solid State Science and Technology* (2014), p. 107.
[36] B. L. Xianfu Wang, Qiufan Wang, Weifeng Song, Xiaojuan Hou, Di Chen, Yi-bing Cheng, Guozhen Shen, in *Advanced Materials* (2013), p. 1479.
[37] R. Huang, J. Zhang, F. Wei, L. Shi, T. Kong, and G. Cheng, in *Advanced Functional Materials* (2014), p. 3581.
[38] T. W. Case, in *Physical Review* (1917), p. 305.
[39] D. J. Choi, Yamujin Lee,JeeHee Jeong,Gyoung Hwa Whang,Dongmok Hwang,Sung Woo Cho,Kyung-Sang Kim,Sang-Wook, in *Scientific Reports* (2014), p. 6714.
[40] Y. W. Jianmin Ma, Yijing Wang, Qing Chen, Jiabiao Lian, and Wenjun Zheng, in *The Journal of Physical Chemistry* (2009), p. 13588.
[41] M. L. Ying Zhou, Zhe Xia, Jie Zhong, Huaibing Song, Xinsheng Liu, Bo Yang, Junpei Zhang, Jie Chen, Kunhao Zhou, Junbo Han, Yibing Cheng, Jiang Tang, in *Advanced Energy Materials* (2014), p. 1846.
[42] Y.-Q. Liu, M. Zhang, F.-X. Wang, and G.-B. Pan, Journal of Materials Chemistry C **2,** 240 (2014).

[43] X. Fang, S. Xiong, T. Zhai, Y. Bando, M. Liao, U. K. Gautam, Y. Koide, X. Zhang, Y. Qian, and D. Golberg, Advanced Materials **21,** 5016 (2009).
[44] Y. Jiang, W. J. Zhang, J. S. Jie, X. M. Meng, X. Fan, and S. T. Lee, Advanced Functional Materials **17,** 1795 (2007).
[45] S.-C. Kung, W. E. van der Veer, F. Yang, K. C. Donavan, and R. M. Penner, Nano Letters **10,** 1481 (2010).
[46] J.-J. Wang, F.-F. Cao, L. Jiang, Y.-G. Guo, W.-P. Hu, and L.-J. Wan, Journal of the American Chemical Society **131,** 15602 (2009).
[47] W. Knap, M. Dyakonov, D. Coquillat, F. Teppe, N. Dyakonova, J. Łusakowski, K. Karpierz, M. Sakowicz, G. Valusis, D. Seliuta, I. Kasalynas, A. El Fatimy, Y. M. Meziani, and T. Otsuji, Journal of Infrared, Millimeter, and Terahertz Waves **30,** 1319 (2009).
[48] E. A. Shaner, M. C. Wanke, A. D. Grine, S. K. Lyo, J. L. Reno, and S. J. Allen, Applied Physics Letters **90,** 181127 (2007).
[49] X. G. Peralta, S. J. Allen, M. C. Wanke, N. E. Harff, J. A. Simmons, M. P. Lilly, J. L. Reno, P. J. Burke, and J. P. Eisenstein, Applied Physics Letters **81,** 1627 (2002).
[50] M. Dyakonov and M. Shur, IEEE Transactions on Electron Devices **43,** 380 (1996).
[51] W. Knap, J. Lusakowski, T. Parenty, S. Bollaert, A. Cappy, V. V. Popov, and M. S. Shur, Applied Physics Letters **84,** 2331 (2004).
[52] M. Sakowicz, J. Łusakowski, K. Karpierz, M. Grynberg, W. Knap, and W. Gwarek, Journal of Applied Physics **104,** 024519 (2008).
[53] D. B. Veksler, A. V. Muravjov, V. Y. Kachorovskii, T. A. Elkhatib, K. N. Salama, X. C. Zhang, and M. S. Shur, Solid-State Electronics **53,** 571 (2009).
[54] C. Wai Lam, D. Jason, and M. M. Daniel, Reports on Progress in Physics **70,** 1325 (2007).
[55] S. Ogyun, A. Woojin, H. Min-Koo, and H. Min-Woo, Semiconductor Science and Technology **28,** 025001 (2013).
[56] W. Saito, M. Kuraguchi, Y. Takada, K. Tsuda, I. Omura, and T. Ogura, IEEE Transactions on Electron Devices **52,** 159 (2005).
[57] J. W. Chung, J. C. Roberts, E. L. Piner, and T. Palacios, IEEE Electron Device Letters **29,** 1196 (2008).
[58] R. Chu, L. Shen, N. Fichtenbaum, D. Brown, S. Keller, and U. K. Mishra, IEEE Electron Device Letters **29,** 297 (2008).
[59] V. Adivarahan, M. Gaevski, W. H. Sun, H. Fatima, A. Koudymov, S. Saygi, G. Simin, J. Yang, M. A. Khan, A. Tarakji, M. S. Shur, and R. Gaska, IEEE Electron Device Letters **24,** 541 (2003).
[60] W. Saito, M. Kuraguchi, Y. Takada, K. Tsuda, I. Omura, and T. Ogura, IEEE Transactions on Electron Devices **51,** 1913 (2004).
[61] C. Liu, E. F. Chor, and L. S. Tan, Applied Physics Letters **88,** 173504 (2006).
[62] J. Shi, L. F. Eastman, X. Xin, and M. Pophristic, Applied Physics Letters **95,** 042103 (2009).

[63] Z. H. Liu, G. I. Ng, S. Arulkumaran, Y. K. T. Maung, K. L. Teo, S. C. Foo, and V. Sahmuganathan, IEEE Electron Device Letters **31,** 803 (2010).
[64] M. Kanamura, T. Ohki, T. Kikkawa, K. Imanishi, T. Imada, A. Yamada, and N. Hara, IEEE Electron Device Letters **31,** 189 (2010).
[65] Z. H. Liu, G. I. Ng, S. Arulkumaran, Y. K. T. Maung, K. L. Teo, S. C. Foo, V. Sahmuganathan, T. Xu, and C. H. Lee, IEEE Electron Device Letters **31,** 96 (2010).
[66] J. F. Joseph, K. Toshiharu, S. L. Selvaraj, and E. Takashi, Japanese Journal of Applied Physics **50,** 04DF03 (2011).
[67] K. Balachander, S. Arulkumaran, H. Ishikawa, K. Baskar, and T. Egawa, physica status solidi (a) **202,** R16 (2005).
[68] V. Adivarahan, J. Yang, A. Koudymov, G. Simin, and M. A. Khan, IEEE Electron Device Letters **26,** 535 (2005).
[69] M. Amani, M. L. Chin, A. G. Birdwell, T. P. O'Regan, S. Najmaei, Z. Liu, P. M. Ajayan, J. Lou, and M. Dubey, Applied Physics Letters **102,** 193107 (2013).
[70] M. v. Haartman and M. Östling, in *Low-Frequency Noise In Advanced Mos Devices* (Springer Netherlands, Dordrecht, 2007), p. 1.
[71] T. Someya, Nat Mater **9,** 879 (2010).
[72] J. Wang, C. Yan, M.-F. Lin, K. Tsukagoshi, and P. S. Lee, J. Mater. Chem. C **3,** 596 (2015).
[73] G. Chen, B. Liang, Z. Liu, G. Yu, X. Xie, T. Luo, Z. Xie, D. Chen, M.-Q. Zhu, and G. Shen, J. Mater. Chem. C **2,** 1270 (2014).
[74] X. Xie and G. Shen, Nanoscale **7,** 5046 (2015).
[75] Z. Gao, W. Jin, Y. Zhou, Y. Dai, B. Yu, C. Liu, W. Xu, Y. Li, H. Peng, Z. Liu, and L. Dai, Nanoscale **5,** 5576 (2013).
[76] J. Qi, X. Hu, Z. Wang, X. Li, W. Liu, and Y. Zhang, Nanoscale **6,** 6025 (2014).
[77] H.-Y. Chen, K.-W. Liu, X. Chen, Z.-Z. Zhang, M.-M. Fan, M.-M. Jiang, X.-H. Xie, H.-F. Zhao, and D.-Z. Shen, J. Mater. Chem. C **2,** 9689 (2014).
[78] H. Zhou, P. Gui, Q. Yu, J. Mei, H. Wang, and G. Fang, J. Mater. Chem. C **3,** 990 (2015).
[79] Y. Shen, X. Yan, Z. Bai, X. Zheng, Y. Sun, Y. Liu, P. Lin, X. Chen, and Y. Zhang, RSC Adv. **5,** 5976 (2015).
[80] Y. Q. Bie, Z. M. Liao, H. Z. Zhang, G. R. Li, Y. Ye, Y. B. Zhou, J. Xu, Z. X. Qin, L. Dai, and D. P. Yu, Adv Mater **23,** 649 (2011).
[81] F. D. Auret, S. A. Goodman, M. Hayes, M. J. Legodi, H. A. van Laarhoven, and D. C. Look, Applied Physics Letters **79,** 3074 (2001).
[82] S. Das, S. Chakrabarti, and S. Chaudhuri, Journal of Physics D-Applied Physics **38,** 4021 (2005).
[83] S. M. Hatch, J. Briscoe, and S. Dunn, Advanced Materials **25,** 867 (2013).
[84] T. Xie, G. Liu, B. Wen, J. Y. Ha, N. V. Nguyen, A. Motayed, and R. Debnath, ACS Applied Materials & Interfaces (2015).
[85] R. Debnath, T. Xie, B. M. Wen, W. Li, J. Y. Ha, N. F. Sullivan, N. V. Nguyen, and A. Motayed, Rsc Advances **5,** 14646 (2015).
[86] Y. Vygranenko, K. Wang, and A. Nathan, Applied Physics Letters **89** (2006).

[87] M. C. Biesinger, B. P. Payne, L. W. M. Lau, A. Gerson, and R. S. C. Smart, Surface and Interface Analysis **41,** 324 (2009).
[88] X. Liu, J. Zhang, L. Wang, T. Yang, X. Guo, S. Wu, and S. Wang, J. Mater. Chem. **21,** 349 (2011).
[89] H.-M. Chiu and J.-M. Wu, Journal of Materials Chemistry A **1,** 5524 (2013).
[90] T. Ghosh and D. Basak, Journal of Physics D: Applied Physics **42,** 145304 (2009).
[91] J. P. Kar, S. N. Das, J. H. Choi, Y. A. Lee, T. Y. Lee, and J. M. Myoung, Journal of Crystal Growth **311,** 3305 (2009).
[92] M. R. Hasan, T. Xie, S. C. Barron, G. Liu, N. V. Nguyen, A. Motayed, M. V. Rao, and R. Debnath, APL Mater. **3,** 106101 (2015).
[93] Y. H. Ko, G. Nagaraju, and J. S. Yu, Nanoscale **7,** 2735 (2015).
[94] W. Tian, C. Zhang, T. Y. Zhai, S. L. Li, X. Wang, J. W. Liu, X. Jie, D. Q. Liu, M. Y. Liao, Y. Koide, D. Golberg, and Y. Bando, Advanced Materials **26,** 3088 (2014).
[95] T. Xie, M. R. Hasan, B. Qiu, E. S. Arinze, N. V. Nguyen, A. Motayed, S. M. Thon, and R. Debnath, Applied Physics Letters **107,** 241108 (2015).
[96] H. E. Katz, A. J. Lovinger, J. Johnson, C. Kloc, T. Siegrist, W. Li, Y. Y. Lin, and A. Dodabalapur, Nature **404,** 478 (2000).
[97] C. R. Kagan, D. B. Mitzi, and C. D. Dimitrakopoulos, Science **286,** 945 (1999).
[98] H. Sirringhaus, T. Kawase, R. H. Friend, T. Shimoda, M. Inbasekaran, W. Wu, and E. P. Woo, Science **290,** 2123 (2000).
[99] B. A. Ridley, B. Nivi, and J. M. Jacobson, Science **286,** 746 (1999).
[100] D. B. Mitzi, L. L. Kosbar, C. E. Murray, M. Copel, and A. Afzali, Nature **428,** 299 (2004).
[101] X. Duan, C. Niu, V. Sahi, J. Chen, J. W. Parce, S. Empedocles, and J. L. Goldman, Nature **425,** 274 (2003).
[102] D. B. Mitzi, M. Copel, and S. J. Chey, Advanced Materials **17,** 1285 (2005).
[103] F. Zhang, C.-a. Di, N. Berdunov, Y. Hu, Y. Hu, X. Gao, Q. Meng, H. Sirringhaus, and D. Zhu, Advanced Materials **25,** 1401 (2013).
[104] H. E. A. Huitema, G. H. Gelinck, J. B. P. H. van der Putten, K. E. Kuijk, C. M. Hart, E. Cantatore, P. T. Herwig, A. J. J. M. van Breemen, and D. M. de Leeuw, Nature **414,** 599 (2001).
[105] A. R. Brown, A. Pomp, C. M. Hart, and D. M. de Leeuw, Science **270,** 972 (1995).
[106] F. Garnier, R. Hajlaoui, A. Yassar, and P. Srivastava, Science **265,** 1684 (1994).
[107] G. H. Gelinck, H. E. A. Huitema, E. van Veenendaal, E. Cantatore, L. Schrijnemakers, J. B. P. H. van der Putten, T. C. T. Geuns, M. Beenhakkers, J. B. Giesbers, B.-H. Huisman, E. J. Meijer, E. M. Benito, F. J. Touwslager, A. W. Marsman, B. J. E. van Rens, and D. M. de Leeuw, Nat Mater **3,** 106 (2004).
[108] Y. Sun, G. C. Welch, W. L. Leong, C. J. Takacs, G. C. Bazan, and A. J. Heeger, Nat Mater **11,** 44 (2012).
[109] D. B. Mitzi, Journal of Materials Chemistry **14,** 2355 (2004).

[110] J.-S. Lee, M. V. Kovalenko, J. Huang, D. S. Chung, and D. V. Talapin, Nat Nano **6,** 348 (2011).
[111] A. M. Smith and S. Nie, Accounts of Chemical Research **43,** 190 (2010).
[112] P. K. Nair, M. T. S. Nair, V. M. García, O. L. Arenas, A. C. Y. Peña, I. T. Ayala, O. Gomezdaza, A. Sánchez, J. Campos, H. Hu, R. Suárez, and M. E. Rincón, Solar Energy Materials and Solar Cells **52,** 313 (1998).
[113] O. Niitsoo, S. K. Sarkar, C. Pejoux, S. Rühle, D. Cahen, and G. Hodes, Journal of Photochemistry and Photobiology A: Chemistry **181,** 306 (2006).
[114] H. Lee, M. Wang, P. Chen, D. R. Gamelin, S. M. Zakeeruddin, M. Grätzel, and M. K. Nazeeruddin, Nano Letters **9,** 4221 (2009).
[115] H. J. Lee, J. Bang, J. Park, S. Kim, and S.-M. Park, Chemistry of Materials **22,** 5636 (2010).
[116] S. A. Studenikin, N. Golego, and M. Cocivera, Journal of Applied Physics **84,** 2287 (1998).
[117] F. Paraguay D, W. Estrada L, D. R. Acosta N, E. Andrade, and M. Miki-Yoshida, Thin Solid Films **350,** 192 (1999).
[118] Y. Zhou, L. Wang, S. Chen, S. Qin, X. Liu, J. Chen, D.-J. Xue, M. Luo, Y. Cao, Y. Cheng, E. H. Sargent, and J. Tang, Nat Photon **9,** 409 (2015).
[119] D. Morelli, V. Jovovic, and J. Heremans, Physical review letters **101,** 035901 (2008).
[120] G. Domingo, R. Itoga, and C. Kannewurf, Physical Review **143,** 536 (1966).
[121] Y. C. Choi, T. N. Mandal, W. S. Yang, Y. H. Lee, S. H. Im, J. H. Noh, and S. I. Seok, Angewandte Chemie **126,** 1353 (2014).
[122] Y. Kim, A. DiVenere, G. K. L. Wong, J. B. Ketterson, S. Cho, and J. R. Meyer, Journal of Applied Physics **91,** 715 (2002).
[123] A. Boulouz, S. Chakraborty, A. Giani, F. P. Delannoy, A. Boyer, and J. Schumann, Journal of Applied Physics **89,** 5009 (2001).
[124] R. Huang, J. Zhang, F. Wei, L. Shi, T. Kong, and G. Cheng, Advanced Functional Materials **24,** 3581 (2014).
[125] T. Zhai, M. Ye, L. Li, X. Fang, M. Liao, Y. Li, Y. Koide, Y. Bando, and D. Golberg, Advanced Materials **22,** 4530 (2010).
[126] M. Wuttig and N. Yamada, Nat Mater **6,** 824 (2007).
[127] R. B. Yang, J. Bachmann, E. Pippel, A. Berger, J. Woltersdorf, U. Gösele, and K. Nielsch, Advanced Materials **21,** 3170 (2009).
[128] F. Verger, V. Nazabal, F. Colas, P. Němec, C. Cardinaud, E. Baudet, R. Chahal, E. Rinnert, K. Boukerma, I. Peron, S. Deputier, M. Guilloux-Viry, J. P. Guin, H. Lhermite, A. Moreac, C. Compère, and B. Bureau, Optical Materials Express **3,** 2112 (2013).
[129] M. Luo, M. Leng, X. Liu, J. Chen, C. Chen, S. Qin, and J. Tang, Applied Physics Letters **104,** 173904 (2014).
[130] N. V. Tarakina, S. Schreyeck, T. Borzenko, C. Schumacher, G. Karczewski, K. Brunner, C. Gould, H. Buhmann, and L. W. Molenkamp, Crystal Growth & Design **12,** 1913 (2012).

[131] D. H. Webber and R. L. Brutchey, Journal of the American Chemical Society **135,** 15722 (2013).
[132] T. K. Todorov, K. B. Reuter, and D. B. Mitzi, Advanced Materials **22,** E156 (2010).
[133] C. L. McCarthy, D. H. Webber, E. C. Schueller, and R. L. Brutchey, Angewandte Chemie **127,** 8498 (2015).
[134] G. Chen, W. Wang, C. Wang, T. Ding, and Q. Yang, Advanced Science **2,** 1500109 (2015).
[135] P. I. Hsu, R. Bhattacharya, H. Gleskova, M. Huang, Z. Xi, Z. Suo, S. Wagner, and J. C. Sturm, Applied Physics Letters **81,** 1723 (2002).
[136] G. Cliff and G. W. Lorimer, Journal of Microscopy **103,** 203 (1975).
[137] R. F. Egerton, *Electron Energy-loss Spectrometry in the Electron Microscope*, 3rd Edition ed. (Plenum, New York, 2011).
[138] N. Maiti, S. H. Im, Y. H. Lee, C.-H. Kim, and S. I. Seok, CrystEngComm **13,** 3767 (2011).
[139] X. Liu, J. Chen, M. Luo, M. Leng, Z. Xia, Y. Zhou, S. Qin, D.-J. Xue, L. Lv, H. Huang, D. Niu, and J. Tang, ACS Applied Materials & Interfaces **6,** 10687 (2014).
[140] P. Makreski, G. Petruševski, S. Ugarković, and G. Jovanovski, Vibrational Spectroscopy **68,** 177 (2013).
[141] Y. K. Kadıoğlu, Z. Üstündağ, K. Deniz, C. Yenikaya, and Y. Erdoğan, Instrumentation Science & Technology **37,** 683 (2009).
[142] T. P. Mernagh and A. G. Trudu, Chemical Geology **103,** 113 (1993).
[143] C. A. Cody, L. DiCarlo, and R. K. Darlington, Inorganic Chemistry **18,** 1572 (1979).
[144] G. Mestl, P. Ruiz, B. Delmon, and H. Knozinger, The Journal of Physical Chemistry **98,** 11283 (1994).
[145] J. Tauc, R. Grigorovici, and A. Vancu, physica status solidi (b) **15,** 627 (1966).
[146] B. Yang, D.-J. Xue, M. Leng, J. Zhong, L. Wang, H. Song, Y. Zhou, and J. Tang, Scientific Reports **5,** 10978 (2015).
[147] F. Perales, G. Lifante, F. Agulló-Rueda, and C. d. l. Heras, Journal of Physics D: Applied Physics **40,** 2440 (2007).
[148] Y. Rodríguez-Lazcano, M. T. S. Nair, and P. K. Nair, Journal of The Electrochemical Society **152,** G635 (2005).
[149] M. Tonouchi, Nat Photon **1,** 97 (2007).
[150] P. H. Siegel, IEEE Transactions on Microwave Theory and Techniques **50,** 910 (2002).
[151] P. Mukherjee and B. Gupta, International Journal of Infrared and Millimeter Waves **29,** 1091 (2008).
[152] G. K. Kitaeva, Laser Physics Letters **5,** 559 (2008).
[153] K. L. Vodopyanov, Laser Physics **19,** 305 (2009).
[154] J. Federici and L. Moeller, Journal of Applied Physics **107,** 111101 (2010).
[155] R. Appleby and H. B. Wallace, IEEE Transactions on Antennas and Propagation **55,** 2944 (2007).

[156] F. F. John, S. Brian, H. Feng, G. Dale, B. Robert, O. Filipe, and Z. David, Semiconductor Science and Technology **20,** S266 (2005).
[157] J. A. Zeitler and L. F. Gladden, European Journal of Pharmaceutics and Biopharmaceutics **71,** 2 (2009).
[158] P. H. Siegel, IEEE Transactions on Microwave Theory and Techniques **52,** 2438 (2004).
[159] Y. L. Hor, J. F. Federici, and R. L. Wample, Applied Optics **47,** 72 (2008).
[160] J. F. Federici, R. L. Wample, D. Rodriguez, and S. Mukherjee, Applied Optics **48,** 1382 (2009).
[161] M. Dyakonov and M. Shur, Physical Review Letters **71,** 2465 (1993).
[162] D. Veksler, A. Muraviev, T. Elkhatib, K. Salama, and M. Shur, in *Plasma wave FET for sub-wavelength THz imaging*, 2007 (IEEE), p. 1.
[163] W. Knap, V. Kachorovskii, Y. Deng, S. Rumyantsev, J.-Q. Lü, R. Gaska, M. S. Shur, G. Simin, X. Hu, M. A. Khan, C. A. Saylor, and L. C. Brunel, Journal of Applied Physics **91,** 9346 (2002).
[164] Y. M. Meziani, T. Otsuji, M. Hanabe, T. Ishibashi, T. Uno, and E. Sano, Applied Physics Letters **90,** 061105 (2007).
[165] S. L. Rumyantsev, Y. Deng, S. Shur, M. E. Levinshtein, M. A. Khan, G. Simin, J. Yang, X. Hu, and R. Gaska, Semiconductor Science and Technology **18,** 589 (2003).
[166] S. Boubanga-Tombet, F. Teppe, D. Coquillat, S. Nadar, N. Dyakonova, H. Videlier, W. Knap, A. Shchepetov, C. Gardès, Y. Roelens, S. Bollaert, D. Seliuta, R. Vadoklis, and G. Valušis, Applied Physics Letters **92,** 212101 (2008).
[167] D. Veksler, F. Teppe, A. Dmitriev, V. Y. Kachorovskii, W. Knap, and M. Shur, Physical Review B **73,** 125328 (2006).
[168] M. N. Yoder, IEEE Transactions on Electron Devices **43,** 1633 (1996).
[169] Y. F. Wu, B. P. Keller, S. Keller, N. X. Nguyen, M. Le, C. Nguyen, T. J. Jenkins, L. T. Kehias, S. P. Denbaars, and U. K. Mishra, IEEE Electron Device Letters **18,** 438 (1997).
[170] Y. Uemoto, D. Shibata, M. Yanagihara, H. Ishida, H. Matsuo, S. Nagai, N. Batta, M. Li, T. Ueda, T. Tanaka, and D. Ueda, in *8300V Blocking Voltage AlGaN/GaN Power HFET with Thick Poly-AlN Passivation*, 2007, p. 861.
[171] Y. F. Wu, A. Saxler, M. Moore, R. P. Smith, S. Sheppard, P. M. Chavarkar, T. Wisleder, U. K. Mishra, and P. Parikh, IEEE Electron Device Letters **25,** 117 (2004).
[172] O. Ambacher, J. Smart, J. R. Shealy, N. G. Weimann, K. Chu, M. Murphy, W. J. Schaff, L. F. Eastman, R. Dimitrov, L. Wittmer, M. Stutzmann, W. Rieger, and J. Hilsenbeck, Journal of Applied Physics **85,** 3222 (1999).
[173] M. E. Levinshtein, S. L. Rumyantsev, R. Gaska, J. W. Yang, and M. S. Shur, Applied Physics Letters **73,** 1089 (1998).
[174] B. K. Jones, IEEE Transactions on Electron Devices **41,** 2188 (1994).
[175] M. E. Levinshtein and S. L. Rumyantsev, Semiconductor Science and Technology **9,** 1183 (1994).

[176] S. L. Rumyantsev, N. Pala, M. S. Shur, R. Gaska, M. E. Levinshtein, P. A. Ivanov, M. A. Khan, G. Simin, X. Hu, and J. Yang, Semiconductor Science and Technology **17,** 476 (2002).
[177] S. L. RUMYANTSEV, N. PALA, M. S. SHUR, M. E. LEVINSHTEIN, P. A. IVANOV, M. A. KHAN, G. SIMIN, J. YANG, X. HU, A. TARAKJI, and R. GASKA, Fluctuation and Noise Letters **01,** L221 (2001).
[178] F. Crupi, P. Magnone, S. Strangio, F. Iucolano, and G. Meneghesso, IEEE Transactions on Electron Devices **63,** 2219 (2016).
[179] J. F. Joseph, E. Takashi, Y. Yuya, Y. Yoshiki, U. Akinori, T. Toshiya, and M. Koh, Applied Physics Express **7,** 041003 (2014).
[180] H. Y. Liu, B. Y. Chou, W. C. Hsu, C. S. Lee, J. K. Sheu, and C. S. Ho, IEEE Transactions on Electron Devices **60,** 213 (2013).
[181] J. J. Freedsman, T. Kubo, and T. Egawa, IEEE Transactions on Electron Devices **60,** 3079 (2013).
[182] Y. Cordier, M. Hugues, P. Lorenzini, F. Semond, F. Natali, and J. Massies, physica status solidi (c) **2,** 2720 (2005).
[183] L. Sang, M. Liao, and M. Sumiya, Sensors **13,** 10482 (2013).
[184] D. Sharma, A. Motayed, S. Krylyuk, Q. Li, and A. V. Davydov, IEEE Transactions on Electron Devices **60,** 4206 (2013).
[185] R. P. Jindal and A. van der Ziel, Applied Physics Letters **38,** 290 (1981).
[186] M. Fontana, T. Deppe, A. K. Boyd, M. Rinzan, A. Y. Liu, M. Paranjape, and P. Barbara, Scientific Reports **3,** 1634 (2013).
[187] K. F. Mak, K. He, J. Shan, and T. F. Heinz, Nat Nano **7,** 494 (2012).
[188] G. Ghibaudo, O. Roux, C. Nguyen-Duc, F. Balestra, and J. Brini, physica status solidi (a) **124,** 571 (1991).
[189] S. K. Jha, C. Surya, K. J. Chen, K. M. Lau, and E. Jelencovic, Solid-State Electronics **52,** 606 (2008).
[190] S. Yan-Kuin, W. Sun-Chin, W. Ruey-Lue, C. Shoou-Jinn, K. Chih-Hsin, and K. Ta-Ming, IEEE Electron Device Letters **24,** 622 (2003).
[191] D. V. Kuksenkov, G. E. Giudice, H. Temkin, R. Gaska, A. Ping, and I. Adesida, Electronics Letters **34,** 2274 (1998).

BIOGRAPHY

Md Rezaul Hasan completed his undergraduate from Islamic University of technology (a sub-organ of the OIC) in 2009 and joined as Lecturer in the same university at January, 2010. He worked there as lecturer for almost three years. He completed his masters in July, 2012 from IUT. Then, he started his PhD in George Mason University (GMU) at fall, 2012.